

**INTEGRATION OF SPATIO-TEMPORAL VEGETATION DYNAMICS INTO A
DISTRIBUTED ECOHYDROLOGICAL MODEL: APPLICATION TO
OPTIMALITY THEORY AND REAL-TIME WATERSHED SIMULATIONS**

Taehee Hwang

A dissertation submitted to the faculty of the University of North Carolina at Chapel Hill
in partial fulfillment of the requirements for the degree of Doctor of Philosophy in the
Department of Geography

Chapel Hill
2010

Approved by:

Lawrence E. Band, Advisor

Aaron Moody, Reader

Conghe Song, Reader

Gregory W. Characklis, Reader

James S. Clark, Reader

© 2010
Taehee Hwang
ALL RIGHTS RESERVED

ABSTRACT

Taehee Hwang

Integration of spatio-temporal vegetation dynamics into a distributed ecohydrological model:
Application to optimality theory and real-time watershed simulations
(Under the direction of Lawrence E. Band)

Spatio-temporal vegetation dynamics are important drivers to characterize seasonal to annual water and carbon budgets. Spatial adjustment and evolution of the ecosystem is closely related to the geomorphic, climatic, and hydrologic settings. In particular, lateral hydrologic redistribution along flowpaths control the long-term joint adjustments of vegetation and soil over successional and quasi-geological time scales. For this reason, it is complex and challenging to incorporate the many relevant processes and feedbacks between ecological and hydrological systems for the full simulation of water, carbon, and nutrient cycling. Recent developments in remote sensing technology provide the potential to link dynamic canopy measurements with integrated process descriptions within distributed ecohydrological modeling frameworks. In this dissertation, three research studies are presented concerning estimation of spatio-temporal vegetation dynamics in application into a distributed ecohydrological model at the Coweeta Long Term Ecological Research site. In Chapter 2, we test whether the simulated spatial pattern of vegetation corresponds to measured canopy patterns and an optimal state relative to a set of ecosystem processes, defined as maximizing ecosystem productivity and water use efficiency at the catchment scale. A distributed ecohydrological model is simulated at a small catchment scale with various field measurements to see if the evolved pattern of vegetation density along the

flowpaths leads to system-wide emergent optimality for carbon uptake over and above the individual patch. Lateral hydrological connectivity determines the degree of dependency on productivity and resource use with other patches along flowpaths, resulting in different system-wide carbon and water uptake by vegetation. In Chapter 3, phenological signals are extracted from global satellite products to find the topography-mediated controls on vegetation phenology in the study site. It provides a basis to understand spatial variations of local vegetation phenology as a function of microclimate, vegetation community types, and hillslope positions. In Chapter 4, near real-time vegetation dynamics are estimated by fusing multi-temporal satellite images, and integrated into the catchment scale distributed ecohydrological simulation. Integration of spatio-temporal vegetation dynamics into a distributed ecohydrological model helps to simulate ecohydrological feedbacks between vegetation patterns and lateral hydrological redistribution by reducing uncertainty related to state and flux variables.

DEDICATION

This dissertation is dedicated

To my wife and precious daughter, Yuri Kim and Arwen Hwang

To my parents, Jaemook Hwang and Gongja Lee

ACKNOWLEDGEMENTS

First, I would like to thank my advisor, Dr Lawrence Band who deepened and broadened my scope of research views. Considering broad topics of my dissertation, I was so lucky to meet such an open-minded advisor with consistent enthusiasm and a positive manner. He is my role model not only for an academic advisor but also as a lifetime mentor.

I am also grateful to other committee members, Dr. Aaron Moody, Dr. Conghe Song, Dr. Greg Characklis, and Dr. Jim Clark. I learned a lot from their classes over the years. Even though I did not finish all I suggested, they encouraged me and showed interests to my researches from different perspectives. In addition, I would like to thank Dr. Jim Vose, Dr. Paul Bolstad, and Dr. Todd Lookingbill for their support in providing data in Coweeta Hydrologic Lab. I also like to thank my colleagues and friends who worked with me in the fields and helped me for the completion of this dissertation. During pit-digging experiments in the fields, Dr. T.C. Hales broadened my geological views also with impressive untiring energy. Tamara Mittman and Jon Duncan also gave valuable feedbacks to improve my dissertation both academically and grammatically.

Finally, I would like to express my truthful gratitude to my family for their love and supports. My beautiful wife, Yuri Kim was always there not only as a lifetime companion, but also as an academic colleague. My newborn daughter, Arwen Hwang let me know the true happiness of a life. My parents always believed in me from start to finish. I could not have done this without their beliefs.

TABLE OF CONTENTS

LIST OF TABLES	xii
LIST OF FIGURES	xiii
LIST OF ABBREVIATIONS	xix
LIST OF SYMBOLS	xxi
 Chapter 1 Introduction.....	1
1.1 Background	1
1.2 A Process-based Distributed Ecohydrological Model	4
References	8
 Chapter 2 Ecosystem processes at the watershed scale: Extending optimality theory from plot to catchment	12
2.1 Abstract	12
2.2 Introduction	13
2.3 Model overview.....	16
2.3.1 A Farquhar photosynthesis model	16
2.3.2 Coupled photosynthesis – stomatal conductance models	18
2.3.3 Scaling up fluxes from leaves to canopy	19

2.3.4	Nitrogen limitation.....	20
2.3.5	Allocation.....	21
2.4	Materials and methods	24
2.4.1	Site description.....	24
2.4.2	Climate data and historical field measurements	26
2.4.3	Hydrologic gradients of vegetation density	27
2.4.4	Rooting depth and root distributions from soil pits	30
2.4.5	Model parameterization	33
2.4.6	Prescribed rooting depth as a function of hillslope position.....	36
2.4.7	Allocation dynamics with varying rooting depth.....	40
2.5	Results	41
2.5.1	Topographic controls on rooting depth.....	41
2.5.2	Parameter spaces	43
2.5.3	Long-term ecohydrologic optimality at the hillslope scales	45
2.6	Discussion and conclusions.....	49
2.6.1	Optimal vegetation gradients for system-wide productivity.....	49
2.6.2	Compromises between multiple resources.....	50
2.6.3	An objective function of optimality models	53
2.6.4	Allocation dynamics along the hillslope gradients	54
2.6.5	Limitations of this study	56
2.6.6	Conclusions.....	57

Acknowledgements	58
References	59
Chapter 3 Topography-mediated controls on local vegetation phenology estimated from MODIS vegetation index.....	71
3.1 Abstract	71
3.2 Introduction	72
3.3 Materials and methods	74
3.3.1 Study area.....	74
3.3.2 MODIS vegetation index	78
3.3.3 Post-processing analysis	79
3.3.4 A phenology model for multi-year VI datasets.....	83
3.3.5 Analytical solutions for phenological transition dates.....	85
3.3.6 Topographical variables.....	89
3.3.7 Interannual variations between wet and dry years	90
3.3.8 Statistical analysis.....	92
3.4 Results	96
3.4.1 Topographical controls on local vegetation phenology	96
3.4.2 Vegetation phenology between wet vs. dry years.....	98
3.5 Discussion and conclusions.....	103
3.5.1 Temperature controls on vegetation phenology.....	103
3.5.2 Photoperiod controls on vegetation phenology.....	104

3.5.3	Other controls on vegetation phenology	106
3.5.4	Growing season length (GSL) vs. vegetation growth.....	107
3.5.5	Spatial scale issues	109
3.5.6	Conclusions.....	112
	Acknowledgements.....	113
	Appendix.....	114
	References.....	115
 Chapter 4 Estimation of real-time vegetation dynamics for distributed ecohydrological modeling by fusing multi-temporal MODIS and Landsat NDVI data 123		
4.1	Abstract	123
4.2	Introduction	124
4.3	Method and Materials.....	129
4.3.1	Study site.....	129
4.3.2	Landsat NDVI.....	131
4.3.3	MODIS NDVI and FPAR.....	132
4.3.4	Downscaling MODIS FPAR into sub-grid scale.....	134
4.3.5	Simulation of a distributed ecohydrological model	137
4.4	Results	138
4.4.1	MODIS and Landsat NDVI values	138
4.4.2	An example of downscaling.....	145

4.4.3	The effect of the topographically corrected downscaling	149
4.4.4	An example of distributed hydrological modeling	155
4.5	Discussion and conclusions.....	157
4.5.1	General discussion	157
4.5.2	The FPAR-NDVI relationship	158
4.5.3	Scale invariance in sub-grid variability	160
4.5.4	Topographic correction.....	164
4.5.5	Conclusions.....	165
	Acknowledgements.....	166
	References.....	168
Chapter 5	Summary and conclusions.....	175

LIST OF TABLES

Table 1.1: Key processes of RHESSys model	7
Table 2.1: Detailed measurements for soil pits at different topographic positions	31
Table 2.2: Species-specific eco-physiologic model parameters ^a	32
Table 2.3: Other model parameters.....	34
Table 3.1: Summary of phenological and topographic variables	91
Table 3.2: Pearson correlation coefficients between topographic factors and phenological variables ($n = 252$)	95
Table 3.3: Summaries of multiple regression models ($n = 252$).....	97
Table 4.1: Landsat TM and MODIS bandwidths of red and near infrared bands	127

LIST OF FIGURES

Figure 2.1: Water scalar functions of nitrogen transformation rates as a function of soil moisture saturation for sandy loam soils; after Parton <i>et al.</i> (1996).	23
Figure 2.2: A compartment flow diagram of carbon allocation, transfer, and turnover with mixed daily and yearly allocation strategies following the current BIOME-BGC algorithm (Thornton <i>et al.</i> 2002; Thornton 1998).	23
Figure 2.3: Study site (WS18); (a) NDVI (normalized difference vegetation index) from a June 1, 2003 IKONOS image, (b) wetness index, and (c) locations for WS18 (square), LAI (leaf area index) measurements, and soil pits within the Coweeta LTER site. Litter LAI points are from Bolstad <i>et al.</i> (2001). Red and yellow lines represent the boundaries of watersheds, and dashed lines indicate roads along which artificial gaps are shown. (a) and (b) are perspective views from the WS18 outlet. The rectangles within WS18 are three gradient plots (118, 218, and 318). A paired experimental watershed (WS17) is also shown next to the target watershed where white pines (<i>Pinus strobus</i> L.) are planted in 1956 after 15-year clear cut periods.	25
Figure 2.4: (a) A scatter plot between LAI (leaf area index) measurements and NDVI (normalized difference vegetation index), and (b) hydrologic gradients of estimated LAI within the study watershed. Litter LAI measurements are from Bolstad <i>et al.</i> (2001). Circles represent average values, and box plots have lines at the lower quartile, median, and upper quartile values from each binned group. Counts are the number of 10×10 m patches in each group, which are basic units of model simulation.	29
Figure 2.5: Long-term observed and simulated daily streamflow at the study watershed (1990 ~ 2006), including the 3-year calibration period (October 1999 ~ September 2002).	35
Figure 2.6: Time series and scatter plots of observed and simulated soil water content at (a) 118 (xeric), (b) 218 (mesic), and (c) 318 (intermediate) gradient plots within the target watershed (Figure 2.3b).	37

Figure 2.7: Simulated long term (1941 ~ 2005) nitrogen transformation rates (plant uptake, mineralization, nitrification, and denitrification) in litter and soil as a function of wetness index. Note that these modeled gradients largely result from in situ N cycling as lateral transport of mobile nitrogen (nitrate), or organic litter downslope is not included in the simulation version. Each point represents a 10×10 m cell ($n = 1253$), a basic unit of model simulation. 38

Figure 2.8: The distribution of roots as a function of soil depth for pits located on (a) ridges and (b) hollows. Distributions are expressed as root cumulative frequency and as absolute number. Grey lines represent individual pits, while black lines are the mean of all pits. Photographs are vertical sections of two *Q. rubra* pits (Table 2.1) dug within 20 m of each other. Note the difference in the depth of the dark A horizon between the two sites. Blue painted roots were used for analysis of root distributions. Modified from Figure 3 in Hales *et al.* (2009). 42

Figure 2.9: Mean absolute error (MAE) of simulated LAI within WS18 over multiple realizations of average rooting depth (RD_{avg}) and spatial pattern of rooting depth (RD_{dev}) under (a) the constant and (b) the alternative allocation strategies. 44

Figure 2.10: 3-D and 2-D contour plots of long-term simulated (1941 ~ 2005) average annual (a) NPP (net primary productivity), (b) ET (evapotranspiration), and (c) WUE (water used efficiency) over sampled RD_{avg} and RD_{dev} under constant allocation strategy. The color bar represents the mean absolute error (MAE) of simulated LAI (Figure 2.9a). 46

Figure 2.11: 3-D and 2-D contour plots of long-term simulated (1941 ~ 2005) average annual (a) NPP (net primary productivity), (b) ET (evapotranspiration), and (c) WUE (water used efficiency) over sampled RD_{avg} and RD_{dev} under alternative allocation strategy, where allocation ratios are as a function of local rooting depth. The color bar represents the mean absolute error (MAE) of simulated LAI (Figure 2.9b). 47

Figure 2.12: 3-D plots for long-term annual NPP (net primary productivity) and ANPP (aboveground NPP) under (a) constant and (b) alternative allocation strategies with varying RD_{avg} and RD_{dev} parameters. Contours at the x-y plane represent ANPP values. Note that allocation ratios of ANPP to NPP are constant under constant allocation

strategy, while they decrease in proportion to rooting depth under alternative allocation strategy. Long term patterns of vegetation density (LAI) follow ANPP as a constant portion of cumulative ANPP is allocated into foliar biomass.	48
Figure 3.1: A study site (Coweeta Hydrologic Lab). Grids represent the MODIS (MOD13Q1; about 230 m) pixels. Red lines represent the boundaries of watersheds. Letters indicates the pixels for examples of filtering and fitting methods (Figure 3.3; Figure 3.4).	76
Figure 3.2: A typic diagram from Day <i>et al.</i> (1988), which describes vegetation community types within the study site as a function of slope, aspect, elevation, and hillslope positions.	77
Figure 3.3: Examples of two-step filtering methods from 8-year historical trajectories (left column) and time-series (right column) of estimated LAI at selected MODIS pixels ((a) ~ (i); Figure 3.1). Grey and black dots represent filtered values by the outlier exclusion analysis and the modified BISE methods, respectively.	81
Figure 3.4: Examples of the difference logistic function fitting for 8-year estimated LAI datasets at selected MODIS pixels ((a) ~ (i); Figure 3.1). Vertical dotted lines are phenological transition dates (t^*) from Eq. 3.5.	86
Figure 3.5: Analytical solutions of phenological variables; (a) the difference logistic function, (b) the first derivative, (c) the second derivative (a thick line) and curvature (grey lines; Eq. 3.4), and (d) the third derivative (a thick line) and the rate of curvature change (CCR; grey lines). The curvature and CCR curves are drawn with different c parameter values (0.5 ~ 4.0; Eq. 3.2). The vertical grey lines are analytical solutions for phenological variables from Eq. 3.5, not changed with different c parameter values.	87
Figure 3.6: Paired scatter plots between topographic and phenological variables. Fitted lines show strongly significant relationships from multiple regression models (Table 3.3).	94

Figure 3.7: Elevational controls on (a) Mid_{on} (grey) and Mid_{off} (black), (b) $Length_{on}$ (grey) and $Length_{off}$ (black), and (c) LAI_{max} (grey) and LAI_{min} (black). Horizontal error bars represent $Length_{on}$ and $Length_{off}$	100
Figure 3.8: Scatter plots of six phenological variables (Mid_{on} , Mid_{off} , $Length_{off}$, $Length_{on}$, LAI_{min} , and LAI_{max}) between extremely wet (2003, 2005) and dry (2001, 2008) years.	101
Figure 3.9: Major topographic controls ($elev$, $taspect$) on length phenological variables ($Length_{on}$, $Length_{off}$) between wet (light circles and dashed lines) and dry years (dark circles and solid line).	102
Figure 3.10: Comparison of radiation proxies ($taspect$, PRR_g) from two different upscaling methods at each MODIS pixels. Radiation proxies of x-axis were calculated from upscaled DEM at MODIS scale (about 250 m), while those of y-axis from averaging of the original scale radiation proxies from LIDAR DEM (about 6 m)....	111
Figure 4.1: A study site (Coweeta Hydrologic Lab). Grids represent the MODIS (MOD13Q1; about 230 m) pixels. Red and yellow lines represent the boundaries of sub-watersheds and WS08 (an upper basin of Coweeta). Letters indicates the pixels for examples of fitting and downscaling methods (Figure 4.2; Figure 4.3; Figure 4.8; Figure 4.9)	130
Figure 4.2: Examples of fitting by the difference logistic function for 8-year MODIS NDVI datasets (2001 ~ 2008) at selected MODIS pixels ((a) ~ (i); Figure 4.1).	140
Figure 4.3: Interannual phenological variations of the fitted MODIS NDVI model at selected MODIS pixels ((a) ~ (i); Figure 4.1).....	142
Figure 4.4: Boxplots for spatial variations of mid-day of (a) greenup and (b) senescence periods, and (c) fitted maximum and minimum NDVI values within the study site ($n = 369$) for each year, calculated from the fitted MODIS NDVI model (Figure 4.3). Boxes have lines at the lower, median, and upper quartile values. Lines are extended to the most extreme values within the Whiskers, defined as 1.5 times the inter-quartile range from the lower and upper quartiles. Outliers are displayed with black dots....	143

Figure 4.5: Spatio-temporal patterns of Landsat NDVI values within the Coweeta basin as a function of DOY. All Landsat TM images are from 2000 to 2008, and absolutely cloud-free. Points and vertical lines represent an average, and 5th and 95th percentiles of spatial NDVI values within the WS08 watershed ($n = 8654$; Figure 4.1). 144

Figure 4.6: An example of two downscaling methods on May 5, 2008; (a) a fitted MODIS FPAR image, (b) a composite Landsat NDVI image, (c) a proportionality parameter (α_t) map by the simple downscaling method, (d) a downscaled FPAR map by the simple downscaling method, (e) a potential hourly radiation map ($\text{kJ m}^{-2} \text{h}^{-1}$), and (f) a downscaled FPAR map by the topographically corrected downscaling method..... 147

Figure 4.7: Two examples of the topographically corrected downscaling method on July 1, 2008 (left column) and February 8, 2008 (right column); (a) and (b) fitted MODIS FPAR images, (c) and (d) composite Landsat TM NDVI images, and (e) and (f) downscaled FPAR maps. 148

Figure 4.8: Examples of the topographically corrected downscaling for the MODIS FPAR at selected MODIS pixels in 2008 ((a) ~ (i); Figure 4.1). Grey dotted and color solid lines represent the fitted MODIS FPAR and the downscaled sub-grid FPAR values respectively. 151

Figure 4.9: Examples of the topographically corrected downscaling at selected MODIS pixels in 2008 ((a) ~ (i); Figure 4.1). Color solid lines represent the downscaled sub-grid LAI values estimated from downscaled sub-grid FPAR values (Figure 4.8)..... 152

Figure 4.10: A scatter plot between $\alpha_{topo_corrected}$ (a proportionality parameter in the topographically corrected downscaling) and α_{simple} (a proportionality parameter in the simple downscaling) values on May 5 (cross), February 8 (triangle), and July 1 (circle), 2008..... 153

Figure 4.11: Temporal patterns of $\alpha_{topo_corrected}$ (upper) and α_{simple} (lower) values for a simulation period (2001 ~ 2008) with 5-day intervals. Points and vertical lines represent average, and 5th and 95th percentiles of spatial distributions in the study site ($n = 369$) on the same DOY each year. Note that α parameters are calculated each day, not each DOY..... 154

Figure 4.12: Observed and simulated daily streamflow at the study watershed (WS08; Figure 4.1), including the 3-year calibration period (October 2003 ~ September 2006).	156
--	-----

Figure 4.13: Temporal patterns of relative differences (left column) and scatter plots (right column) between (a) $NDVI_{avg}$ and $NDVI_{lump}$, (b) $NDVI_{avg}$ and $NDVI_{wgt}$, and (c) $NDVI_{lump}$ and $NDVI_{wgt}$. $NDVI_{lump}$ is the NDVI calculated from aggregated radiance at the MODIS scale. $NDVI_{avg}$ is the averaged NDVI at MODIS scale from sub-grid Landsat NDVI values. $NDVI_{wgt}$ is the weighted averaged NDVI with respect to sub-grid incoming radiance (Eq. 4.8). Horizontal and vertical lines represent 5th and 95th percentiles of the spatial NDVI values within the WS08 watershed ($n = 8654$; Figure 4.1).	162
--	-----

LIST OF ABBREVIATIONS

ANPP	Aboveground Net Primary Productivity
AVHRR	Advanced Very High Resolution Radiometer
BISE	Best Index Slope Extraction
BRDF	Bidirectional Reflectance Distribution Function
CCR	Curvature Change Rate
DBH	Diameter at Breast Height
DEM	Digital Elevation Model
DOS	Dark Object Subtraction
DOY	Day Of Year
ET	Evapotranspiration
EVI	Enhanced Vegetation Index
FPAR	Fraction of absorbed Photosynthetically Active Radiation
GPS	Geographic Positioning System
GSL	Growing Season Length
L1T	Level-one Terrain-corrected
LAI	Leaf Area Index
TM	Thematic Mapper
LIDAR	LIght Detection And Ranging
LTER	Long Term Ecological Research
MAE	Mean Absolute Error
MODIS	MODerate resolution Imaging Spectro-radiometer

MRT	MODIS Reprojection Tool
NDVI	Normalized Difference Vegetation Index
NPP	Net Primary Productivity
PAR	Photosynthetically Active Radiation
QC	Quality Control
RHESSys	Regional Hydro-Ecological Simulation System
RuBP	Ribulose-BisPhosphate carboxylase-oxygenase
SLA	Specific Leaf Area
SR	Simple Ratio
STARFM	Spatial and Temporal Adaptive Reflectance Fusion Model
UTM	Universal Transverse Mercator
VI	Vegetation Index
WUE	Water Use Efficiency

LIST OF SYMBOLS

A	net rate of leaf photosynthesis
a, b	fitting variables in the logistic function
A_j	RuBP-limited photosynthesis (an electron transport rate)
$APAR$	absorbed photosynthetically active radiation per unit leaf area
$APAR_{i,t}$	absorbed PAR at each sub-grid pixel i and date t
A_v	Rubisco-limited photosynthesis (a carboxylation rate)
c	difference between fitted maximum and minimum NDVI or LAI
C_i	partial pressure of within leaf CO_2
CO_2	atmospheric concentration of carbon dioxide
d	a fitted minimum or background NDVI or LAI value
$elev$	elevation
$FPAR$	MODIS FPAR
$FPAR_{i,t}$	FPAR values of sub-grid i on date t
$FPAR_t$	MODIS FPAR on date t
g_c	stomatal conductivity for CO_2
g_s	stomatal conductance for water
$g_{s,max}$	maximum stomatal conductance for water
$g_{s,shade}$	stomatal conductance for water per unit shaded leaf area
$g_{s,sunlit}$	stomatal conductance for water per unit sunlit leaf area
i	sub-grid pixel locations
I_e	effective irradiance
$IPAR_i$	potential incident PAR at each sub-grid pixel i
$IPAR_{i,DOY}$	potential incident PAR at each sub-grid pixel i on corresponding DOY

J	electron transport rate
J_{max}	maximum electron transport rate
K_c	Michaelis-Menten constant of Rubisco for CO ₂
K_o	Michaelis-Menten constant of Rubisco for O ₂
LAI_{max}	fitted maximum leaf area index
LAI_{min}	fitted minimum leaf area index
LAI_{shade}	total shaded leaf area index
LAI_{sunlit}	total sunlit leaf area index
$Length_{off}$	length of the senescence period
$Length_{on}$	length of the greenup period
Mid_{off}	mid-day of the senescence period
Mid_{on}	mid-day of the greenup period
n	number of sub-grid pixels within a single MODIS pixel
$NDVI_{avg}$	mean NDVI of $NDVI_i$ values within a single MODIS pixel
$NDVI_i$	composite Landsat NDVI at each sub-grid pixel i
$NDVI_{i,DOY}$	composite Landsat NDVI at each sub-grid pixel i on corresponding DOY
$NDVI_{lump}$	lumped NDVI calculated from aggregated radiance at the MODIS scale
$NDVI_{wgt}$	weighted mean of $NDVI_i$ with respect to $IPAR_i$
O_i	partial pressure of within leaf O ₂
PRR	potential relative radiation for the whole year
PRR_f	potential relative radiation for the senescence season (Oct, Nov)
PRR_g	potential relative radiation for the greenup season (Apr, May)
RD	a local rooting depth
R_d	daily leaf respiration
RD_{avg}	average rooting depth within the hillslope
RD_{dev}	spatial pattern of rooting depth

t	date
t'	transition dates for phenological signals
$taspect$	transformed aspect
$topidx$	wetness index (or topographic index)
V_{max}	maximum rate of carboxylation
VPD	vapor pressure deficit
WI	local wetness index
WI_{avg}	average wetness index within the hillslope
α	a proportionality parameter
α_{simple}	α of the simple downscaling method
α_t	α on date t
$\alpha_{t,simple}$	α of the simple downscaling method on date t
$\alpha_{t,topo-corrected}$	α of the topographically corrected downscaling method on date t
$\alpha_{topo-corrected}$	α of the topographically corrected downscaling method
Γ^*	CO ₂ -compensation point
θ	sun zenith angle
κ	signed curvature
ψ	soil water potential
Ω	foliage clumping index

Chapter 1 Introduction

1.1 Background

Ecohydrology may be defined as the science which seeks to describe the hydrologic mechanisms that underlie ecologic patterns and processes (Rodriguez-Iturbe 2000). We expand on this definition by including the complementary question of how ecological mechanisms underlie hydrologic patterns and processes, essentially examining the coupled evolution and interactions within ecohydrological systems.

Ecohydrological processes incorporate a very wide variation in temporal scales ranging from sub-daily energy, water, carbon and nutrient flux, to decadal and century level growth and aggradation of ecosystems and biogeochemical development of soils. These processes are interconnected over both time and space by three-dimensional circulation of water through the landscape by the set of dominant surface and subsurface flowpaths, interacting with long term modification of canopy and soil conditions. Forested watershed responses to climatic patterns involve complex interactions between ecological and hydrological processes (e.g. interception, infiltration, evapotranspiration, photosynthesis, drainage, succession etc.) mediated by soil moisture dynamics, operating at different temporal and spatial scales. Therefore, spatio-temporal dynamics of soil moisture are key links between hydrologic and biogeochemical processes (Rodriguez-Iturbe 2000).

This level of complexity suggests that prescription of major sets of state or flux variables (e.g. leaf area index, soil saturation, streamflow, and evapotranspiration) can lead to the accumulation of

significant bias in model behavior. Especially in topographically complex terrains, prescribing averaged spatial and temporal variations of state variables may underestimate the effect of severe drought due to asymmetric nature of the spatial distribution of soil moisture along with its non-linear control on water and carbon processes (e.g. Band *et al.* 1993). Given the complexity of these interactions and their spatio-temporal variations, we must incorporate new observations of ecological and hydrological form and process to reduce the uncertainty related to the state and flux variables in the model. In this process, temporal and spatial resolutions of data assimilation strongly depend on available ecohydrological datasets.

Recent developments in ground based and remote sensing observational technologies, along with coupled distributed ecohydrological modeling paradigms provide the potential to mitigate this problem by linking dynamics measurements with integrated process descriptions. High resolution spatial information (e.g. land cover, topography, canopy cover, soil moisture, precipitation etc.) have aided the development of complex fully distributed models that construct a detailed spatial representation of the variability of the hydrological processes within the watershed. In particular, near real-time global satellite products (MODIS; MODerate Resolution Imaging Spectro-radiometer) enable us to integrate spatio-temporal dynamics of key ecohydrological processes, such as spatio-temporal vegetation dynamics, which are difficult to adequately incorporate in classical lumped hydrological models.

Vegetation density is usually represented by the fraction of absorbed photosynthetically active radiation (FPAR) and leaf area index (LAI). FPAR is a robust indicator for energy absorption by vegetation and subsequent carbon uptake (e.g. light use efficiency). LAI is an important driver in process-based biogeochemical models, which tends to be correlated with aboveground net primary production and biomass across a broad range of ecosystems. LAI represents canopy interception capacity for evaporation and potential transpiration through stomata in the water cycle. Vegetation compromises between its growth and water stress for optimal carbon uptake (so-called ‘growth-stress trade-off’) represented as a non-linear relationship between FPAR (energy use) and LAI (water use).

These two important biophysical properties are linearly or non-linearly correlated with NDVI (normalized difference vegetation index) from remote sensing images, so the NDVI plays a crucial role in estimating spatio-temporal dynamics of vegetation density from remote sensing images at different scales. In this study, phenological state variables (e.g. FPAR, LAI) are locally estimated within the study area using NDVI values from multi-temporal remotely sensed data (e.g. IKONOS, Landsat TM, MODIS), further evaluated with field measurements.

This dissertation aims to integrate spatio-temporal vegetation dynamics into a distributed ecohydrological model at different scales, operating over sub-daily to decadal level time scales with specific applications to ecological optimality theory and real-time watershed simulations. Three related questions and topics are addressed within the dissertation papers:

1. To determine if the observed vegetation patterns along hydrologic gradients within a small catchment represent long-term ecohydrologic pattern optimization for carbon uptake (e.g., full system productivity or water use efficiency maximization) at the hillslope scale.
2. To find topography-mediated controls on local vegetation phenology from MODIS NDVI data, and to relate these spatial phenological patterns to micro-climate variations and other factors (e.g. vegetation community types, topographic positions).
3. To develop a downscaling method fusing multi-temporal MODIS-Landsat data in conjunction with topographic information to produce near real-time estimates of high spatial and temporal resolution canopy phenology in complex terrain, for assimilation into the distributed ecohydrological model.

For the first question, Chapter 2 specifically uses the modeling framework to assess long term development and co-evolution of the ecosystem canopy, soil, and topography. The spatial gradient of vegetation density within a small catchment is estimated with fine-resolution satellite imagery (IKONOS) and various field measurements, evaluated with simulated vegetation growth patterns from

different root depth and allocation strategies as a function of hillslope position. Then, we test whether the simulated spatial pattern of vegetation corresponds to measured canopy patterns and an optimal state relative to a set of ecosystem processes, defined as maximizing ecosystem productivity and water use efficiency at the catchment scale.

In Chapter 3, we develop a robust filtering and fitting method to extract phenological signals from the multi-year trajectories of MODIS NDVI data, and relate spatial patterns of vegetation phenology to topographic factors by a statistical analysis to answer the second question. These topography-mediated phenological patterns are interpreted based on spatial variations of micro-climate and other factors (e.g. vegetation community types, hillslope positions). In particular, scale issues would be examined by comparing these phenological patterns with historical field measurements and interannual variations between very wet and dry years.

For the last question, we develop methods to estimate near real-time vegetation dynamics by downscaling the fitted MODIS FPAR into the Landsat scale with two suggested downscaling methods for the 8-year period (2001 ~ 2008) in Chapter 4. The sub-grid variability of vegetation density within the MODIS pixels is inferred each day from composite NDVI images as a function of day of year assuming they are interannually consistent. Examples of a distributed ecohydrological model are shown assimilating the real-time downscaled vegetation dynamics.

Finally, Chapter 5 summarizes important findings and discusses their further implications.

1.2 A Process-based Distributed Ecohydrological Model

RHESSys (Regional Hydro-Ecological Simulation System) is a GIS-based, ecohydrological modeling framework designed to simulate carbon, water and nutrient cycling in complex terrain (Band *et al.* 1993; Tague and Band 2004). One of the unique features of RHESSys is its hierarchical landscape representation. RHESSys combines both a set of physically based process models and a methodology for partitioning and parameterizing the landscape. The spatially distributed structure

enables the modeling of spatio-temporal interactions between the different ecohydrological processes at the plot to the watershed scale. This approach allows different processes to be affiliated at different spatio-temporal scales and the basic modeling unit to be of arbitrary shape, rather than strictly grid-based.

RHESSys has been developed from several pre-existing models. First, a microclimate model, MT-CLIM (Running *et al.* 1987) uses topography and user supplied base station information to extrapolate spatially variable climate variables over topographically varying terrain. At the patch level, an eco-physiological model is adapted from BIOME-BGC (Running and Coughlan 1988; Running and Hunt 1993; Kimball *et al.* 1997) to estimate carbon, water and potential nitrogen fluxes from different canopy cover types, while representation of soil organic matter and nutrient cycling in RHESSys is largely based on CENTURY model (Parton *et al.* 1993). RHESSys also uses the CENTURY_{NGAS} (Parton *et al.* 1996) approach to model nitrogen cycling processes such as nitrification and denitrification (Band *et al.* 2001). At a hillslope scale, a quasi-distributed hydrological model, TOPMODEL (Beven and Kirkby 1979) is integrated which distributes soil moisture based on the distribution of a topographically defined wetness index.

A modified version 5.8 of RHESSys is used in this study. Recent BIOME-BGC (version 4.1.1) changes from the comparison with flux tower data were updated to this version of RHESSys for this study. These are relevant to the deployment strategy of retranslocated nitrogen and the treatment of daily allocation in the face of a carbon pool deficit (Thornton 2000). A conditional three-layer model in the soil column (Famiglietti and Wood 1994) is integrated for vertical water processes; the root zone layer, the transmission layer, and the saturated layer. The unsaturated soil layer is partitioned into two layers (root zone and transmission layers) only when water table depth is below prescribed root zone depth. Roots are assumed to extend uniformly throughout the root zone. The upward capillary flux from the water table passes through the transmission layer and directly into the root zone layer.

RHESSys has been successfully applied for ecohydrological simulations in forested watersheds across diverse climate regions; watershed scale transpiration and production (Band *et al.* 1991, 1993; Band 1993; Nemani *et al.* 1993; Mackay *et al.* 2003; Zierl *et al.* 2007; Hwang *et al.* 2008, 2009), nitrogen processes (Band *et al.* 2001; Creed *et al.* 1996; Creed and Band 1998a; Groffman *et al.* 2009; Tague 2009), spatial patterns of vegetation growth (Mackay and Band 1997; Mackay 2001), spatial patterns of vegetation species (Meentemeyer *et al.* 2001; Meentemeyer and Moody 2002), hydrologic responses to climate change (Band *et al.* 1996; Baron *et al.* 2000; Christensen *et al.* 2008; Tague *et al.* 2008, 2009; Jefferson *et al.* 2008), snow distribution (Christensen *et al.* 2008; Tague *et al.* 2008; Hartman *et al.* 1999), the characterization of scale-dependent flow variability (Sanford *et al.* 2007), and streamflow prediction of ungauged watersheds (Tague and Pohl-Costello 2008). Key processes in RHESSys are shown in Table 1.1. Detailed explanations of this model are available in the RHESSys homepage (<http://fiesta.bren.ucsb.edu/~rhessys/>), and Tague and Band (2004).

Table 1.1: Key processes of RHESSys model

Processes or Parameters		References
Vegetation		
Water	Interception	$f(all-sided\ LAI)$
	Transpiration	Penman-Monteith Eq. ^a
	Leaf Conductance	$f(T, \theta, APAR, VPD, CO_2)^a$ (Jarvis 1976)
Carbon	Photosynthesis	Farquhar Eq. ^a (Farquhar <i>et al.</i> 1980)
	Maintenance Respiration	$f(T, N,C)^{\dagger}$ (Ryan 1991)
	Growth Respiration	Constant (Biome-BGC)
	Allocation / Mortality	Constant (Biome-BGC)
	Turnover	Constant (Biome-BGC)
Nitrogen	Stoichiometrically constant C/N ratios for all compartments	
	Retranslocation of stored nitrogen during the litterfall process	
Soil		
Water	Infiltration	Phillip's Eq.
	Drainage	(Clapp and Hornberger 1978)
	Exfiltration / Capillary Rise	(Eagleson 1978c)
	Lateral Redistribution	TOPMODEL (Beven and Kirkby 1979)
	Saturated Throughflow	TOPMODEL (Beven and Kirkby 1979)
Carbon	Decomposition	$f(T, \theta, C, M, N)$ (Parton <i>et al.</i> 1996)
Nitrogen	Mineralization	$f(T, \theta, M, NH_4^+)$ (Parton <i>et al.</i> 1996)
	Denitrification	$f(\theta, M, NO_3^-)$ (Parton <i>et al.</i> 1996)
	Leaching	Flushing hypothesis
	Plant Uptake	$f(soil\ mineral\ N)$

^acomputed for sunlit and shaded leaves separately; *LAI* = leaf area index, *T* = temperature, θ = rootzone soil moisture contents, *APAR* = absorbed photosynthetically active radiation, *VPD* = vapor pressure deficit, *N* = nitrogen contents, *C* = substrate (carbon) quality, *M* = substrate (carbon) storage

References

- Band LE (1993) Effect of Land-Surface Representation on Forest Water and Carbon Budgets. *Journal of Hydrology*, **150**, 749-772.
- Band LE, Mackay DS, Creed IF, Semkin R, Jeffries D (1996) Ecosystem processes at the watershed scale: Sensitivity to potential climate change. *Limnology and Oceanography*, **41**, 928-938.
- Band LE, Patterson P, Nemani R, Running SW (1993) Forest ecosystem processes at the watershed scale: incorporating hillslope hydrology. *Agricultural and Forest Meteorology*, **63**, 93-126.
- Band LE, Peterson DL, Running SW, Coughlan J, Lammers R, Dungan J, Nemani R (1991) Forest Ecosystem Processes at the Watershed Scale - Basis for Distributed Simulation. *Ecological Modelling*, **56**, 171-196.
- Band LE, Tague CL, Groffman P, Belt K (2001) Forest ecosystem processes at the watershed scale: hydrological and ecological controls of nitrogen export. *Hydrological Processes*, **15**, 2013-2028.
- Baron JS, Hartman MD, Band LE, Lammers RB (2000) Sensitivity of a high-elevation Rocky Mountain watershed to altered climate and CO₂. *Water Resources Research*, **36**, 89-99.
- Beven K, Kirkby M (1979) A physically-based variable contributing area model of basin hydrology. *Hydrologic Science Bulletin*, **24**, 43-69.
- Christensen L, Tague CL, Baron JS (2008) Spatial patterns of simulated transpiration response to climate variability in a snow dominated mountain ecosystem. *Hydrological Processes*, **22**, 3576-3588.
- Clapp RB, Hornberger GM (1978) Empirical equations for some soil hydraulic-properties. *Water Resources Research*, **14**, 601-604.
- Creed IF, Band LE (1998) Exploring functional similarity in the export of nitrate-N from forested catchments: A mechanistic modeling approach. *Water Resources Research*, **34**, 3079-3093.
- Creed IF, Band LE, Foster NW, Morrison IK, Nicolson JA, Semkin RS, Jeffries DS (1996) Regulation of nitrate-N release from temperate forests: A test of the N flushing hypothesis. *Water Resources Research*, **32**, 3337-3354.
- Eagleson PS (1978) Climate, Soil, and Vegetation .3. Simplified Model of Soil-Moisture Movement in Liquid-Phase. *Water Resources Research*, **14**, 722-730.
- Famiglietti JS, Wood EF (1994) Multiscale Modeling of Spatially-Variable Water and Energy-Balance Processes. *Water Resources Research*, **30**, 3061-3078.

- Farquhar GD, Caemmerer SV, Berry JA (1980) A Biochemical-Model of Photosynthetic CO₂ Assimilation in Leaves of C₃ Species. *Planta*, **149**, 78-90.
- Groffman PM, Butterbach-Bahl K, Fulweiler RW, et al (2009) Challenges to incorporating spatially and temporally explicit phenomena (hotspots and hot moments) in denitrification models. *Biogeochemistry*, **93**, 49-77.
- Hartman MD, Baron JS, Lammers RB, Cline DW, Band LE, Liston GE, Tague C (1999) Simulations of snow distribution and hydrology in a mountain basin. *Water Resources Research*, **35**, 1587-1603.
- Hwang T, Band LE, Hales TC (2009) Ecosystem processes at the watershed scale: Extending optimality theory from plot to catchment. *Water Resources Research*, **45**, W11425.
- Hwang T, Kang S, Kim J, Kim Y, Lee D, Band L (2008) Evaluating drought effect on MODIS Gross Primary Production (GPP) with an eco-hydrological model in the mountainous forest, East Asia. *Global Change Biology*, **14**, 1037-1056.
- Jarvis PG (1976) The Interpretation of the Variations in Leaf Water Potential and Stomatal Conductance Found in Canopies in the Field. *Philosophical Transactions of the Royal Society of London. Series B, Biological Sciences*, **273**, 593-610.
- Jefferson A, Nolin A, Lewis S, Tague C (2008) Hydrogeologic controls on streamflow sensitivity to climate variation. *Hydrological Processes*, **22**, 4371-4385.
- Kimball JS, Thornton PE, White MA, Running SW (1997) Simulating forest productivity and surface-atmosphere carbon exchange in the BOREAS study region. *Tree physiology*, **17**, 589-599.
- Mackay DS (2001) Evaluation of hydrologic equilibrium in a mountainous watershed: incorporating forest canopy spatial adjustment to soil biogeochemical processes. *Advances in Water Resources*, **24**, 1211-1227.
- Mackay DS, Band LE (1997) Forest ecosystem processes at the watershed scale: dynamic coupling of distributed hydrology and canopy growth. *Hydrological Processes*, **11**, 1197-1217.
- Mackay DS, Samanta S, Nemani RR, Band LE (2003) Multi-objective parameter estimation for simulating canopy transpiration in forested watersheds. *Journal of Hydrology*, **277**, 230-247.
- Meentemeyer RK, Moody A (2002) Distribution of plant life history types in California chaparral: the role of topographically-determined drought severity. *Journal of Vegetation Science*, **13**, 67-78.
- Meentemeyer RK, Moody A, Franklin J (2001) Landscape-scale patterns of shrub-species abundance in California chaparral - The role of topographically mediated resource gradients. *Plant Ecology*, **156**, 19-41.
- Nemani R, Pierce L, Running S, Band L (1993) Forest Ecosystem Processes at the Watershed Scale: Sensitivity to Remotely-Sensed Leaf Area Index Estimates. *International Journal of Remote Sensing*, **14**, 2519-2534.

- Parton WJ, Mosier AR, Ojima DS, Valentine DW, Schimel DS, Weier K, Kulmala AE (1996) Generalized model for N₂ and N₂O production from nitrification and denitrification. *Global Biogeochemical Cycles*, **10**, 401-412.
- Parton WJ, Scurlock JMO, Ojima DS, et al (1993) Observations and modeling of biomass and soil organic-matter dynamics for the grassland biome worldwide. *Global Biogeochemical Cycles*, **7**, 785-809.
- Rodriguez-Iturbe I (2000) Ecohydrology: A hydrologic perspective of climate-soil-vegetation dynamics. *Water Resources Research*, **36**, 3-9.
- Running SW, Hunt ER (1993) Generalization of a Forest Ecosystem Process Model for Other Biomes, BIOME-BCG, and an Application for Global-Scale Models. In: *Scaling Physiological Processes: Leaf to Globe* (eds Ehleringer JR, Field CB), pp. 141-158. Academic Press Inc., San Diego, CA, USA.
- Running SW, Coughlan JC (1988) A general-model of forest ecosystem processes for regional applications .1. hydrologic balance, canopy gas-exchange and primary production processes. *Ecological Modelling*, **42**, 125-154.
- Running SW, Nemani RR, Hungerford RD (1987) Extrapolation of synoptic meteorological data in mountainous terrain and its use for simulating forest evapotranspiration and photosynthesis. *Canadian Journal of Forest Research-Revue Canadienne De Recherche Forestiere*, **17**, 472-483.
- Ryan MG (1991) Effects of climate change on plant respiration. *Ecological Applications*, **1**, 157-167.
- Sanford SE, Creed IF, Tague CL, Beall FD, Buttle JM (2007) Scale-dependence of natural variability of flow regimes in a forested landscape. *Water Resources Research*, **43**, W08414.
- Tague C (2009) Modeling hydrologic controls on denitrification: sensitivity to parameter uncertainty and landscape representation. *Biogeochemistry*, **93**, 79-90.
- Tague C, Grant G, Farrell M, Choate J, Jefferson A (2008) Deep groundwater mediates streamflow response to climate warming in the Oregon Cascades. *Climatic Change*, **86**, 189-210.
- Tague C, Pohl-Costello M (2008) The Potential Utility of Physically Based Hydrologic Modeling in Ungauged Urban Streams. *Annals of the Association of American Geographers*, **98**, 818-833.
- Tague C, Seaby L, Hope A (2009) Modeling the eco-hydrologic response of a Mediterranean type ecosystem to the combined impacts of projected climate change and altered fire frequencies. *Climatic Change*, **93**, 137-155.
- Tague CL, Band LE (2004) RHESSys: Regional Hydro-Ecologic Simulation System--an object-oriented approach to spatially distributed modeling of carbon, water, and nutrient cycling. *Earth Interactions*, **8**, 1-42.

Thornton PE (2000) *User's Guide for Biome-BGC, Version 4.1.1*. Numerical Terradynamic Simulation Group, University of Montana, Missoula, MT, USA.

Zierl B, Bugmann H, Tague CL (2007) Water and carbon fluxes of European ecosystems: An evaluation of the ecohydrological model RHESSys. *Hydrological Processes*, **21**, 3328-3339.

Chapter 2 Ecosystem processes at the watershed scale: Extending optimality theory from plot to catchment

2.1 Abstract

The adjustment of local vegetation conditions to limiting soil water by either maximizing productivity or minimizing water stress has been an area of central interest in ecohydrology since Eagleson's classic study (Eagleson 1978a, 1978b, 1978c, 1978d, 1978e, 1978f, 1978g, 1982; Eagleson and Tellers 1982). This work has typically been limited to consider one-dimensional exchange and cycling within patches and has not incorporated the effects of lateral redistribution of soil moisture, coupled ecosystem carbon and nitrogen cycling, and vegetation allocation processes along topographic gradients. We extend this theory to the hillslope and catchment scale, with in situ and downslope feedbacks between water, carbon and nutrient cycling within a fully transient, distributed model. We explore whether ecosystem patches linked along hydrologic flowpaths as a catena evolve to form an emergent pattern optimized to local climate and topographic conditions. Lateral hydrologic connectivity of a small catchment is calibrated with streamflow data and further tested with measured soil moisture patterns. Then, the spatial gradient of vegetation density within a small catchment estimated with fine-resolution satellite imagery and field measurements is evaluated with simulated vegetation growth patterns from different root depth and allocation strategies as a function of hillslope position. This is also supported by the correspondence of modeled and field measured spatial patterns of root depths and catchment-level aboveground vegetation productivity. We test whether the simulated spatial pattern of vegetation corresponds to measured canopy patterns and an optimal state

relative to a set of ecosystem processes, defined as maximizing ecosystem productivity and water use efficiency at the catchment scale. Optimal carbon uptake ranges show effective compromises between multiple resources (water, light, and nutrients), modulated by vegetation allocation dynamics along hillslope gradient.

2.2 Introduction

Eagleson proposed an elegant optimality hypothesis in water-limited ecosystems (Eagleson 1978a, 1978b, 1978c, 1978d, 1978e, 1978f, 1978g, 1982; Eagleson and Tellers 1982), based on the Darwinian approach that ‘current vegetation composition is an optimal state for productivity’ (Eagleson 2002). In the absence of significant disturbance, natural soil-vegetation systems would co-evolve ‘gradually and synergistically’ with changes in soil structure driven by vegetation to achieve an equilibrium state. Eagleson posited that these equilibria are based on three different optimization strategies at different temporal scales. At short time scales with given climate and soil conditions, minimization of soil water stress produces a vegetation canopy in which steady-state soil moisture will be maximized to minimize vegetation water stress. This short-term equilibrium hypothesis is usually interpreted as a ‘growth-stress trade-off’ (Mackay 2001; Kerkhoff *et al.* 2004), which conceptually describes the optimal carbon uptake or biomass productivity represented by canopy density in terms of water use. Maximization of biomass productivity is then assumed to control the long-term joint adjustment of vegetation species and soil over successional and quasi-geological time scales respectively. This hypothesis suggests that optimal canopy density in water-limited ecosystems is to be found between minimum water stress and maximum productivity (Rodriguez-Iturbe *et al.* 1999a).

Over past three decades, the optimization of vegetation structure at the plot scale has been defined in the ecological and hydrological fields as various terms including hydrologic equilibrium concepts for terrestrial vegetation or vegetation species distribution at local (Nemani and Running 1989), catchment (Mackay 2001; Caylor *et al.* 2004, 2005), and continental scales (Arris and Eagleson 1994),

minimization of global water stress through tree/grass coexistence (Rodriguez-Iturbe *et al.* 1999a, 1999b), emergent optimal water use properties across different biomes (Huxman *et al.* 2004; Emanuel *et al.* 2007), and the evaluation of carbon and water fluxes with a short-term physiological optimality hypothesis (Hari *et al.* 1999, 2000; Schymanski *et al.* 2008; van der Tol *et al.* 2008a, 2008b). In most cases, the adjustment of the canopy to maximize productivity relative to water availability and flux has been evaluated with respect to one dimensional (vertical) water and nutrient exchange at the ecosystem patch scale, without incorporating lateral moisture redistribution at the landscape scale.

Ecohydrological feedbacks between vegetation patterns and lateral water redistribution have been reviewed in various studies, including interactions between surface runoff generation and patterned vegetation (e.g. 'Tiger bush') in semiarid ecosystems (e.g. Bromley *et al.* 1997; Howes and Abrahams 2003; Ludwig *et al.* 2005; Saco *et al.* 2007), and feedbacks between groundwater hydrology and vegetation especially in riparian ecosystems (e.g. Camporeale and Ridolfi 2006). Spatial patterns of vegetation are often integrated into hillslope-scale hydrological models to explain the active role of vegetation on local water balance and lateral hydrological processes (e.g. Famiglietti and Wood 1994; Wigmosta *et al.* 1994; Chen *et al.* 2005). Mackay (2001) previously evaluated the adjustment of canopy density (leaf area index) to soil moisture and soil nutrients at the hillslope and catchment level, with respect to lateral soil moisture transport.

Determining vertical root profiles and the extent of deep roots has also been a main component of optimality models, as root zone moisture dynamics affect stomatal control on leaf carbon and water exchange, and nitrogen cycling and assimilation (Band *et al.* 2001; Mackay and Band 1997; Mackay 2001; Rodriguez-Iturbe *et al.* 1999a; Porporato *et al.* 2003). Recent studies of optimal rooting strategies have focused on maximum plant water uptake and transpiration in water-limited ecosystems with analytical solutions (Laio *et al.* 2006) and numerical approaches (Collins and Bras 2007). Cost and benefit analysis of deep roots for carbon uptake was also integrated to find the optimal rooting depth strategy at local (Guswa 2008) and global scales (Kleidon and Heimann 1998). In addition,

Schymanski *et al.* (2008) introduced a model of root water uptake dynamically optimizing root surface area to meet the canopy water demand while minimizing carbon costs related to the root maintenance. However, the above models do not simulate shifts of allocation strategies and nutrient availability with changing rooting depth or profiles. Increased allocation to deep roots can lead to decreased allocation to foliar biomass and shallow roots, resulting in less light and nutrient availability.

We explore general principles that would explain the tendency to evolve optimal ecosystem patterns at the hillslope scale, where ecosystem patches exist as part of a drainage chain, or catena, that share some degree of dependency on productivity and resource use with other patches along flowpaths. Optimization has been used to represent a number of different concepts in hydrology and ecology, ranging from maximization of ecosystem functions, to parameter calibrations maximizing model fit to measured runoff. We define optimality here as the maximization of ecosystem functions at the hillslope or catchment scale, such as net primary productivity, evapotranspiration or water use efficiency. We investigate whether these self organizing canopy patterns have the emergent property of maximizing long term (annual to multi-annual) ecosystem net primary productivity, evapotranspiration or water use efficiency at the catchment scale, over and above the optimization at individual patches.

The modeling approach we take is fully transient including short term hydrologic dynamics, long term canopy growth, and soil biogeochemical evolution, and does not incorporate short or long term optimality in the process dynamics. Instead, we use our model to investigate whether hydrological and physiological feedbacks result in the emergent property of catchment scale optimality. The basic concept of this study is that lateral water flux produces important gradients in limiting water and nutrient availability, such as upslope patches condition resource availability downslope. Therefore, in the absence of significant human manipulation, current vegetation density gradients within a hillslope and a catchment can be the result of self-organization between adjacent patches in a catenary sequence of flowpaths. Mackay and Band (1997), and Mackay (2001) used an earlier version of our modeling

approach to demonstrate the adjustment of canopy leaf area gradients along hydrologic flowpaths with soil water and nutrient conditions in catchments in central Ontario and California.

In this study, the model is parameterized with detailed measurements in the Coweeta Long Term Ecological Research (LTER) site. The spatial gradient of vegetation density within a small catchment, estimated with fine-resolution satellite imagery and field measurements, is evaluated with simulated vegetation growth patterns from different rooting and allocation strategies. The modeling study will simulate net primary productivity (NPP) and evapotranspiration (ET) for the different range of vegetation patterns. The goal of this modeling study is to determine if the observed patterns of vegetation density within a small catchment are from long-term ecohydrologic pattern optimization for carbon uptake (e.g. full system productivity or water use efficiency maximization) at the hillslope scale.

2.3 Model overview

This study is based on the use of a process-based ecohydrological model (RHESSys; Regional Hydro-Ecological Simulation System) (Band *et al.* 1993, 2001; Tague and Band 2004; Mackay and Band 1997) and detailed measurements in the Coweeta LTER site.

2.3.1 A Farquhar photosynthesis model

The concept of ecosystem optimality emerged from eco-physiologists (Cowan and Farquhar 1977; Cowan 1982), who developed theories based on principles stating that a maximum amount of carbon is assimilated for a given amount of water loss. Their theory related the stomatal conductance with photosynthesis using a constant water use efficiency concept for short and long-term regulations (referred to as ‘marginal cost’). The Farquhar photosynthesis model (Farquhar *et al.* 1980) hypothesizes that plants optimize stomatal conductivity dynamically for maximizing carbon uptake

with respect to water loss (Cowan and Farquhar 1977; Farquhar *et al.* 2001). Farquhar's equations for C3 plants are controlled by two rate-determining steps in the photosynthetic reaction: a carboxylation rate (A_v) and an electron transport rate (A_j), the minimum of which is the net rate of leaf photosynthesis (A) (Farquhar *et al.* 1980; de Pury and Farquhar 1997).

$$A = \min\{A_v, A_j\} - R_d \quad (2.1)$$

where R_d is daily leaf respiration. In the model, R_d is calculated using reference values at 20 °C and an empirical relationship between leaf nitrogen content and respiration rate (Ryan 1991). Carboxylation limited photosynthesis (A_v) is mediated by Rubisco enzyme, and is referred to as Rubisco-limited photosynthesis (Farquhar *et al.* 1980; de Pury and Farquhar 1997; Farquhar and von Caemmerer 1982).

$$A_v = V_{\max} \frac{C_i - \Gamma^*}{C_i + K_c(1 + O_i / K_o)} \quad (2.2)$$

where K_c and K_o are the Michaelis-Menten constant of Rubisco for CO_2 and O_2 , and C_i and O_i are partial pressure of within leaf CO_2 and O_2 , and Γ^* is the CO_2 -compensation point. Both K and Γ^* are temperature-dependent usually expressed with reference values at 25 °C and their increase ratios with 10 °C increase (Q_{10} values) (Collatz *et al.* 1991). V_{\max} represents the maximum rate of carboxylation, assumed to be a linear relationship with leaf nitrogen content per unit leaf area and Rubisco activity, which includes a temperature-dependent function (de Pury and Farquhar 1997; Chen *et al.* 1999a; Wilson *et al.* 2000).

Electron transport limited photosynthesis (A_j) is catalyzed by Ribulose-bisphosphate carboxylase-oxygenase (RuBP) enzyme, often called RuBP-limited photosynthesis (Farquhar *et al.* 1980; de Pury and Farquhar 1997; Farquhar and von Caemmerer 1982).

$$A_j = J \frac{C_i - \Gamma_*}{4.5C_i + 10.5\Gamma_*} \quad (2.3)$$

where J is the electron transport rate, calculated from a quadratic equation as a function of effective irradiance (I_e) and the maximum electron transport rate (J_{max}). A fixed ratio (2.1; Wullschlegel 1993) is usually assumed between J_{max} and V_{max} even though this ratio can vary with temperature sensitivities of both components.

2.3.2 Coupled photosynthesis – stomatal conductance models

Many stomatal conductance (g_s) models (e.g. Chen *et al.* 1999a; Baldocchi *et al.* 1991; McMurtrie *et al.* 1992; Sellers *et al.* 1992; Leuning 1995; Oren and Pataki 2001; Kim *et al.* 2008) use an empirical equation from (Jarvis 1976), which assumes that environmental factors act independently to control stomatal conductance.

$$g_s = g_{s,max} f(VPD) f(\psi) f(APAR) f(CO_2) \quad (2.4)$$

where $g_{s,max}$ is the maximum stomatal conductance for water, $f(\cdot)$ are linear or non-linear scalar functions that evaluate between 0 and 1 for VPD (vapor pressure deficit), ψ (soil water potential), $APAR$ (absorbed photosynthetically active radiation per unit leaf area), and CO_2 (atmospheric concentration of carbon dioxide).

Stomatal conductance is the key link between carbon uptake and water leakage because gas exchange through stomata is usually assumed to be dominated by a diffusion process following concentration gradients under a steady-state assumption (Cowan and Farquhar 1977). Stomatal conductivity for CO_2 (g_c) can be calculated by dividing the above g_s with a constant factor (set to 1.6; Cowan and Farquhar 1977) which accounts for the ratio of atmospheric diffusivities between water

vapor and CO₂ (Leuning 1995). The rate of CO₂ transport across stomata (A) can be expressed as a function of stomatal conductivity for carbon (g_c) and a concentration gradient term ($C_a - C_i$) (Cowan and Farquhar 1977).

$$A = g_c (C_a - C_i) \quad (2.5)$$

A_v from Eq. 2.2 and A_j from Eq. 2.3 can be solved using the quadratic equation, by substituting C_i from the above equation (Farquhar and von Caemmerer 1982; Chen *et al.* 1999a). Note that stomatal conductance and photosynthesis are all unit leaf area basis, not unit ground area basis, which would be scaled up with dynamic separation between sunlit and shaded leaves.

2.3.3 *Scaling up fluxes from leaves to canopy*

Many coupled modeling efforts show that dynamic separation between sunlit and shaded leaves is the most efficient way to represent different rate determining factors for photosynthesis with canopy depth profile without multi-layer simulations (de Pury and Farquhar 1997; Chen *et al.* 1999a; Wang and Leuning 1998). Following Chen *et al.* (1999a), total sunlit leaf area index (LAI) (LAI_{sunlit}) is defined as

$$LAI_{sunlit} = 2 \cos \theta (1 - \exp(-0.5 \Omega LAI / \cos \theta)) \quad (2.6)$$

where θ is sun zenith angle, and Ω is the foliage clumping index. Shaded LAI (LAI_{shade}) is $LAI_{shade} = LAI - LAI_{sunlit}$. Dynamic weighting is applied to calculate canopy-scale stomatal conductance (g_s), and photosynthesis (A) per unit ground area.

$$g_s = g_{s,sunlit} LAI_{sunlit} + g_{s,shade} LAI_{shade} \quad (2.7)$$

$$A = A_{sunlit} LAI_{sunlit} + A_{shade} LAI_{shade} \quad (2.8)$$

This dynamic separation between sunlit and shaded leaves is justified in that the upper canopy is usually light-saturated whereas the lower canopy responds linearly to irradiance, which should result in a vertical distribution of leaf nitrogen and specific leaf area for their optimal exploitation (Field 1983; de Pury and Farquhar 1997).

2.3.4 Nitrogen limitation

Most temperate forests are limited by nutrients, in particular nitrogen (Vitousek and Howarth 1991; Schimel *et al.* 1997; Nadelhoffer *et al.* 1999; Oren *et al.* 2001). Most ecohydrological catchment models usually incorporate only soil moisture patterns into vegetation dynamics, derived by topographic position, local soil texture, and available rooting depth information without nutrient limitation (Wigmosta *et al.* 1994; Rodriguez-Iturbe *et al.* 1999a; Porporato *et al.* 2002; Ivanov *et al.* 2008; van der Tol *et al.* 2008b) and are often applied in strictly water-limited ecosystems.

The spatial distribution of plant-available nitrogen is also closely related to local soil moisture dynamics, which itself is a composite result of micro-climate condition, local soil texture, and local vegetation; both directly (e.g. mineralization, nitrification, denitrification, and leaching) and indirectly through plants (e.g. translocation, residues decomposition, and nitrogen fixation) (Band *et al.* 2001; Creed and Band 1998a, 1998b; Mackay and Band 1997; Mackay 2001; Porporato *et al.* 2003). Figure 2.1 shows the adjustment of nitrogen transformation rates as a function of soil moisture content following Parton *et al.* (1996), which determines a direct topographic effect on spatial patterns of plant-available nitrogen. Note that available nitrogen content would be most available around 60% of volumetric soil water saturation for sandy loam soil by increasing anaerobic condition of soil at high soil moisture content, where denitrification process is more active.

The nitrogen cycle in the model is largely based on the BIOME-BGC model (Running and Coughlan 1988; Running and Hunt 1993; Kimball *et al.* 1997; Thornton *et al.* 2002) for vegetation and the CENTURY_{NGAS} model (Parton *et al.* 1996) for soil. The model assumes stoichiometrically constant ratios between carbon and nitrogen (C/N ratio) for all vegetation compartments (leaf, litter, fine root, live wood, and dead wood) and soil pools (Tague and Band 2004). At a daily time step, all soil/litter pools calculate the potential immobilization and decomposition rates based on soil water and temperature. If nitrogen availability cannot satisfy the sum of potential microbial uptake (immobilization) and plant growth demands (plant uptake), these two demands compete for available soil mineral nitrogen. Plants can also use an internally-recycled nitrogen pool translocated from turnover of leaves and live vegetation parts (stem, coarse root) for remaining demands for nitrogen. Available nitrogen also includes atmospheric deposition, fertilization, or symbiotic/asymbiotic fixation. Detailed explanations are available in the works of Thornton (1998), and Tague and Band (2004).

2.3.5 Allocation

The amount of fixed carbon available to the leaf depends on subsequent metabolic events after photosynthesis, called allocation, which includes the storage, utilization and transport of fixed carbon in the plant (Taiz and Zeiger 2002). Interannual effects of climate factors on vegetation are largely from translocation of these stored carbohydrates to leaves in the early growing season. In the model, these allocation dynamics depend on mixed daily and yearly allocation strategies related to temporal phenological changes (Figure 2.2) (Running and Hunt 1993; Thornton 1998; Thornton *et al.* 2002). Daily gross photosynthesis is allocated to both vegetation and storage (available for budburst in the following growing season) at a constant ratio after considering autotrophic respiration (maintenance and growth respirations). Transfer from storage to vegetation compartments occurs during the prescribed growing season. Leaf and fine root turnovers occurs only during the prescribed leaf-fall season, whereas those for live stem and coarse root occur at a constant rate throughout the year.

Biogeochemical models usually do not simulate actual tree stands which incorporate tree seedling, recruitments, and mortality (Friend *et al.* 1997). Only total plant mortality is simulated which describe the portion of the plant pools either replaced each year or removed through fire or plant death.

Note that LAI is not prescribed into the model, but the model is self-regulating with respect to LAI based on photosynthate production, respiration, and allocation processes. Optimality models that prescribe aboveground vegetation density and belowground biomass (or rooting depth) usually neglect the feedbacks and constraints of previous, transient carbon, water and nutrient balance. Allocation processes compromise between light, water, and nutrients proportioning fixed carbon into different vegetation compartments based on limiting resources (Tilman 1988; Gedroc *et al.* 1996; McConnaughay and Coleman 1999).

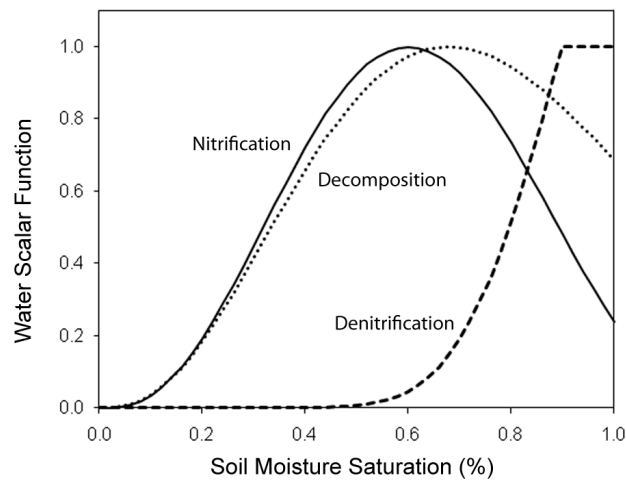


Figure 2.1: Water scalar functions of nitrogen transformation rates as a function of soil moisture saturation for sandy loam soils; after Parton *et al.* (1996).

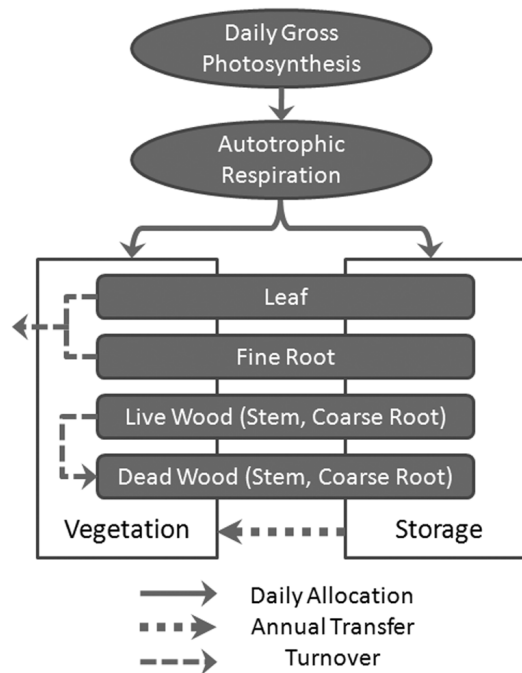


Figure 2.2: A compartment flow diagram of carbon allocation, transfer, and turnover with mixed daily and yearly allocation strategies following the current BIOME-BGC algorithm (Thornton *et al.* 2002; Thornton 1998).

2.4 Materials and methods

2.4.1 Site description

The Coweeta Hydrologic Lab is located in western North Carolina and is representative of the Southern Appalachian forest. The Southern Appalachian forest has very diverse flora as a result of combined effect of terrain, microclimate and soil moisture (Whittaker 1956; Day and Monk 1974). Mean monthly temperature varies from 3.6 °C in January to 20.2 °C in July. The climate in the Coweeta Basin is classified as marine, humid temperate, and precipitation is relatively even in all seasons; annual precipitation ranges from 1870 mm to 2500 mm with about a 5% increase with 100 m (Swift *et al.* 1988). The dominant canopy species are oaks and mixed hardwoods including *Quercus* spp. (oaks), *Carya* spp. (hickory), *Nyssa sylvatica* (black gum), *Liriodendron tulipifera* (yellow poplar), and *Tsuga canadensis* (eastern hemlock), while major evergreen undergrowth species are *Rhododendron maximum* (rhododendron) and *Kalmia latifolia* (mountain laurel) (Day and Monk 1974; Day *et al.* 1988). The main study site is Watershed 18 (WS18), a northwest-facing, steeply sloping (average 52% slope), 13-ha catchment with an elevation range from 726 to 993 m (Figure 2.3c). This study site is a control watershed with mixed hardwoods stands undisturbed since 1927. Soil moisture is a primary control on vegetation patterns within WS18, despite the high annual rainfall (Day and Monk 1974; Day *et al.* 1988).

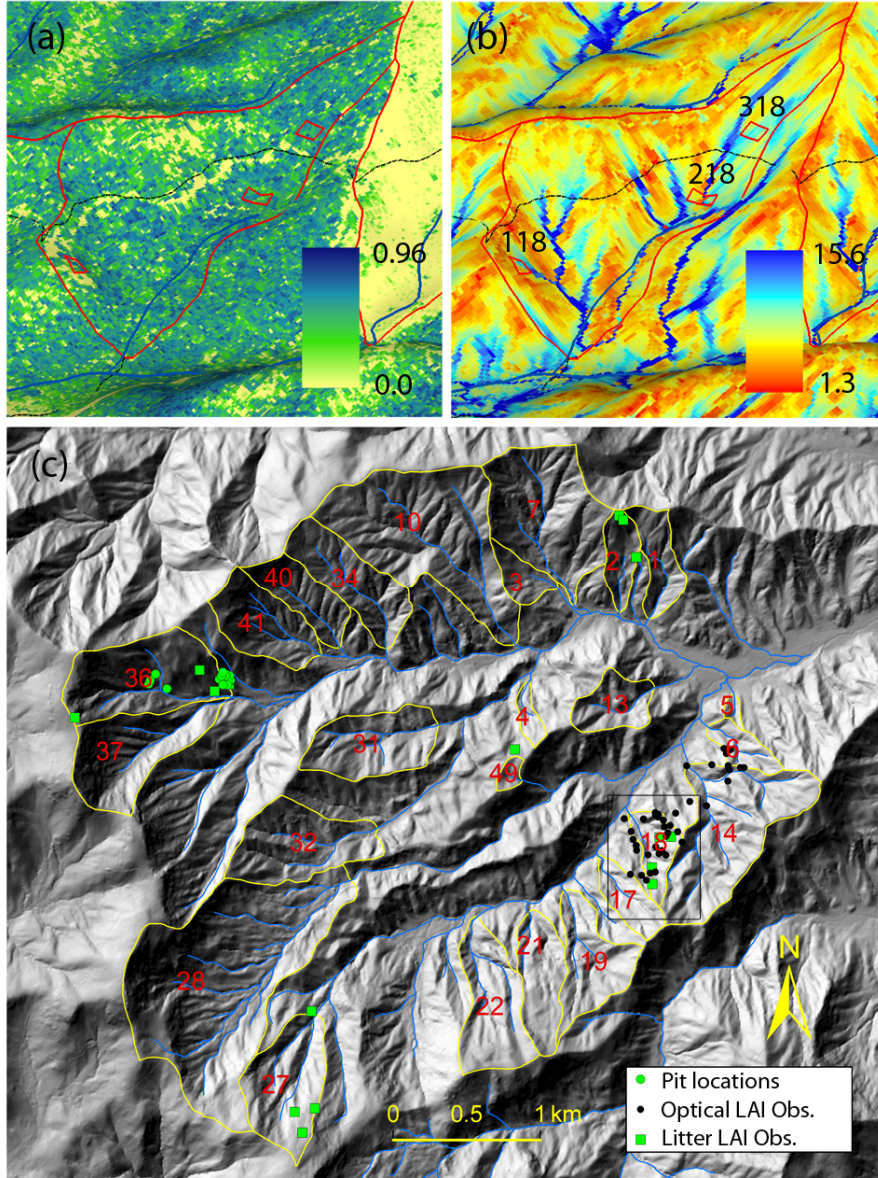


Figure 2.3: Study site (WS18); (a) NDVI (normalized difference vegetation index) from a June 1, 2003 IKONOS image, (b) wetness index, and (c) locations for WS18 (square), LAI (leaf area index) measurements, and soil pits within the Coweeta LTER site. Litter LAI points are from Bolstad *et al.* (2001). Red and yellow lines represent the boundaries of watersheds, and dashed lines indicate roads along which artificial gaps are shown. (a) and (b) are perspective views from the WS18 outlet. The rectangles within WS18 are three gradient plots (118, 218, and 318). A paired experimental watershed (WS17) is also shown next to the target watershed where white pines (*Pinus strobus* L.) are planted in 1956 after 15-year clear cut periods.

2.4.2 *Climate data and historical field measurements*

Daily climate (maximum and minimum daily temperature, daily precipitation; CS01/RG06 climate station) and streamflow data (WS18; Coweeta LTER research data ID 3033) are available from 1937, one of the longest hydrological records for forested headwater catchments in the world. For the model simulation, we used universal kriging with elevational trends from 7 points measurements within the Coweeta basin from 1991 to 1995 to develop long-term rainfall isohyets to scale daily precipitation over the terrain.

Three LTER research plots have been established along a topographic gradient at high, mid and low catchment positions (118 - xeric, 218 - mesic, and 318 – intermediate) to study ecohydrologic trends within the study watershed (Figure 2.3b), where detailed vegetation, soil and various microclimate data are available. Detailed explanations of these gradient plots are available at the Coweeta LTER homepage (http://coweeta.ecology.uga.edu/gradient_physical.html). We use daily volumetric water content data (Coweeta LTER research data ID 1013) collected with 30-cm CS615 sensors (Water Content Reflectometer, Campbell Scientific Inc., Logan, UT, USA) every 15 minutes from March 1999. At each gradient plot, these TDR sensors are installed at different depths (0 ~ 30 and 30 ~ 60 cm) and at two locations (upper slope and lower slope) within 20 × 40 m original rectangular plots.

Aboveground net primary productivity (ANPP) was estimated from tree ring increments and litterfall measurements in the early 1970's for the full watershed (Day and Monk 1974, 1977; Day *et al.* 1988). Biomass increases were estimated from tree ring increments with locally-derived biometric equations for each species (Day and Monk 1974, and references therein). Recently, Bolstad *et al.* (2001) also estimated ANPP at four circular 0.1 ha plots within the watershed (site number 3, 4, 13, 14) from 2-year litterfall (1995 ~ 1996) and 10-year tree ring measurements (1986 ~ 1995).

2.4.3 Hydrologic gradients of vegetation density

Leaf area index (LAI), an important carbon state variable in process-based biogeochemical models, is also a valuable driver in the scaling effort as it is well correlated with normalized difference vegetation index (NDVI) derived from remote sensing images (Nemani *et al.* 1993; Gholz *et al.* 1991; Chen and Cihlar 1996; Fassnacht *et al.* 1997). The NDVI is a normalized ratio between red and near infrared bands.

$$NDVI = (\rho_{NIR} - \rho_{RED}) / (\rho_{NIR} + \rho_{RED}) \quad (2.9)$$

LAI values were measured at 39 points around the WS18 in early June 2007 using two different methods (Figure 2.3c), with GPS coordinates measured during the previous leaf-off season (GeoExplorer; Field Data Solutions Inc., Jerome, ID, USA). LAI was measured with an LAI-2000 Plant Canopy Analyzer (LI-COR Inc., Lincoln, NE, USA) using two instruments simultaneously for above and below canopy during overcast sky condition or at dawn or at dusk. Hemispheric images were also taken at the same sites, and analyzed with the Gap Light Analyzer software (Institute of Ecosystem Studies, Millbrook, New York, USA). We also used LAI data estimated from litter biomass and specific leaf area around the Coweeta LTER site (Figure 2.3c), four of which are located within WS18 (Bolstad *et al.* 2001). These litter-trap measurements are quite valuable in that optical measurements usually do not show much sensitivity in ranges of high leaf area index (Nemani *et al.* 1993; Fassnacht *et al.* 1997; Pierce and Running 1988; Gower and Norman 1991).

Spatial patterns of LAI within the watershed were determined from the site-specific correlation between point-measured LAI and NDVI values from a summer IKONOS Image (June 1, 2003; Figure 2.3a) with varying average window size of NDVI pixels and masking from outmost rings in a sequence for optical LAI calculation. Optical measurements of vegetation using LAI-2000 in complex terrain can be biased by topographic interference especially in the outer rings. We found the best

match between LAI calculations of $0^\circ \sim 23^\circ$ zenith ranges (1 and 2 rings) and NDVI values by a 3×3 averaging window (Figure 2.3a). Considering average canopy height (~ 16 m) within the watershed and 4-meter IKONOS pixel size, this match is quite reasonable in terms of their size correspondences.

Most LAI measurements are located along the regression line except for some outliers (Figure 2.4a), from which we estimated spatial patterns of vegetation density within the target watershed. These outliers are mostly from the sites where thick rhododendron (*R. maximum*) develops in understory canopy. Dense understory canopy can easily decouple upward ground optical measurements and downward remote sensing images, and also affects NDVI values which are very sensitive to canopy background variations (Huete 1988; Huete *et al.* 1994).

Hydrologic gradients of vegetation density were calculated by grouping 10×10 m patches at equal wetness index intervals (0.5) to suppress noises, where only groups over ten pixels were counted (Figure 2.4b). Wetness index (or topographic index; Beven and Kirkby 1979) was calculated from 6.1-m (20 ft.) LIDAR elevation data (Figure 2.3c) representing hydrological gradients in the TOPMODEL algorithm. Upslope contributing area for wetness index was calculated from *D*-infinity (D_∞) method allowing flow to be proportioned between multiple downslope pixels according to gradient (Tarboton 1997). A 30-m buffer area along the road is masked in this analysis to exclude artificial vegetation gaps (Figure 2.3a).

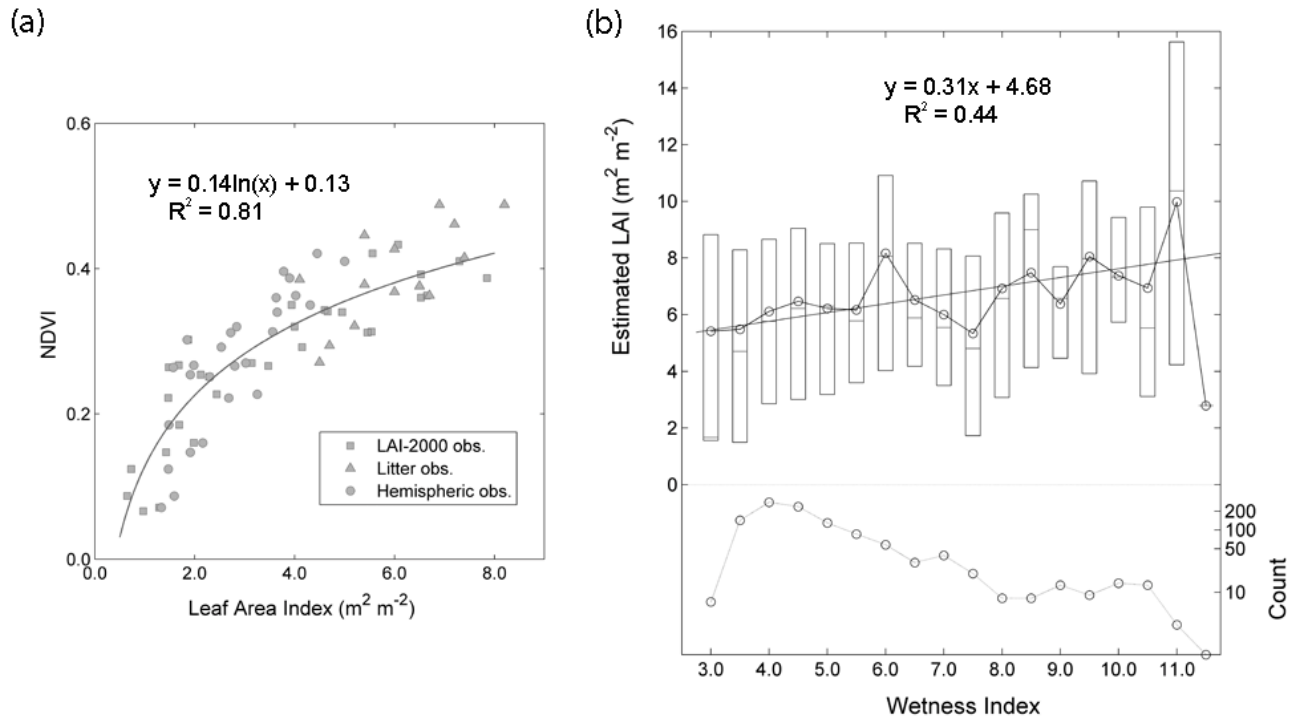


Figure 2.4: (a) A scatter plot between LAI (leaf area index) measurements and NDVI (normalized difference vegetation index), and (b) hydrologic gradients of estimated LAI within the study watershed. Litter LAI measurements are from Bolstad *et al.* (2001). Circles represent average values, and box plots have lines at the lower quartile, median, and upper quartile values from each binned group. Counts are the number of $10 \times 10 \text{ m}$ patches in each group, which are basic units of model simulation.

2.4.4 Rooting depth and root distributions from soil pits

Hales *et al.* (2009) estimated spatial distributions of root depth, with 15 manually excavated soil pits around WS36 (Figure 2.3c), undisturbed since 1919. WS36 has steeper topography (average 65 % slope) with steeper gradients of vegetation density (not shown here) than the study watershed (WS18). We did not excavate in WS18 as it is now preserved and adjacent catchments are recently disturbed (e.g. selective logging). Nine pits were located close to the watershed outlet, while another four pits were excavated higher in the watershed (Figure 2.3c). Soils are all sandy-silt loam inceptisols with a typical colluvial appearance.

Pits were dug with horizontal dimensions of approximately 100 cm by 150 cm, with depth varying between 120 cm and 180 cm due to difficulties excavating pits below the saprolite layer. Each pit was located downslope (within 0.8 m) from an individual specimen of one of the major hardwood species within the Coweeta LTER site (Table 2.2). Pit locations were carefully chosen in the field based on topographic positions, classified based on their curvature as ridge, sideslope, and hollow (Table 2.1). From GPS coordinates and the LIDAR data, the average wetness index of ridge pits was computed to be 3.79, while that of hollow pits was 5.65. Note that on-site curvature is a more robust method to determine topographic positions for each tree, because even detailed elevation information (e.g. LIDAR) cannot decide a hillslope position of each tree for geolocation or scale problems.

Summaries of soil pit measurements are available in Table 2.1. Detailed methods of pit construction, root frequency, and diameter measurements are described in Hales *et al.* (2009). Note that the limited number of measurements was due to careful hand-digging to sample fine root structures. The vertical distribution of roots was quantified by counting roots, where the cumulative frequency function of roots was drawn to determine rooting depth and vertical root distribution.

Table 2.1: Detailed measurements for soil pits at different topographic positions

Topographic positions	Species	DBH (cm)	Wetness index	Rooting depth (RD_{95}) (m) ^a
ridge	<i>Acer rubrum</i>	5.1	4.12	1.00
	<i>Acer saccharum</i>	20.9	3.10	1.01
	<i>Carya</i> spp.	38.8	3.97	0.90
	<i>Liriodendron tulipifera</i>	20.1	4.08	0.60
	<i>Quercus prinus</i>	58.7	2.59	0.93
	<i>Quercus rubra</i>	33.2	4.12	1.02
	<i>Rhododendron maximum</i> ^b	9.2	4.61	0.98
	<i>Tsuga canadensis</i> ^b	33.9	3.70	0.57
	Average	27.5	3.79	0.88
sideslope	<i>Liriodendron tulipifera</i>	17.5	3.89	0.74
hollow	<i>Betula lenta</i>	28.5	4.20	0.91
	<i>Liriodendron tulipifera</i>	22.5	5.38	0.94
	<i>Quercus rubra</i>	84.0	4.60	1.21
	<i>Quercus rubra</i>	37.7	7.89	0.71
	<i>Quercus velutina</i>	33.7	5.88	0.75
	<i>Rhododendron maximum</i> ^b	4.3	5.93	0.92
	Average	35.1	5.65	0.91

^aDefined from 95% cumulative distribution of root counts; ^bNote that these species are not deciduous broadleaf.

Table 2.2: Species-specific eco-physiologic model parameters^a

Vegetation species	Percent basal area ^b	Specific leaf area (SLA)	Shaded to sunlit SLA ratio	Leaf CN ratio	Maximum leaf conductance	Photosynthetic parameter	Q ₁₀ for autotrophic respiration	Maximum rate of carboxylation
	(%)	(m ² kg C ⁻¹)	(unitless)	(unitless)	(m s ⁻¹)	(unitless)	(unitless)	(μmol CO ₂ m ⁻² s ⁻¹)
<i>Quercus prinus</i>	21.3	17.8 (22)	2.21 (24)	25.9 (85)		0.0234 (94)	2.33 (31)	14.54 (94)
<i>Acer rubrum</i>	9.3	25.8 (18)	1.78 (22)	18.5 (103)	0.0058 (NA)	0.0167 (221)	2.43 (40)	7.24 (221)
<i>Quercus coccinea</i>	7.9	19.0 (13)	1.39 (18)	18.8 (80)	0.0083 (NA)	0.0133 (84)	2.37 (25)	27.53 (84)
<i>Quercus rubra</i>	6.8	20.8 (15)	1.74 (24)	26.4 (88)		0.0213 (27)	2.42 (27)	12.77 (27)
<i>Liriodendron tulipifera</i>	6.4	26.8 (18)	1.60 (18)	24.2 (85)	0.0110 (NA)	0.0248 (91)	2.24 (29)	10.18 (91)
<i>Carya glabra</i>	5.1	23.8 (20)	1.69 (24)	21.3 (90)		0.0217 (99)	2.46 (36)	9.42 (99)
<i>Kalmia latifolia</i>	5.1	18.9 (NA)		11.5 (NA)	0.0042 (NA)			
<i>Oxydendrum arboreum</i>	4.4	52.4 (10)	1.03 (8)	20.0 (64)			3.02 (14)	
<i>Nyssa sylvatica</i>	3.7					0.0285 (32)		5.62 (32)
<i>Cornus florida</i>	3.2	29.6 (8)	1.78 (9)	21.2 (65)		0.0662 (20)	2.60 (11)	3.40 (20)
<i>Betula lenta</i>	2.7	34.0 (21)	1.68 (21)	25.4 (79)		0.0115 (290)	2.71 (27)	16.95 (290)
<i>Rhododendron maximum</i>	7.4	48.9 (NA)		10.2 (14)	0.0033 (NA)		2.54 (7)	
Weighted average		23.8	1.66	22.1	0.0065	0.0229	2.43	11.37
References	1	2,3,4,5	3	2,3,4,6	4	8	6,9	8

^aDetailed explanations of parameters are available in White *et al.* (2000); ^bAll species under 2% (29 species) are not considered. Numbers in parenthesis are sample sizes. NA represents non-available. References are as follows: (1) Day *et al.* (1988), (2) Martin *et al.* (1998), (3) Mitchell *et al.* (1999), (4) Reich *et al.* (1999), (5) Bolstad *et al.* (2001), (6) Vose and Bolstad (1999), (7) Vose and Bolstad (2006), (8) Sullivan *et al.* (1996), (9) Bolstad *et al.* (1999).

2.4.5 *Model parameterization*

The model is simulated at 10×10 m grid cell resolution (patch; $n = 1253$), which we treat as control volumes for biogeochemical and hydrological processes. Many species-specific physiological parameters (Table 2.2) and other (e.g. soil, nutrient) parameters (Table 2.3) were measured intensively within WS18 and Coweeta LTER site. We calculated representative physiological parameters at the whole catchment scale with these species-specific parameters weighted by vegetation composition within the study watershed (Table 2.2). We did not simulate the model at the species level, because a detailed vegetation species map is not available and some physiological parameters (e.g. allocation, phenological parameters) are not measured at the species level. Phenological parameters (Table 2.3) are estimated from 8-day composite MODIS (MODerate Resolution Imaging Spectroradiometer) satellite images for five years (2001 ~ 2005), aggregated to the 5×5 km grid scale large enough to include the whole Coweeta basin (21.8 km^2) and minimize geolocation problems.

Lateral hydrologic connectivity within the study watershed is defined by calibrating the model with streamflow data varying the TOPMODEL parameters, m (the decay rate of hydraulic conductivity with depth), and the lateral/vertical K_{sat0} (saturated hydraulic conductivity at surface). Monte-Carlo simulation was implemented three thousand times with randomly sampled parameter values within certain acceptable ranges. A three-year calibration period (October 1999 ~ September 2002) was chosen to include extreme drought precipitation patterns (Figure 2.5) for better representations of soil moisture status during drought periods. To allow soil moisture to stabilize, a one and a half year initialization was employed before the calibration period. The Nash-Sutcliffe (N-S) coefficient (Nash and Sutcliffe 1970) for lognormal streamflow discharge was used to evaluate model performance because this objective function is biased toward base flow, closely related to soil moisture status in this study area (Hewlett 1961). A maximum efficiency value of the calibration period was 0.802, whereas that of a 16-year validation period was 0.873 (Figure 2.5).

Table 2.3: Other model parameters

Parameters ^a	Value	Unit	References
<i>Eco-physiological Parameters</i>			
CN ratio of leaf litter	34.8		
fine root	51.1	Unitless	1, 2
live wood	75.6		
Q_{10} value for heterotrophic respiration	3.56	Unitless	3
Allocation parameters			
Fine root to leaf carbon	1.21		
Stem to leaf carbon	1.0	Unitless	4, 5, 6, 7
Live wood to total wood carbon	0.16		
Coarse root to stem carbon	0.22		
Light extinction coefficient (k)	0.54	Unitless	8
Phenological parameters			
Start day of leaf on	105	DOY	
Start day of leaf off	260	DOY	5, 6
Length of growth period	35	days	
Length of senescence period	50	days	
Whole plant mortality	0.5	Percent	8,10, 11
<i>Soil texture parameters</i>			
sand	55.2		
clay	16.9	percent	12, 13, 14
silt	27.9		
<i>Nitrogen input parameters</i>			
Wet nitrogen deposition rate	0.0010	kg N m ⁻² y ⁻¹	15
Biological nitrogen fixation rate	0.0011		16

^aDetailed explanations of parameters are available in White *et al.* (2000). References are as follows: (1) Martin *et al.* (1998), (2) Vose and Bolstad (2006), (3) Bolstad and Vose (2005), (4) McGinty (1976), (5) Day and Monk (1977), (6) 5-year MODIS data (2001 ~ 2005), (7) Monk and Day (1988), (8) White *et al.* (2000), (9) Sullivan *et al.* (1996), (10) Elliott and Swank (1994), (11) Clinton *et al.* (2003), (12) Zak *et al.* (1994), (13) Yeakley *et al.* (1998), (14) Unpublished data from Todd Lookingbill, (15) Knoepp *et al.* (2008), (16) Todd *et al.* (1975).

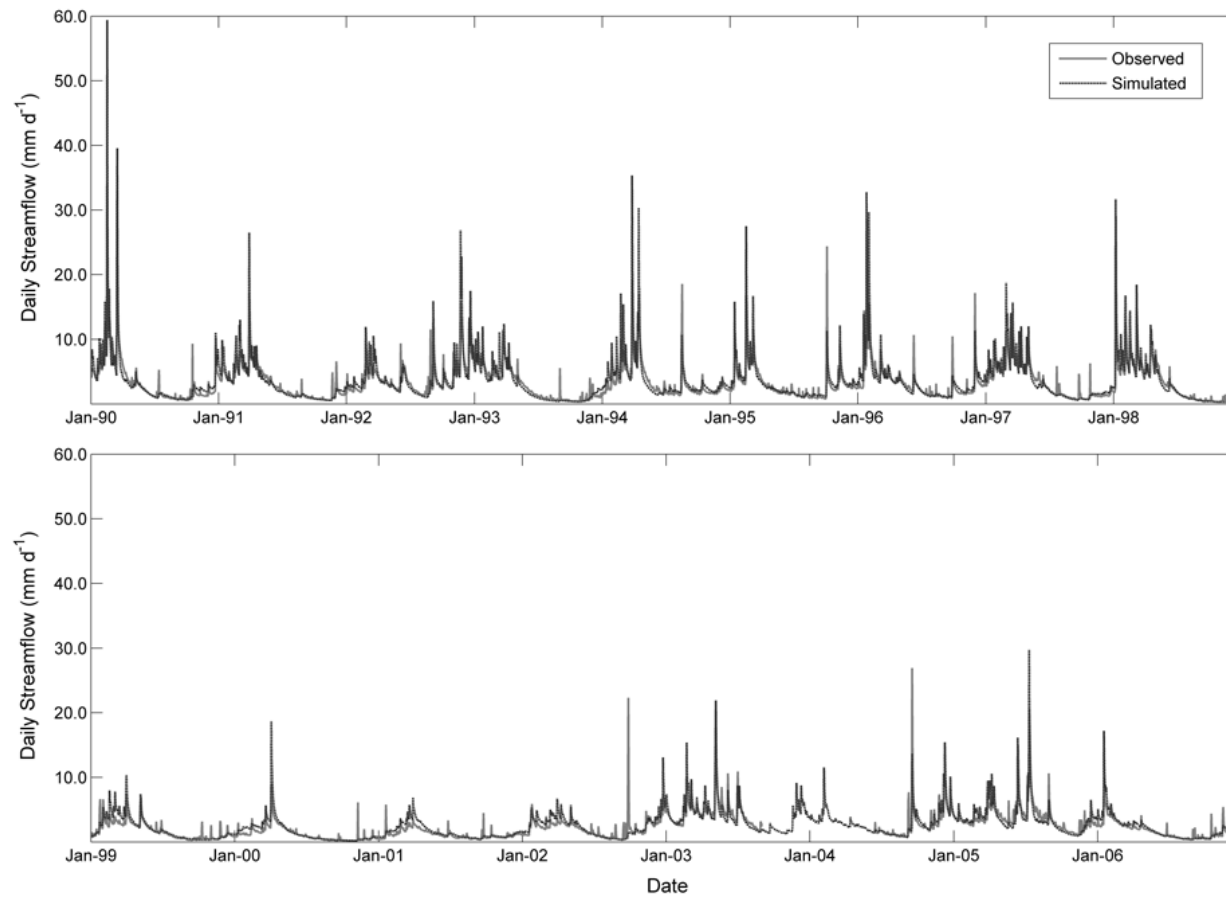


Figure 2.5: Long-term observed and simulated daily streamflow at the study watershed (1990 ~ 2006), including the 3-year calibration period (October 1999 ~ September 2002).

We show fairly good agreement between measured and simulated soil moisture content (1999 ~ 2006) at upper 60-cm soil depth from three gradient plots that range from xeric to wet soil conditions (Figure 2.6). Therefore, reasonable spatio-temporal patterns of root zone moisture dynamics further constrains model parameterization in addition to streamflow data within the watershed.

Figure 2.7 shows key long term nitrogen transformation rates along the hillslope gradient, simulated based on the current vegetation gradients and the defined lateral hydrologic connectivity. In this area, nitrogen is cycled tightly with increasing mineralization and uptake rates downslope. A small proportion of available nitrogen is nitrified, with significant denitrification restricted to the wettest parts of the catchment. The difference in mineralization and plant N uptake is largely explained by atmospheric deposition ($< 1.0 \text{ g N m}^{-2} \text{ y}^{-1}$; Knoepp *et al.* 2008), and fixation ($1.1 \text{ g N m}^{-2} \text{ y}^{-1}$; Todd *et al.* 1975). We point out that these gradients largely from in situ N cycling as we did not include lateral transport of mobile nitrogen (nitrate), or mass transport of organic litter downslope in the model version we used.

2.4.6 *Prescribed rooting depth as a function of hillslope position*

Lateral water flux through shallow soil columns is dominant in these mountainous forest catchments (Hewlett and Hibbert 1963), which results in uneven distribution of plant available water along hydrologic flowpaths (Yeakley *et al.* 1998). The spatial pattern of vegetation density within a watershed is a good estimator for spatial patterns of root zone moisture dynamics and lateral connectivity within watersheds. However, temporal dynamics of plant available water are dependent not only on hillslope position, but also on local properties like soil texture (Porporato *et al.* 2001; Brady and Weil 2002) and rooting depth (Oren and Pataki 2001; Schenk and Jackson 2002).

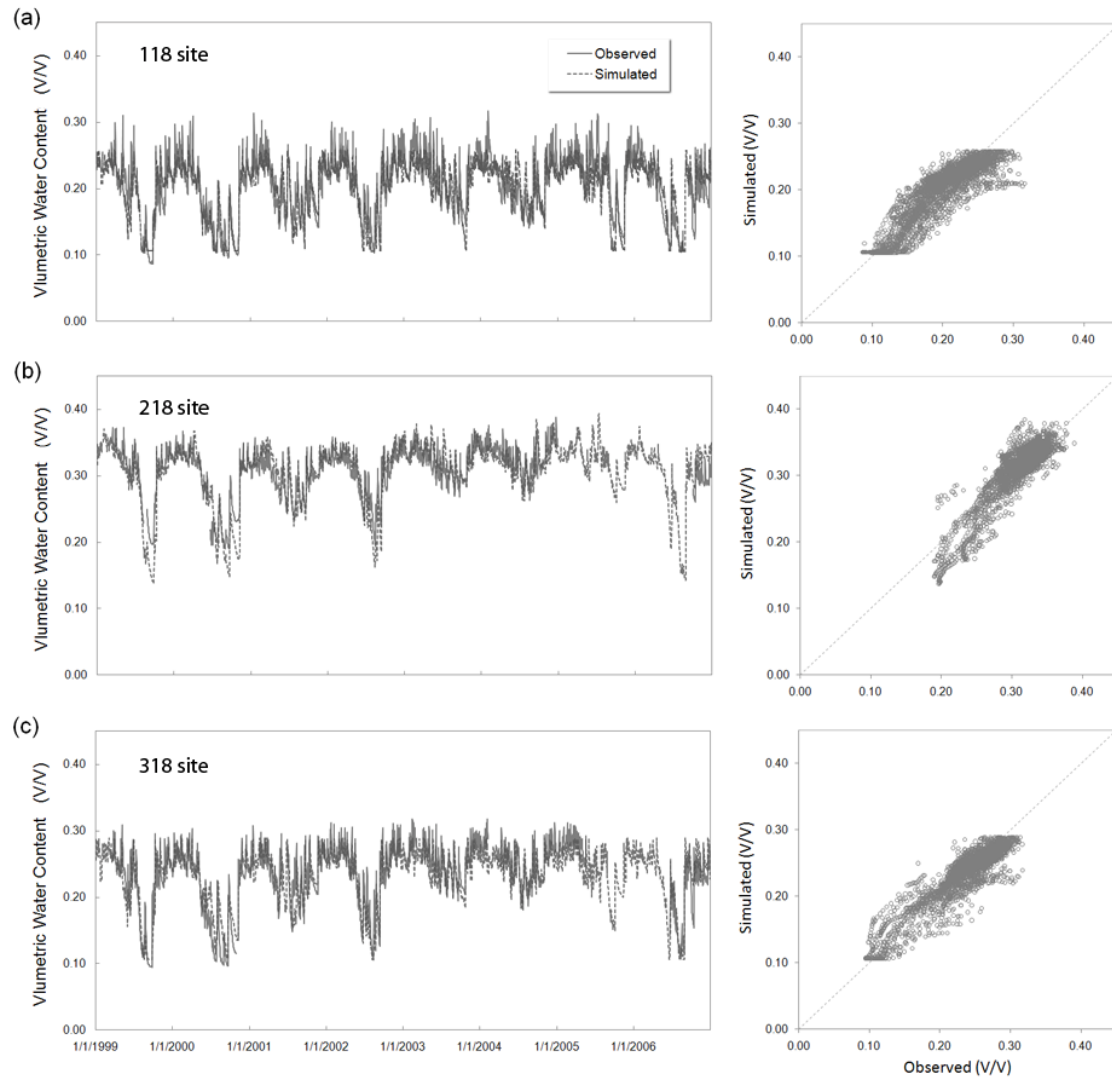


Figure 2.6: Time series and scatter plots of observed and simulated soil water content at (a) 118 (xeric), (b) 218 (mesic), and (c) 318 (intermediate) gradient plots within the target watershed (Figure 2.3b).

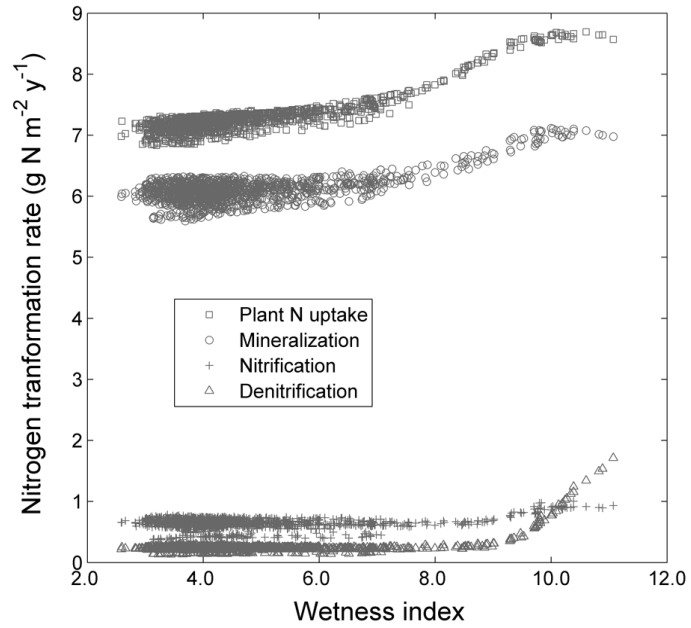


Figure 2.7: Simulated long term (1941 ~ 2005) nitrogen transformation rates (plant uptake, mineralization, nitrification, and denitrification) in litter and soil as a function of wetness index. Note that these modeled gradients largely result from in situ N cycling as lateral transport of mobile nitrogen (nitrate), or organic litter downslope is not included in the simulation version. Each point represents a 10 × 10 m cell ($n = 1253$), a basic unit of model simulation.

We use maximum rooting depth in this study, rather than the usual definition of rooting depth (the depth of 95% cumulative distribution of root biomass; Arora and Boer 2003). Maximum rooting depth represents temporal dynamics of plant available water better as the deepest 5% of roots may play an important role for vegetation transpiration especially during a dry season (Nepstad *et al.* 1994; Canadell *et al.* 1996; Jackson *et al.* 1999).

Soil and vegetation may also vary systematically as a function of topographic position. Colluvial soils are thicker and slightly finer in wet and convergent topography with mesic species, but thinner and coarser in dry and divergent topography with xeric species in this area (Day *et al.* 1988; Yeakley *et al.* 1998; Hales *et al.* 2009). To reflect these local properties, a local rooting depth (RD) is expressed as a linear function of local wetness index (WI) with two rooting depth parameters, average rooting depth (RD_{avg}) and spatial pattern of rooting depth (RD_{dev}).

$$RD = RD_{avg} + RD_{dev} \times (WI - WI_{avg}) \quad (2.10)$$

where WI_{avg} represents the average wetness index within the hillslope. The spatial pattern of rooting depth (RD_{dev}) parameter is the change in rooting depth with unit increase of wetness index, hence a positive value means increasing rooting depth in a downslope direction.

Soil texture variation within the watershed is small, and we do not incorporate specific patterns in model parameterization. The model is then further calibrated by Monte-Carlo sampling of RD_{avg} and RD_{dev} using degree-of-fit between simulated and estimated hydrologic gradients of vegetation density (Figure 2.4b). Different combinations of RD_{avg} and RD_{dev} result in variations in spatial patterns of LAI due to variations in water and nutrient availability, resulting photosynthesis, and allocation dynamics. The minimum rooting depth was set as 0.2 m to avoid numerical problems in the vertical hydrological processes in the model.

2.4.7 Allocation dynamics with varying rooting depth

We used a constant allocation strategy between vegetation compartments (e.g. leaf, stem, fine root, coarse root) in the model, from the current BIOME-BGC algorithm (Thornton 1998; Thornton *et al.* 2002). Allocation parameters are estimated from detailed field measurements of aboveground woody biomass increase, annual foliage productions, and root biomass dynamics around the study site (Table 2.3) (Day *et al.* 1988; Day and Monk 1977; McGinty 1976). Specifically, McGinty (1976) measured actual root growth dynamics by re-filling three excavated pits over a two year period, providing information to calculate rough estimates for allocation ratios between vegetation compartments. He also measured the vertical distribution of root biomass in the mixed hardwood forest from twenty pits around the study area (WS14, WS22, and WS27), from which we estimate maximum rooting depth.

However, the allocation scheme can respond to local water availability, determined by a hillslope position and local properties. Many studies show that decreasing resource availability (water and nutrients) can favor partitioning more carbon belowground, in terms of climatic gradients (Schenk and Jackson 2002; Hui and Jackson 2006) and field experiments (Gedroc *et al.* 1996; McConnaughay and Coleman 1999; Cromer and Jarvis 1990; Ryan *et al.* 2004; Litton *et al.* 2007). For this reason, there is a long history of modeling efforts to integrate this dynamic allocation scheme based on light, water, and nutrient availability (see Mackay 2001; Wilson 1988; Running and Gower 1991; Friedlingstein *et al.* 1999).

In this study, we incorporated two kinds of allocation strategies. First, we used constant allocation parameters measured on site (Table 2.3) regardless of spatial patterns of prescribed rooting depth. Second, we simply assume the linear relationship between local rooting depth and constant belowground allocation ratios, which means that more fixed carbon is allocated to belowground with increasing prescribed local rooting depth. This alternative allocation strategy is justified by the fact that deeper roots require more belowground biomass. Under this alternative allocation strategy, if aboveground biomass remains the same, total belowground biomass is simply proportional to the

rooting depth while it does not change under the constant allocation strategy. Following Arora and Boer (2003), this simple linear relationship between total belowground biomass and rooting depth assumes that roots grow mainly vertically downward while maintaining surface root density.

2.5 Results

2.5.1 Topographic controls on rooting depth

Figure 2.8 shows the difference of rooting depths and root distributions between ridge and hollow locations. Our data suggests that there is no significant difference in rooting depth between them, whether they are defined as 95% cumulative distribution of root counts (RD_{95} ; Table 2.1) or maximum sampled roots depth (Figure 2.8). The average RD_{95} is 0.88 m in ridges ($n = 8$) and 0.91 m in hollows ($n = 6$). If we exclude coniferous (*Tsuga Canadensis*; hemlock) and evergreen (*Rhododendron maximum*; rhododendron) species and just compare deciduous forests, they are nearly equivalent (about 0.9 m). We note that maximum rooting depth is more error prone as roots are sampled in a two-dimension face along a single pit which may miss individual deep roots such as tap roots.

The average diameter at breast height (DBH) for deciduous broadleaf species is 41.3 cm in hollows ($n = 6$) and 29.5 cm in ridges ($n = 5$) (Table 2.1), although this difference is dominated by a single large DBH stem (*Q. rubra*). Bolstad *et al.* (2001) also found general increases of aboveground biomass and leaf area from ridge to hollow from sixteen circular 0.1 ha plots with mixed deciduous hardwood stands in the Coweeta basin. Martin *et al.* (1998) found that DBH values from ten deciduous broadleaf species in the Coweeta basin have a linear allometric relationship with leaf area, estimated from leaf mass and specific leaf area (SLA) ($R^2 = 0.822$, $n = 87$). Therefore, although there is about 40% increase of LAI from ridge to hollow in this sample, maximum rooting depths remain almost constant.

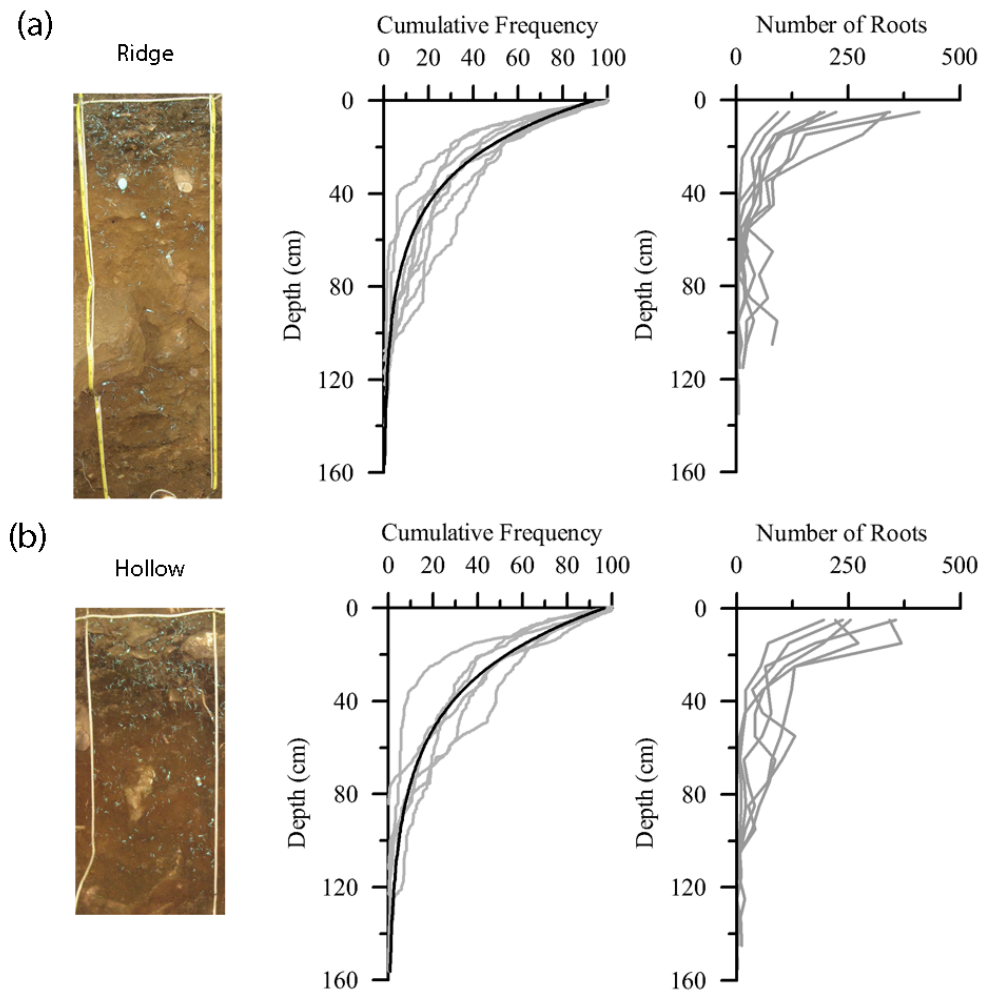


Figure 2.8: The distribution of roots as a function of soil depth for pits located on (a) ridges and (b) hollows. Distributions are expressed as root cumulative frequency and as absolute number. Grey lines represent individual pits, while black lines are the mean of all pits. Photographs are vertical sections of two *Q. rubra* pits (Table 2.1) dug within 20 m of each other. Note the difference in the depth of the dark A horizon between the two sites. Blue painted roots were used for analysis of root distributions. Modified from Figure 3 in Hales *et al.* (2009).

2.5.2 *Parameter spaces*

Figure 2.9 indicates parameter spaces for RD_{avg} and RD_{dev} in regard to MAE (mean absolute error) values between simulated and estimated LAI from hydrologic gradients of vegetation (Figure 2.4b) for all patches ($n = 1253$). These parameter spaces are not much different if we use actual estimated LAI values from the IKONOS image directly, but much higher MAE values (> 2.0) are expected even around the best-fit parameter space.

Best-fit parameter spaces are very similar for both allocation strategies, where RD_{avg} is right above 0.8 m and RD_{dev} is around zero or very slightly positive values (Figure 2.9). Too shallow RD_{avg} or high RD_{dev} can result in steeper gradients of vegetation density along the hillslope than estimated ones, where local vegetation density is too dependent on hillslope positions. Instead, simulated spatial gradients of vegetation density can disappear at high RD_{avg} or low RD_{dev} ranges, where local vegetation density is a weaker function of hillslope positions. The patterns of MAE within parameter spaces are very different between two allocation strategies. As for constant allocation strategy, MAE increases very rapidly at shallow RD_{avg} ranges (Figure 2.9a), while it increases rapidly in the deeper RD_{avg} regions in alternative allocation strategy (Figure 2.9b).

This range of estimated RD_{avg} is quite comparable to the actual maximum rooting depth measurements in the hardwood forest at the same northwest-facing slopes around the study area (McGinty 1976). Roots measured at our pits are located in southeast-facing slopes, so slightly higher maximum rooting depth values are reported. Nevertheless, we found very similar spatial pattern of rooting depth from pits excavation data (Table 2.1; Figure 2.8), not so much different between topographic positions (ridges and hollows).

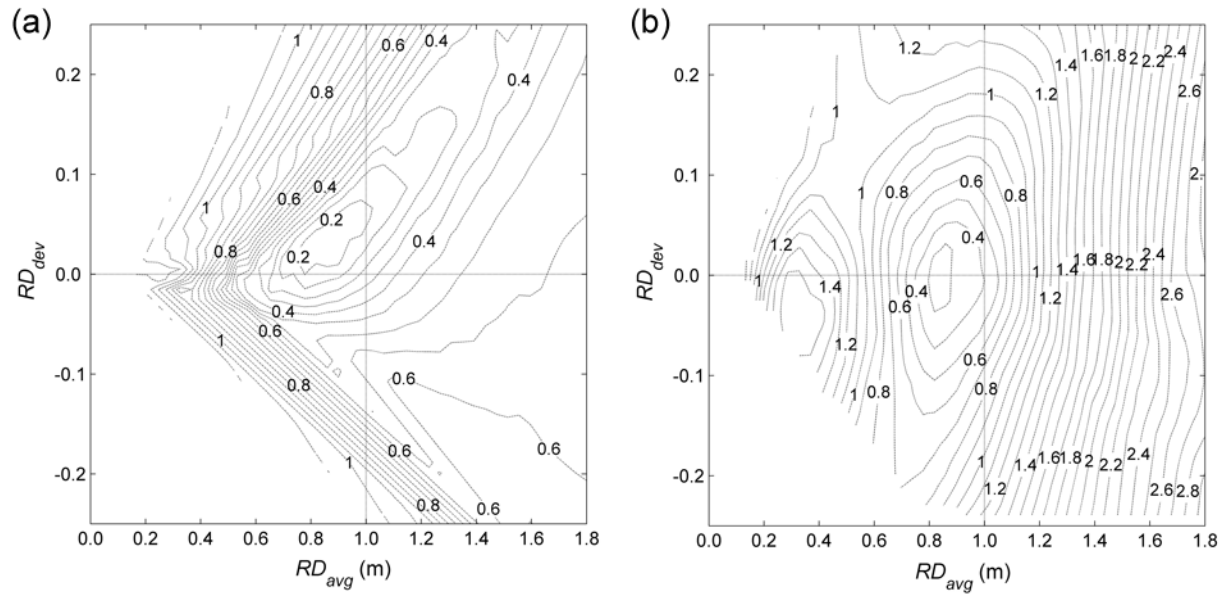


Figure 2.9: Mean absolute error (MAE) of simulated LAI within WS18 over multiple realizations of average rooting depth (RD_{avg}) and spatial pattern of rooting depth (RD_{dev}) under (a) the constant and (b) the alternative allocation strategies.

2.5.3 Long-term ecohydrologic optimality at the hillslope scales

Figure 2.10 and Figure 2.11 show the simulated long-term mean annual NPP (net primary productivity) and ET (evapotranspiration) at the study watershed during the 65-year simulation period (1941 ~ 2005) with different rooting and allocation strategies. Annual ET is calculated on a water year basis to compare with estimated ET from mass balance calculations (precipitation – runoff) at the catchment scale. Water use efficiency (WUE) values are calculated with total ET on an annual basis rather than transpiration to better represent the site-level WUE (Huxman *et al.* 2004). Figure 2.12 shows how aboveground NPP (ANPP) changes with total NPP values under different allocation strategies, where ANPP to NPP ratios reflect model allocation ratios in the model. In the alternative allocation strategy, ANPP/NPP ratios start around one at a very shallow rooting depth and decline with increasing RD_{avg} (Figure 2.12b), but are invariant in the constant allocation strategy (Figure 2.12a). Simulated ANPP is useful not only to compare with the estimated ANPP values at the study site, but also to represent allocation to aboveground vegetation density (foliar biomass) in the long-term simulations. LAI is not prescribed in the model, but a constant portion of cumulative ANPP is allocated into foliar biomass.

For both allocation strategies, optimal carbon uptake occurs around the RD_{avg} with the best fit to the spatial gradients of vegetation density (based on measured and simulated LAI) within the watershed (Figure 2.9). Optimal carbon uptake ranges are simulated with RD_{dev} values slightly negative and very close to zero, similar to the RD_{dev} estimates. Maximum WUE values are also established around these parameter ranges for both allocation strategies.

The simulated ANPP ranges at optimal parameter spaces (Figure 2.12) are similar to estimated long-term ANPP both at the whole catchment scale ($419.5 \text{ g C m}^{-2} \text{ y}^{-1}$) (Day and Monk 1974, 1977; Day *et al.* 1988) and at the plot scale (Bolstad *et al.* 2001). Also, note that there is significant discrepancy between optimal NPP and ANPP parameter ranges in the alternative allocation simulations (Figure 2.12b).

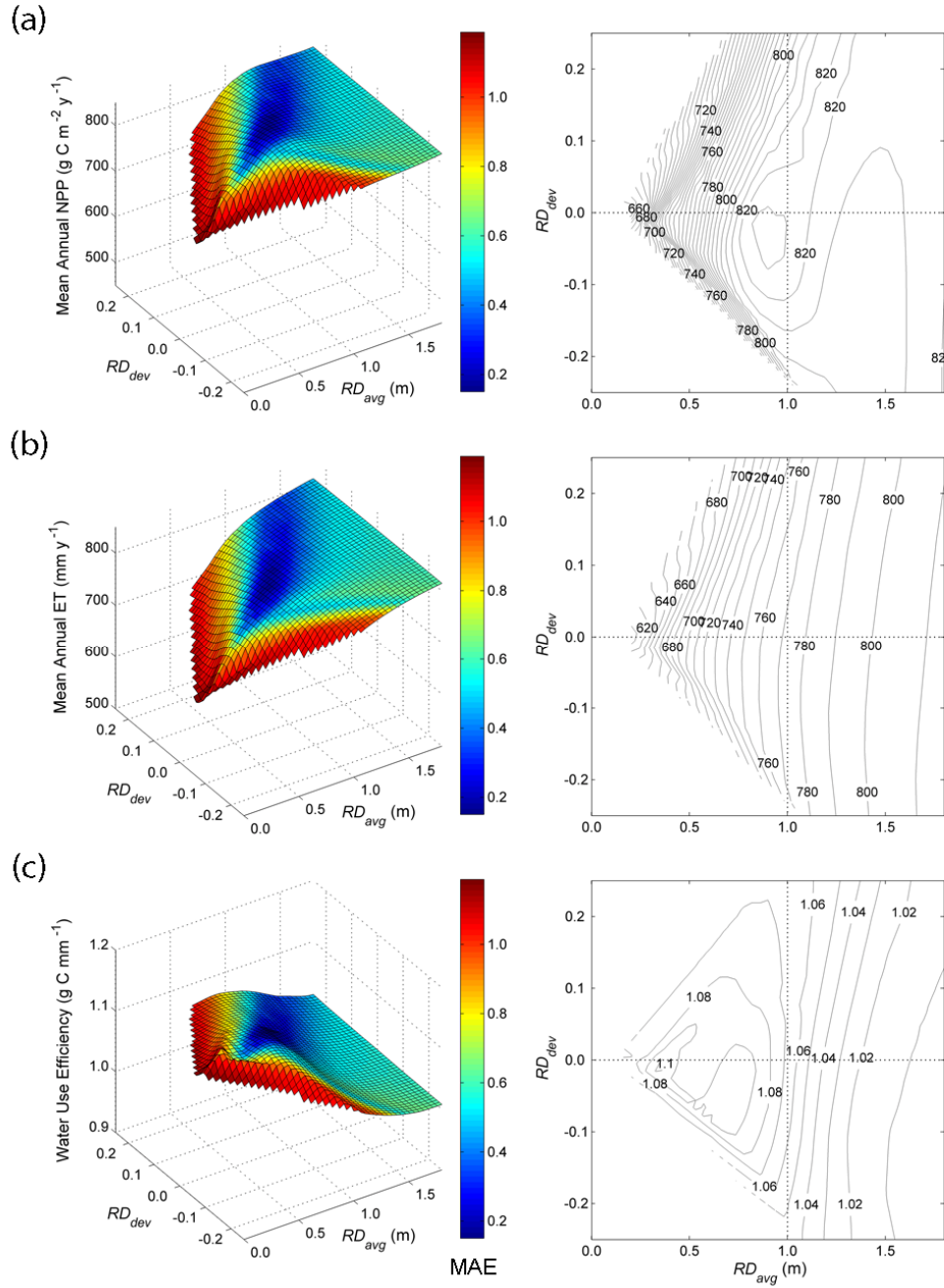


Figure 2.10: 3-D and 2-D contour plots of long-term simulated (1941 ~ 2005) average annual (a) NPP (net primary productivity), (b) ET (evapotranspiration), and (c) WUE (water used efficiency) over sampled RD_{avg} and RD_{dev} under constant allocation strategy. The color bar represents the mean absolute error (MAE) of simulated LAI (Figure 2.9a).

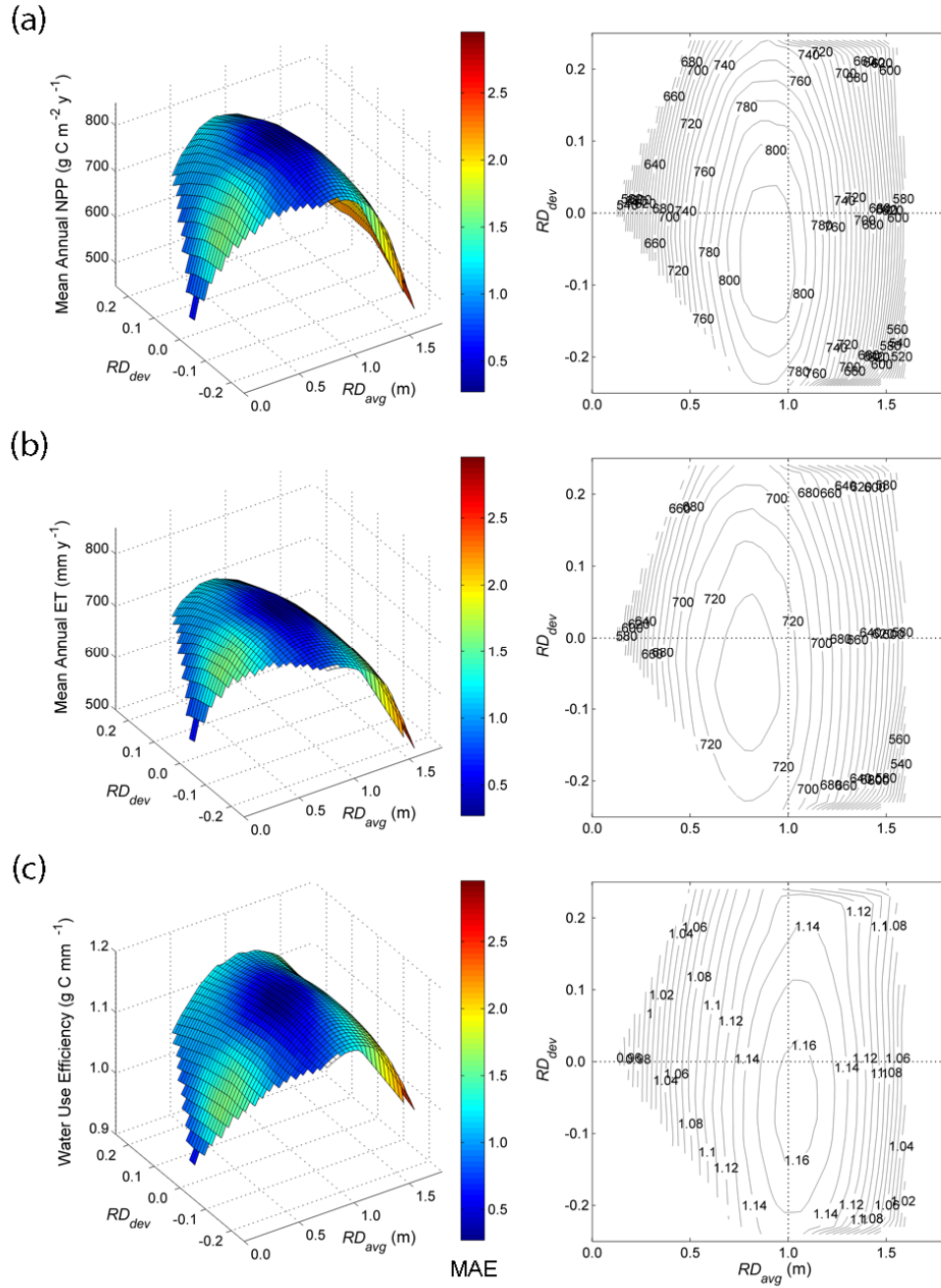


Figure 2.11: 3-D and 2-D contour plots of long-term simulated (1941 ~ 2005) average annual (a) NPP (net primary productivity), (b) ET (evapotranspiration), and (c) WUE (water used efficiency) over sampled RD_{avg} and RD_{dev} under alternative allocation strategy, where allocation ratios are as a function of local rooting depth. The color bar represents the mean absolute error (MAE) of simulated LAI (Figure 2.9b).

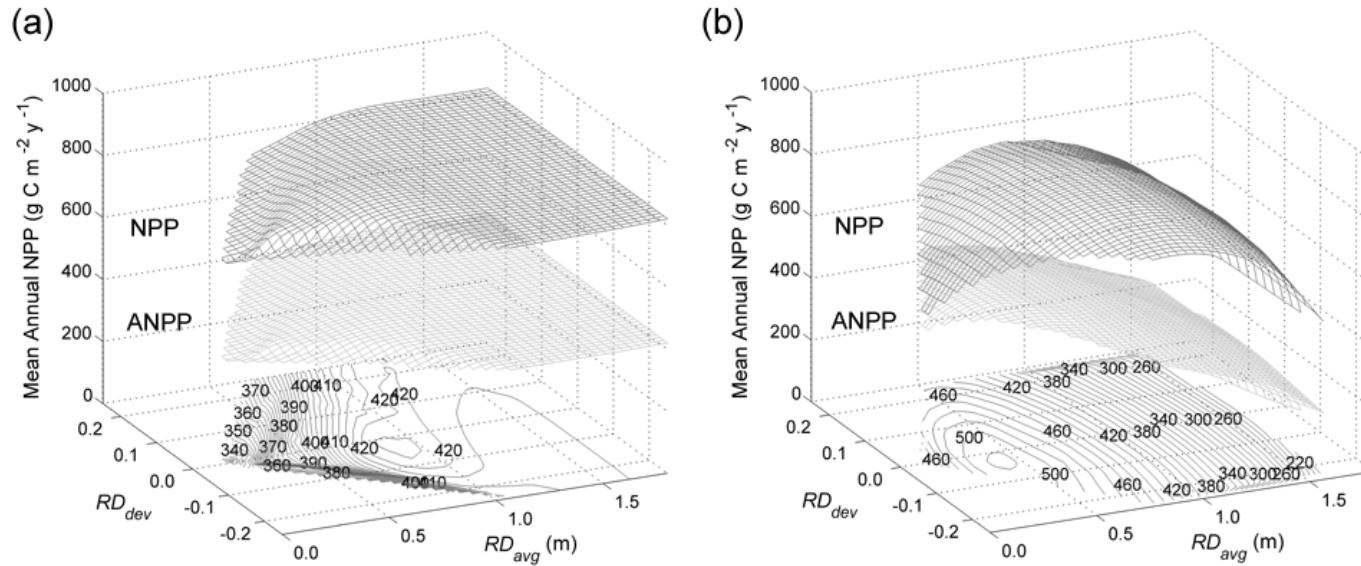


Figure 2.12: 3-D plots for long-term annual NPP (net primary productivity) and ANPP (aboveground NPP) under (a) constant and (b) alternative allocation strategies with varying RD_{avg} and RD_{dev} parameters. Contours at the x-y plane represent ANPP values. Note that allocation ratios of ANPP to NPP are constant under constant allocation strategy, while they decrease in proportion to rooting depth under alternative allocation strategy. Long term patterns of vegetation density (LAI) follow ANPP as a constant portion of cumulative ANPP is allocated into foliar biomass.

Optimal ET ranges (Figure 2.10b and Figure 2.11b) are a little lower than the catchment-scale estimated ET during the same period (794 mm y^{-1}). However, recent studies suggest that upscaled ET estimates from plot measurements in steep mountain catchments are lower than ET from mass balance, usually attributed to deep ground water bypass (e.g. Wilson *et al.* 2001). Ford *et al.* (2007) also shows that two-year ET estimates upscaled from detailed sap flux measurements are about 10% lower than catchment-based estimated ET at the adjacent pair watershed (WS17; Figure 2.3c).

2.6 Discussion and conclusions

2.6.1 Optimal vegetation gradients for system-wide productivity

This study suggests that the existing hydrologic gradients of vegetation density measured within the watershed effectively represent the long-term optimal state for system-wide carbon uptake. Model parameters controlling lateral hydrologic connectivity of the watershed are first calibrated from long-term streamflow data, which also produces reasonable spatio-temporal dynamics of surface soil moisture. To investigate the optimality of vegetation gradients, multiple spatial patterns of vegetation within the watershed are simulated by varying rooting depth as a function of hillslope position. Optimal ranges of rooting depth parameters are also supported by field measurements from pits excavation. Two different allocation strategies in the simulations elaborate the importance of canopy carbon allocation to the emergent optimality as a function of vegetation canopy patterns.

Less vegetation upslope produces a subsidy of more water to downslope vegetation, where more water and nitrogen are available. Model results suggest that more efficient photosynthesis can take place downslope for two reasons. First, increased nitrogen availability can increase carbon uptake per unit water loss (water use efficiency) in downslope vegetation. Second, ample soil moisture downslope allows plants to allocate proportionately less carbon into belowground biomass and

more into aboveground, which increases leaf area, light absorption, and total carbon uptake. However, steeper vegetation gradients (sparser canopy upslope, denser downslope) than the existing canopy pattern simulated by decreasing RD_{avg} or increasing RD_{dev} (Figure 2.9), provide a water subsidy from upslope that exceeds the capacity of the downslope canopy to transpire following an asymptotic response of ET to available water. This results in less total ET and greater catchment runoff ratios (Figure 2.10b and Figure 2.11b).

Uniform or inverse vegetation gradients are established by increasing RD_{avg} or decreasing RD_{dev} (Figure 2.9), with system-wide declines of carbon uptake for two different allocation strategies. With the constant allocation strategy, greater upslope water uptake provides less water subsidy downslope, resulting in increased total catchment ET. However, catchment productivity does not follow increasing plant water uptake because of lower nitrogen availability, specifically in upslope regions (Figure 2.7). Less nitrogen availability can result from decreases both in nitrogen transformation rates and limited amount of nitrogen upslope in the model. Second, with the alternative allocation strategy (greater proportional belowground allocation of photosynthate with increasing rooting depth), total ET and NPP decline with limited light availability (lower canopy light absorption).

In summary, the current vegetation density gradients can result from self-organization for optimal carbon uptake between adjacent patches along flowpaths. They may effectively represent the degree of dependency of multiple interacting resources (water and nutrients), moderated by feedbacks with canopy light absorption. Therefore, vegetation pattern along hydrologic flowpaths is a function of lateral hydrologic connectivity within the hillslope.

2.6.2 *Compromises between multiple resources*

Competition for light, water, and nutrients are the most important factors determining allocation of fixed carbon into vegetation compartments, providing the ecophysiological basis for compromising

between multiple stresses for optimal carbon uptake (Tilman 1988; Gedroc *et al.* 1996; McConnaughay and Coleman 1999). Simulated optimal carbon uptake ranges in this study show effective compromises between multiple stresses (water, light, and nutrients) for optimal carbon uptake. For both of the allocation strategies, there are water-limited productivity conditions up to optimal RD_{avg} ranges, whereas different stress terms act as a limiting factor for carbon uptake above optimal RD_{avg} ranges.

With the constant allocation strategy, catchment scale NPP is fairly steady above optimal RD_{avg} ranges even though annual mean ET increases (Figure 2.10). This increase of ET is mainly attributed to transpiration with increasing local rooting depth, not evaporation (interception), as LAI (following ANPP) remains almost constant (Figure 2.12a). This is mainly explained by decreasing nitrogen availability with increasing RD_{avg} especially in upslope regions (Figure 2.7). More localized soil water uptake with increasing local rooting depths requires more nitrogen especially upslope, which however is not available. In the model, nitrogen is assumed to be confined within specified rooting depth. Therefore, increased root depth produces more water availability but not nitrogen. Rather, wetter root zone moisture dynamics reduce N transformation rates as upper 60-cm soil moisture ranges within the study site are already very close to the levels maximizing decomposition, mineralization, and nitrification rates in soils highest (around 60% saturation for sandy loam soils) (Figure 2.1 and Figure 2.6), except for short dry seasons. The decline of nitrogen availability results in consistent decreases of WUE above optimal RD_{avg} ranges (Figure 2.10c). In contrast, for the alternative allocation strategy carbon uptake and annual ET decline quickly above the optimal RD_{avg} ranges (Figure 2.11). Deeper rooting depth increases water availability, while increased proportional belowground carbon allocation limits foliar biomass which decreases light absorption (Figure 2.12b).

Significant discrepancy between optimal NPP and ANPP parameter ranges in the alternative allocation simulations (Figure 2.12b) shows an example of effective compromise between light and

water resources for optimal system-wide carbon uptake (NPP). Allocation of limited photosynthate into vegetation compartments (e.g. foliar, root), is related to trade-off between resources (e.g. light, water), for a plant would be increasing one resource availability by decreasing the other (Tilman 1988). For example, even though there is higher aboveground vegetation density (or higher light availability) by more aboveground allocation at shallower RD_{avg} ranges (around 0.4 m), catchment scale optimal carbon uptake is limited by water stress, driven by lower belowground allocation. This suggests that the ‘growth-stress trade-off’ concept should be regarded as a compromise between two main complementary resources (light and water) for optimal carbon uptake itself through the control of aboveground vegetation density by limited photosynthate allocation (Tilman 1988; Gedroc *et al.* 1996; McConnaughay and Coleman 1999).

Simulation results also show that the relation between ET (even transpiration) and photosynthesis is not constant. Most optimality models are based on a steady state assumption without the dynamics of vegetation density or nitrogen availability as a function of changing rooting strategy (Rodriguez-Iturbe *et al.* 1999a; Porporato *et al.* 2001; Collins and Bras 2007; Guswa 2008). However, only transpiration (not ET) is directly related to carbon uptake via stomatal responses (Schymanski *et al.* 2007), a proportion which is actively changing with vegetation cover and resulting transpiration and interception proportions, especially in water-limited ecosystems. This effect cannot be properly simulated with a threshold approach for interception loss without simulating actual vegetation dynamics. The linear ET-photosynthesis assumption is only true when there is not so much change in vegetation density and nitrogen availability which can control the portion of transpiration and the relationship between transpiration and photosynthesis (see equations (2) and (3); Schymanski *et al.* 2008). We can see this example in the constant allocation simulations (Figure 2.10) where annual carbon uptake remains almost constant in spite of increases annual ET, because nitrogen availability decreases.

2.6.3 *An objective function of optimality models*

Rodriguez-Iturbe and co-workers used the ‘water stress’ term as an objective function for optimal vegetation density where water stress was quantitatively expressed as a non-linear function of soil moisture (Rodriguez-Iturbe *et al.* 1999a; Porporato *et al.* 2001). They postulated that optimal vegetation condition can be found between minimum water stress and maximum productivity assuming that productivity is directly proportional to evapotranspiration under water-limited ecosystems (Porporato *et al.* 2001).

Vegetation density, quantified as leaf area index (LAI), is not only an indicator for energy absorption of photosynthetically active radiation (PAR), but also a main channel for water loss through transpiration and interception storage. Vegetation actively compromises between light and water resources at short (e.g. leaf orientation) and long-term scale to achieve optimal carbon uptake given climate and soil conditions by density adjustment with water-stress driven foliage reduction in water-limited condition or more allocation into leaf in an energy-limited condition.

If vegetation density is above the optimal state given climate and soil conditions, large interception storage effectively decouples water loss from carbon uptake which eventually results in severe water stress and productivity decline. Many studies report decreasing water use efficiency and decoupling between water loss and carbon uptake during severe drought conditions (e.g. Hwang *et al.* 2008; Baldocchi 1997; Reichstein *et al.* 2002; Leuning *et al.* 2005). On the other hand, if vegetation density (or cover) is below the optimal state given climate and soil conditions, energy absorbed by vegetation can be a limiting factor for photosynthesis which will result in increased allocation to foliar carbon increasing light absorption toward an optimal vegetation state.

In this context, the current canopy density pattern in WS18 appears to be close to an optimal state for carbon uptake itself, not a compromise between minimum water stress and maximum productivity. Vegetation fully exploits the most limiting factor as possible for their maximum growth across diverse ecosystems, often called ‘Liebig's Law of the minimum’ (Tilman 1988).

Even in water-limited ecosystems, the current vegetation state should be the maximization point of vegetation productivity because they are opening their stomata as much as possible for efficient uptake of CO₂ at the least cost of water to avoid severe water stress. Vegetations in water-limited ecosystems always fully use available water in soil (Kerkhoff *et al.* 2004) while avoiding severe water stress to maximize their productivity, not to minimize water stress itself. Moreover, a water stress term cannot be a general objective function for optimality models as limiting factors for carbon assimilation should be different across various ecosystems.

Recently, Schymanski *et al.* (2007, 2009) asserted that carbon uptake (e.g. net carbon profit) should be an objective function of optimality models regarding transpiration as the ‘inevitable’ cost or leak for carbon assimilation process. While this assertion is consistent with the approach taken here and in a number of previous studies, the appropriateness of net carbon profit (NCP) as a driving force in optimality models is somewhat controversial (Raupach 2005). Schymanski *et al.* (2007, 2009) tried to estimate seasonal optimal state of vegetation from measured water fluxes throughout a monthly and a daily basis. This approach has some problems in that current vegetation structure or cover is not just a result of short-term optimization for carbon uptake, but also a result of cumulative and transient effect of previous photosynthesis, respiration and allocation. Many researchers reported an inter-annual transient effect of climate factor on vegetation dynamics from flux measurements (Law *et al.* 2002; Barr *et al.* 2004), satellite observations (Goward and Prince 1995; Mohamed *et al.* 2004), and tree ring growth measurements (Gonzalez-Elizondo *et al.* 2005; Andreassen *et al.* 2006; Pumijumnong and Wanyaphet 2006; Tardif and Conciatori 2006). Vegetation structure in forest ecosystems does not adjust promptly to changing environmental conditions (e.g. water stress) unlike grass-based ecosystem.

2.6.4 Allocation dynamics along the hillslope gradients

It is widely accepted that proportional belowground allocation usually increases with decreasing water and nutrient availability (Gedroc *et al.* 1996; McConnaughay and Coleman 1999; Cromer and Jarvis 1990; Ryan *et al.* 2004; Litton *et al.* 2007; Friedlingstein *et al.* 1999). In WS18, surface soil moisture dynamics (Figure 2.6) indicate that wetter regions are more favorable to available nitrogen along with associated nutrient transport through shallow subsurface flow. Moreover, soil moisture has a primary control on vegetation density (Figure 2.4b), which suggests that the amount of nitrogen input through litter inputs also follows hillslope gradients. For these reasons, there are significant increases of nitrogen availability with wetness within the study site (Knoepp and Swank 1998; Knoepp *et al.* 2008), which also suggests a more rapid cycling of organic matter and greater amount of nutrients available to plants. Therefore, the belowground allocation proportion may decrease with hillslope moisture gradients (without a species shift) simply because water and nutrient availability increases.

This spatial allocation pattern is very similar to what we found in pits excavation experiments (Figure 2.8) and the alternative allocation strategy simulations (Figure 2.11) with spatially homogeneous vegetation species. There was significant increase of DBH from ridge to hollow in our sample, maximum rooting depths are almost constant (Table 2.1). Even though we did not actually calculate total belowground biomass for the lack of lateral roots spread information, this shows possible transitions in allocation dynamics along the hillslope gradients. In the simulation, the optimal RD_{dev} parameter for optimal carbon uptake is located at slightly negative ranges, so maximum rooting depth and belowground allocation proportion slightly decreases downslope. However, transitions into more tolerant vegetation species in a dry region may offset this optimal allocation dynamics along the hillslope gradient. As far as we know, there are no empirical studies on the allocation dynamics along hillslope gradients, that account for the effects of downslope changes of water, nutrients, light availability (McConnaughay and Coleman 1999, and references therein), species shifts (McConnaughay and Coleman 1999; Gower *et al.* 2001), and stand ages

(often called ‘ontogenic drift’) (McConnaughay and Coleman 1999; Ryan *et al.* 2004; Litton *et al.* 2007). For this reason, it would be difficult to find consistent allocation patterns along hillslope gradients in natural situations.

2.6.5 *Limitations of this study*

In this study, we used a simple representation of rooting depth given the complexity of spatial variation and transport processes, assuming density to be evenly distributed with depth. However, a vertical distribution of roots is important for determining water and nutrient availability (Jackson *et al.* 2000; Collins and Bras 2007). Shallow roots play an important role in nutrient recycling as most nutrients (especially nitrogen) are concentrated in the surface soil layer (Jobbagy and Jackson 2001), while deep roots mostly determine water availability during a dry season. For this reason, vertical distribution of roots can play an important role in compromising between these two resources (water and nutrients). Pit observations in our site show fine roots are more evenly distributed with depth in hollow soils, while fine roots often show bimodal distributions at shallow soil depth and the soil-saprolite boundary (Hales *et al.* 2009). A feedback between greater carbon allocation to deeper roots and the density of shallow fine roots may be useful to explore in future modeling efforts. However, this would require significantly more information on soil profile form and computational effort, especially if multiple model realizations are required.

Second, we did not integrate detailed spatial patterns of vegetation species and soil in the study area. Vegetation species varies from xeric to mesic species following hillslope position in this study site (Day and Monk 1974; Day *et al.* 1988). Xeric species are more tolerant to water stress, so optimal carbon uptake may occur at shallower rooting depth than simulated by the model in upslope regions. Mesic species need more water, so optimal carbon uptake may occur at deeper rooting depth than simulated in downslope regions. Hence optimal rooting depth patterns (RD_{dev}) may show a small positive trend downslope given the spatial pattern of species transition. We note that in both

simulated and observed rooting depth, trends are close to zero, contrary to our initial expectations. However, this trend is consistent with the trend of the absolute amount of photosynthate production and the proportional aboveground/belowground allocation.

In the study catchment, soil texture varies from fine sandy loam to silt loam (from soil texture data provided by Todd Lookingbill) with increasing wetness along the hillslope gradients, while soil tends from thinner to thicker (Hales *et al.* 2009). However, our soil pit observations did not indicate any strong textural gradients, but did reveal large local heterogeneity in colluvial soils. Transition of soil texture along the hillslope gradients may favor soil water holding capacity in wetter regions per unit soil depth (Brady and Weil 2002; Schenk and Jackson 2002; Dingman 2002). However, Hales *et al.* (2009) also found high fine root density profiles in the soil-saprolite boundaries in dry region. This suggests that soil-saprolite boundary acts as a physical barrier for deep roots in the dry region, in which case optimal rooting depth patterns may not be properly established along the hillslope gradients.

2.6.6 *Conclusions*

This study suggests that the existing hydrologic gradients of vegetation within the catchment effectively represent the long-term optimal state for carbon uptake, which is closely modulated by rooting and allocation strategies. Traditionally, optimality approaches have assumed a steady state mechanism within the model, based on water or carbon principles. We have used a different approach emphasizing a fully transient, distributed model to investigate whether optimal ecosystem properties emerge as a result of self organizing spatial patterns of canopy density, specifically in the form of catchment scale ecosystem productivity and water use efficiency. The existing vegetation pattern must be understood as a feedback between multiple stresses (e.g. light, water, and nutrients) as connected by water flow along topographic gradients. This adjustment and evolution of the ecosystem with the geomorphic, climatic and hydrologic settings results in an emergent pattern that

optimizes system-wide carbon uptake, over and above the individual patch. This study extends and tests the concept of eco-physiological optimality theory at short-term and plot scales to long-term ecohydrological optimality at catchment and hillslope scales.

Acknowledgements

The research represented in this paper was supported by a USDA Forest Service cooperative agreement (SRS-06-CA 11330410-0) and the National Science Foundation award to the Coweeta Long Term Ecologic Research project (DEB #0823293). Data was made available from the Coweeta Hydrological Laboratory and LTER, which is supported by the National Science Foundation and the USDA Forest Service. We specifically thank Dr. Jim Vose and Dr. Paul Bolstad for their support in providing data in the Coweeta Hydrologic Lab. We also thank Dr. Todd Lookingbill who provided the valuable soil information. This paper is co-authored by Dr Lawrence E. Band and Dr. T. C. Hales. Soil excavation measurements were mainly conducted by Dr. T.C. Hales. Dr. L. E. Band provided a basic research question and gave overall directions to this research study as a dissertation advisor.

References

- Andreassen K, Solberg S, Tveito OE, Lystad SL (2006) Regional differences in climatic responses of Norway spruce (*Picea abies* L. Karst) growth in Norway. *Forest Ecology and Management*, **222**, 211-221.
- Arora VK, Boer GJ (2003) A Representation of Variable Root Distribution in Dynamic Vegetation Models. *Earth Interactions*, **7**, 1-19.
- Arris LL, Eagleson PS (1994) A water-use model for locating the boreal deciduous forest ecotone in eastern North America. *Water Resources Research*, **30**, 1-9.
- Baldocchi D (1997) Measuring and modelling carbon dioxide and water vapour exchange over a temperate broad-leaved forest during the 1995 summer drought. *Plant Cell and Environment*, **20**, 1108-1122.
- Baldocchi DD, Luxmoore RJ, Hatfield JL (1991) Discerning the Forest from the Trees - an Essay on Scaling Canopy Stomatal Conductance. *Agricultural and Forest Meteorology*, **54**, 197-226.
- Band LE, Patterson P, Nemani R, Running SW (1993) Forest ecosystem processes at the watershed scale: incorporating hillslope hydrology. *Agricultural and Forest Meteorology*, **63**, 93-126.
- Band LE, Tague CL, Groffman P, Belt K (2001) Forest ecosystem processes at the watershed scale: hydrological and ecological controls of nitrogen export. *Hydrological Processes*, **15**, 2013-2028.
- Barr AG, Black TA, Hogg EH, Kljun N, Morgenstern K, Nesic Z (2004) Inter-annual variability in the leaf area index of a boreal aspen-hazelnut forest in relation to net ecosystem production. *Agricultural and Forest Meteorology*, **126**, 237-255.
- Beven K, Kirkby M (1979) A physically-based variable contributing area model of basin hydrology. *Hydrologic Science Bulletin*, **24**, 43-69.
- Bolstad PV, Mitchell K, Vose JM (1999) Foliar temperature-respiration response functions for broad-leaved tree species in the southern Appalachians. *Tree physiology*, **19**, 871-878.
- Bolstad PV, Vose JM (2005) Forest and pasture carbon pools and soil respiration in the southern Appalachian Mountains. *Forest Science*, **51**, 372-383.
- Bolstad PV, Vose JM, McNulty SG (2001) Forest productivity, leaf area, and terrain in southern Appalachian deciduous forests. *Forest Science*, **47**, 419-427.
- Brady NC, Weil RR (2002) *The Nature and Properties of Soils*. Prentice Hall, Upper Saddle River, NJ, USA.

- Bromley J, Brouwer J, Barker AP, Gaze SR, Valentin C (1997) The role of surface water redistribution in an area of patterned vegetation in a semi-arid environment, south-west Niger. *Journal of Hydrology*, **198**, 1-29.
- Camporeale C, Ridolfi L (2006) Riparian vegetation distribution induced by river flow variability: A stochastic approach. *Water Resources Research*, **42**, W10415.
- Canadell J, Jackson RB, Ehleringer JR, Mooney HA, Sala OE, Schulze ED (1996) Maximum rooting depth of vegetation types at the global scale. *Oecologia*, **108**, 583-595.
- Caylor KK, Manfreda S, Rodriguez-Iturbe I (2005) On the coupled geomorphological and ecohydrological organization of river basins. *Advances in Water Resources*, **28**, 69-86.
- Caylor KK, Scanlon TM, Rodriguez-Iturbe I (2004) Feasible optimality of vegetation patterns in river basins. *Geophysical Research Letters*, **31**, L13502.
- Chen JM, Chen XY, Ju WM, Geng XY (2005) Distributed hydrological model for mapping evapotranspiration using remote sensing inputs. *Journal of Hydrology*, **305**, 15-39.
- Chen JM, Cihlar J (1996) Retrieving leaf area index of boreal conifer forests using landsat TM images. *Remote Sensing of Environment*, **55**, 153-162.
- Chen JM, Liu J, Cihlar J, Goulden ML (1999) Daily canopy photosynthesis model through temporal and spatial scaling for remote sensing applications. *Ecological Modelling*, **124**, 99-119.
- Clinton BD, Yeakley JA, Apsley DK (2003) Tree growth and mortality in a southern appalachian deciduous forest following extended wet and dry periods. *Castanea*, **68**, 189-200.
- Collatz GJ, Ball JT, Grivet C, Berry JA (1991) Physiological and Environmental-Regulation of Stomatal Conductance, Photosynthesis and Transpiration - a Model that Includes a Laminar Boundary-Layer. *Agricultural and Forest Meteorology*, **54**, 107-136.
- Collins DBG, Bras RL (2007) Plant rooting strategies in water-limited ecosystems. *Water Resources Research*, **43**, W06407.
- Cowan IR (1982) Regulation of Water Use in Relation to Carbon Gain in Higher Plants. In: *Physical Plant Ecology II* (eds Lange OL, Nobel PS, Osmond CB, Ziegler H), pp. 589-613. Springer, Berlin, Germany.
- Cowan IR, Farquhar GD (1977) Stomatal Function in Relation to Leaf Metabolism and Environment. In: *Integration of activity in the higher plant* (ed Jennings DH), pp. 471-505. Cambridge University Press, Cambridge, UK.
- Creed IF, Band LE (1998a) Exploring functional similarity in the export of nitrate-N from forested catchments: A mechanistic modeling approach. *Water Resources Research*, **34**, 3079-3093.

- Creed IF, Band LE (1998b) Export of nitrogen from catchments within a temperate forest: Evidence for a unifying mechanism regulated by variable source area dynamics. *Water Resources Research*, **34**, 3105-3120.
- Cromer RN, Jarvis PG (1990) Growth and Biomass Partitioning in Eucalyptus-Grandis Seedlings in Response to Nitrogen Supply. *Australian Journal of Plant Physiology*, **17**, 503-515.
- Day FP, Philips DL, Monk CD (1988) Forest communities and patterns. In: *Forest Hydrology and Ecology at Coweeta* (eds Swank WT, Crossley JDA), pp. 141-149. Springer-Verlag, New York, NY, USA.
- Day FP, Monk CD (1977) Net Primary Production and Phenology on a Southern Appalachian Watershed. *American Journal of Botany*, **64**, 1117-1125.
- Day FP, Monk CD (1974) Vegetation Patterns on a Southern Appalachian Watershed. *Ecology*, **55**, 1064-1074.
- de Pury DGG, Farquhar GD (1997) Simple scaling of photosynthesis from leaves to canopies without the errors of big-leaf models. *Plant Cell and Environment*, **20**, 537-557.
- Dingman SL (2002) *Physical Hydrology*. Prentiss Hall, Upper Saddle River, NJ, USA.
- Eagleson PS (2002) *Ecohydrology*. Cambridge University Press, New York, NY, USA.
- Eagleson PS (1982) Ecological Optimality in Water-Limited Natural Soil-Vegetation Systems .1. Theory and Hypothesis. *Water Resources Research*, **18**, 325-340.
- Eagleson PS (1978a) Climate, Soil, and Vegetation .1. Introduction to Water-Balance Dynamics. *Water Resources Research*, **14**, 705-712.
- Eagleson PS (1978b) Climate, Soil, and Vegetation .2. Distribution of Annual Precipitation Derived from Observed Storm Sequences. *Water Resources Research*, **14**, 713-721.
- Eagleson PS (1978c) Climate, Soil, and Vegetation .3. Simplified Model of Soil-Moisture Movement in Liquid-Phase. *Water Resources Research*, **14**, 722-730.
- Eagleson PS (1978d) Climate, Soil, and Vegetation .4. Expected Value of Annual Evapotranspiration. *Water Resources Research*, **14**, 731-739.
- Eagleson PS (1978e) Climate, Soil, and Vegetation .5. Derived Distribution of Storm Surface Runoff. *Water Resources Research*, **14**, 741-748.
- Eagleson PS (1978f) Climate, Soil, and Vegetation .6. Dynamics of Annual Water-Balance. *Water Resources Research*, **14**, 749-764.
- Eagleson PS (1978g) Climate, Soil, and Vegetation .7. Derived Distribution of Annual Water Yield. *Water Resources Research*, **14**, 765-776.

- Eagleson PS, Tellers TE (1982) Ecological Optimality in Water-Limited Natural Soil-Vegetation Systems .2. Tests and Applications. *Water Resources Research*, **18**, 341-354.
- Elliott KJ, Swank WT (1994) Impacts of Drought on Tree Mortality and Growth in a Mixed Hardwood Forest. *Journal of Vegetation Science*, **5**, 229-236.
- Emanuel RE, D'Odorico P, Epstein HE (2007) Evidence of optimal water use by vegetation across a range of North American ecosystems. *Geophysical Research Letters*, **34**, L07401.
- Famiglietti JS, Wood EF (1994) Multiscale Modeling of Spatially-Variable Water and Energy-Balance Processes. *Water Resources Research*, **30**, 3061-3078.
- Farquhar GD, von Caemmerer S (1982) Modeling of photosynthetic response to environmental conditions. In: *Physical Plant Ecology II* (eds Lange OL, Nobel PS, Osmond CB, Ziegler H), pp. 550-587. Springer, Berlin, Germany.
- Farquhar GD, Caemmerer SV, Berry JA (1980) A Biochemical-Model of Photosynthetic CO₂ Assimilation in Leaves of C₃ Species. *Planta*, **149**, 78-90.
- Farquhar GD, von Caemmerer S, Berry JA (2001) Models of photosynthesis. *Plant Physiology*, **125**, 42-45.
- Fassnacht KS, Gower ST, MacKenzie MD, Nordheim EV, Lillesand TM (1997) Estimating the leaf area index of North Central Wisconsin forests using the Landsat Thematic Mapper. *Remote Sensing of Environment*, **61**, 229-245.
- Field C (1983) Allocating Leaf Nitrogen for the Maximization of Carbon Gain: Leaf Age as a Control on the Allocation Program. *Oecologia*, **56**, 341-347.
- Ford CR, Hubbard RM, Kloeppel BD, Vose JM (2007) A comparison of sap flux-based evapotranspiration estimates with catchment-scale water balance. *Agricultural and Forest Meteorology*, **145**, 176-185.
- Friedlingstein P, Joel G, Field CB, Fung IY (1999) Toward an allocation scheme for global terrestrial carbon models. *Global Change Biology*, **5**, 755-770.
- Friend AD, Stevens AK, Knox RG, Cannell MGR (1997) A process-based, terrestrial biosphere model of ecosystem dynamics (Hybrid v3.0). *Ecological Modelling*, **95**, 249-287.
- Gedroc JJ, McConnaughay KDM, Coleman JS (1996) Plasticity in root shoot partitioning: Optimal, ontogenetic, or both? *Functional Ecology*, **10**, 44-50.
- Gholz HL, Vogel SA, Cropper WP, McKelvey K, Ewel KC, Teskey RO, Curran PJ (1991) Dynamics of canopy structure and light interception in *Pinus Elliottii* stands, North Florida. *Ecological Monographs*, **61**, 33-51.

- Gonzalez-Elizondo M, Jurado E, Navar J, Gonzalez-Elizondo MS, Villanueva J, Aguirre O, Jimenez J (2005) Tree-rings and climate relationships for Douglas-fir chronologies from the Sierra Madre Occidental, Mexico: A 1681-2001 rain reconstruction. *Forest Ecology and Management*, **213**, 39-53.
- Goward SN, Prince SD (1995) Transient effects of climate on vegetation dynamics: Satellite observations. *Journal of Biogeography*, **22**, 549-564.
- Gower ST, Krankina O, Olson RJ, Apps M, Linder S, Wang C (2001) Net primary production and carbon allocation patterns of boreal forest ecosystems. *Ecological Applications*, **11**, 1395-1411.
- Gower ST, Norman JM (1991) Rapid estimation of leaf area index in conifer and broad-leaf plantations. *Ecology*, **72**, 1896-1900.
- Guswa AJ (2008) The influence of climate on root depth: A carbon cost-benefit analysis. *Water Resources Research*, **44**, W02427.
- Hales TC, Ford CR, Hwang T, Vose JM, Band LE (2009) Topographic and ecologic controls on root reinforcement. *Journal of Geophysical Research-Earth Surface*, **114**, F03013.
- Hari P, Makela A, Berninger F, Pohja T (1999) Field evidence for the optimality hypothesis of gas exchange in plants. *Australian Journal of Plant Physiology*, **26**, 239-244.
- Hari P, Makela A, Pohja T (2000) Surprising implications of the optimality hypothesis of stomatal regulation gain support in a field test. *Australian Journal of Plant Physiology*, **27**, 77-80.
- Hewlett JD (1961) *Soil moisture as a source of base flow from steep mountain watersheds*. **Station Paper 132**, Southeast Forest Experimental Station, U.S. Department of Agriculture and Forest Service, Asheville, NC, USA.
- Hewlett JD, Hibbert AR (1963) Moisture and Energy Conditions within a Sloping Soil Mass during Drainage. *Journal of Geophysical Research*, **68**, 1081-1087.
- Howes DA, Abrahams AD (2003) Modeling runoff and runoff in a desert shrubland ecosystem, Jornada Basin, New Mexico. *Geomorphology*, **53**, 45-73.
- Huete A, Justice C, Liu H (1994) Development of Vegetation and Soil Indexes for Modis-Eos. *Remote Sensing of Environment*, **49**, 224-234.
- Huete AR (1988) A Soil-Adjusted Vegetation Index (Savi). *Remote Sensing of Environment*, **25**, 295-309.
- Hui DF, Jackson RB (2006) Geographical and interannual variability in biomass partitioning in grassland ecosystems: a synthesis of field data. *New Phytologist*, **169**, 85-93.
- Huxman TE, Smith MD, Fay PA, et al (2004) Convergence across biomes to a common rain-use efficiency. *Nature*, **429**, 651-654.

- Hwang T, Kang S, Kim J, Kim Y, Lee D, Band L (2008) Evaluating drought effect on MODIS Gross Primary Production (GPP) with an eco-hydrological model in the mountainous forest, East Asia. *Global Change Biology*, **14**, 1037-1056.
- Ivanov VY, Bras RL, Vivoni ER (2008) Vegetation-hydrology dynamics in complex terrain of semiarid areas: 1. A mechanistic approach to modeling dynamic feedbacks. *Water Resources Research*, **44**, W03429.
- Jackson RB, Moore LA, Hoffmann WA, Pockman WT, Linder CR (1999) Ecosystem rooting depth determined with caves and DNA. *Proceedings of the National Academy of Sciences of the United States of America*, **96**, 11387-11392.
- Jackson RB, Schenk HJ, Jobbagy EG, et al (2000) Belowground consequences of vegetation change and their treatment in models. *Ecological Applications*, **10**, 470-483.
- Jarvis PG (1976) The Interpretation of the Variations in Leaf Water Potential and Stomatal Conductance Found in Canopies in the Field. *Philosophical Transactions of the Royal Society of London. Series B, Biological Sciences*, **273**, 593-610.
- Jobbagy EG, Jackson RB (2001) The distribution of soil nutrients with depth: Global patterns and the imprint of plants. *Biogeochemistry*, **53**, 51-77.
- Kerkhoff AJ, Martens SN, Milne BT (2004) An ecological evaluation of Eagleson's optimality hypotheses. *Functional Ecology*, **18**, 404-413.
- Kim HS, Oren R, Hinckley TM (2008) Actual and potential transpiration and carbon assimilation in an irrigated poplar plantation. *Tree physiology*, **28**, 559-577.
- Kimball JS, Thornton PE, White MA, Running SW (1997) Simulating forest productivity and surface-atmosphere carbon exchange in the BOREAS study region. *Tree physiology*, **17**, 589-599.
- Kleidon A, Heimann M (1998) A method of determining rooting depth from a terrestrial biosphere model and its impacts on the global water and carbon cycle. *Global Change Biology*, **4**, 275-286.
- Knoepp JD, Swank WT (1998) Rates of nitrogen mineralization across an elevation and vegetation gradient in the southern Appalachians. *Plant and Soil*, **204**, 235-241.
- Knoepp JD, Vose JM, Swank WT (2008) Nitrogen deposition and cycling across an elevation and vegetation gradient in southern Appalachian forests. *International Journal of Environmental Studies*, **65**, 389-408.
- Laio F, D'Odorico P, Ridolfi L (2006) An analytical model to relate the vertical root distribution to climate and soil properties. *Geophysical Research Letters*, **33**, L18401.
- Law BE, Falge E, Gu L, et al (2002) Environmental controls over carbon dioxide and water vapor exchange of terrestrial vegetation. *Agricultural and Forest Meteorology*, **113**, 97-120.

- Leuning R (1995) A critical-appraisal of a combined stomatal-photosynthesis model for C₃ plants. *Plant Cell and Environment*, **18**, 339-355.
- Leuning R, Cleugh HA, Zegelin SJ, Hughes D (2005) Carbon and water fluxes over a temperate *Eucalyptus* forest and a tropical wet/dry savanna in Australia: measurements and comparison with MODIS remote sensing estimates. *Agricultural and Forest Meteorology*, **129**, 151-173.
- Litton CM, Raich JW, Ryan MG (2007) Carbon allocation in forest ecosystems. *Global Change Biology*, **13**, 2089-2109.
- Ludwig JA, Wilcox BP, Breshears DD, Tongway DJ, Imeson AC (2005) Vegetation patches and runoff-erosion as interacting ecohydrological processes in semiarid landscapes. *Ecology*, **86**, 288-297.
- Mackay DS (2001) Evaluation of hydrologic equilibrium in a mountainous watershed: incorporating forest canopy spatial adjustment to soil biogeochemical processes. *Advances in Water Resources*, **24**, 1211-1227.
- Mackay DS, Band LE (1997) Forest ecosystem processes at the watershed scale: dynamic coupling of distributed hydrology and canopy growth. *Hydrological Processes*, **11**, 1197-1217.
- Martin JG, Kloeppel BD, Schaefer TL, Kimbler DL, McNulty SG (1998) Aboveground biomass and nitrogen allocation of ten deciduous southern Appalachian tree species. *Canadian Journal of Forest Research-Revue Canadienne De Recherche Forestiere*, **28**, 1648-1659.
- McConnaughay KDM, Coleman JS (1999) Biomass allocation in plants: Ontogeny or optimality? A test along three resource gradients. *Ecology*, **80**, 2581-2593.
- McGinty DT (1976) Comparative root and soil dynamics on a white pine watershed and in the hardwood forest in the Coweeta basin. Unpublished PhD thesis, University of Georgia, Athens, GA, USA.
- McMurtrie RE, Leuning R, Thompson WA, Wheeler AM (1992) A Model of Canopy Photosynthesis and Water-use Incorporating a Mechanistic Formulation of Leaf CO₂ Exchange. *Forest Ecology and Management*, **52**, 261-278.
- Mitchell KA, Bolstad PV, Vose JM (1999) Interspecific and environmentally induced variation in foliar dark respiration among eighteen southeastern deciduous tree species. *Tree physiology*, **19**, 861-870.
- Mohamed MAA, Babiker IS, Chen ZM, Ikeda K, Ohta K, Kato K (2004) The role of climate variability in the inter-annual variation of terrestrial net primary production (NPP). *Science of the Total Environment*, **332**, 123-137.

- Monk CD, Day FP (1988) Biomass, Primary Production, and Selected Nutrient Budgets for an Undisturbed Watershed. In: *Forest Hydrology and Ecology at Coweeta* (eds Swank WT, Crossley JDA), pp. 151-159. Springer-Verlag, New York, NY, USA.
- Nadelhoffer KJ, Emmett BA, Gundersen P, Kjonaas OJ, Koopmans CJ, Schleppi P, Tietema A, Wright RF (1999) Nitrogen deposition makes a minor contribution to carbon sequestration in temperate forests. *Nature*, **398**, 145-148.
- Nash JE, Sutcliffe JV (1970) River flow forecasting through conceptual models part I — A discussion of principles. *Journal of Hydrology*, **10**, 282-290.
- Nemani R, Pierce L, Running S, Band L (1993) Forest Ecosystem Processes at the Watershed Scale: Sensitivity to Remotely-Sensed Leaf Area Index Estimates. *International Journal of Remote Sensing*, **14**, 2519-2534.
- Nemani RR, Running SW (1989) Testing a Theoretical Climate Soil Leaf-Area Hydrologic Equilibrium of Forests using Satellite Data and Ecosystem Simulation. *Agricultural and Forest Meteorology*, **44**, 245-260.
- Nepstad DC, Decarvalho CR, Davidson EA, et al (1994) The Role of Deep Roots in the Hydrological and Carbon Cycles of Amazonian Forests and Pastures. *Nature*, **372**, 666-669.
- Oren R, Ellsworth DS, Johnsen KH, et al (2001) Soil fertility limits carbon sequestration by forest ecosystems in a CO₂-enriched atmosphere. *Nature*, **411**, 469-472.
- Oren R, Pataki DE (2001) Transpiration in response to variation in microclimate and soil moisture in southeastern deciduous forests. *Oecologia*, **127**, 549-559.
- Parton WJ, Mosier AR, Ojima DS, Valentine DW, Schimel DS, Weier K, Kulmala AE (1996) Generalized model for N₂ and N₂O production from nitrification and denitrification. *Global Biogeochemical Cycles*, **10**, 401-412.
- Pierce LL, Running SW (1988) Rapid Estimation of Coniferous Forest Leaf-Area Index using a Portable Integrating Radiometer. *Ecology*, **69**, 1762-1767.
- Porporato A, D'Odorico P, Laio F, Ridolfi L, Rodriguez-Iturbe I (2002) Ecohydrology of water-controlled ecosystems. *Advances in Water Resources*, **25**, 1335-1348.
- Porporato A, D'Odorico P, Laio F, Rodriguez-Iturbe I (2003) Hydrologic controls on soil carbon and nitrogen cycles. I. Modeling scheme. *Advances in Water Resources*, **26**, 45-58.
- Porporato A, Laio F, Ridolfi L, Rodriguez-Iturbe I (2001) Plants in water-controlled ecosystems: active role in hydrologic processes and response to water stress - III. Vegetation water stress. *Advances in Water Resources*, **24**, 725-744.

- Pumijumnong N, Wanyaphet T (2006) Seasonal cambial activity and tree-ring formation of *Pinus merkusii* and *Pinus kesiya* in Northern Thailand in dependence on climate. *Forest Ecology and Management*, **226**, 279-289.
- Raupach MR (2005) Dynamics and optimality in coupled terrestrial energy, water, carbon and nutrient cycles. **301**, 223-238.
- Reich PB, Ellsworth DS, Walters MB, Vose JM, Gresham C, Volin JC, Bowman WD (1999) Generality of leaf trait relationships: A test across six biomes. *Ecology*, **80**, 1955-1969.
- Reichstein M, Tenhunen JD, Rouspard O, et al (2002) Severe drought effects on ecosystem CO₂ and H₂O fluxes at three Mediterranean evergreen sites: revision of current hypotheses? *Global Change Biology*, **8**, 999-1017.
- Rodriguez-Iturbe I, D'Odorico P, Porporato A, Ridolfi L (1999a) On the spatial and temporal links between vegetation, climate, and soil moisture. *Water Resources Research*, **35**, 3709-3722.
- Rodriguez-Iturbe I, D'Odorico P, Porporato A, Ridolfi L (1999b) Tree-grass coexistence in savannas: The role of spatial dynamics and climate fluctuations. *Geophysical Research Letters*, **26**, 247-250.
- Running SW, Hunt ER (1993) Generalization of a Forest Ecosystem Process Model for Other Biomes, BIOME-BCG, and an Application for Global-Scale Models. In: *Scaling Physiological Processes: Leaf to Globe* (eds Ehleringer JR, Field CB), pp. 141-158. Academic Press Inc., San Diego, CA, USA.
- Running SW, Coughlan JC (1988) A general-model of forest ecosystem processes for regional applications .1. hydrologic balance, canopy gas-exchange and primary production processes. *Ecological Modelling*, **42**, 125-154.
- Running SW, Gower ST (1991) FOREST-BGC, a General-Model of Forest Ecosystem Processes for Regional Applications .2. Dynamic Carbon Allocation and Nitrogen Budgets. *Tree physiology*, **9**, 147-160.
- Ryan MG (1991) Effects of climate change on plant respiration. *Ecological Applications*, **1**, 157-167.
- Ryan MG, Binkley D, Fownes JH, Giardina CP, Senock RS (2004) An experimental test of the causes of forest growth decline with stand age. *Ecological Monographs*, **74**, 393-414.
- Saco PM, Willgoose GR, Hancock GR (2007) Eco-geomorphology of banded vegetation patterns in arid and semi-arid regions. *Hydrology and Earth System Sciences*, **11**, 1717-1730.
- Schenk HJ, Jackson RB (2002) Rooting depths, lateral root spreads and below-ground/above-ground allometries of plants in water-limited ecosystems. *Journal of Ecology*, **90**, 480-494.

- Schimel DS, Braswell BH, Parton WJ (1997) Equilibration of the terrestrial water, nitrogen, and carbon cycles. *Proceedings of the National Academy of Sciences of the United States of America*, **94**, 8280-8283.
- Schymanski SJ, Roderick ML, Sivapalan M, Hutley LB, Beringer J (2008) A canopy-scale test of the optimal water-use hypothesis. *Plant Cell and Environment*, **31**, 97-111.
- Schymanski SJ, Roderick ML, Sivapalan M, Hutley LB, Beringer J (2007) A test of the optimality approach to modelling canopy properties and CO₂ uptake by natural vegetation. *Plant Cell and Environment*, **30**, 1586-1598.
- Schymanski SJ, Sivapalan M, Roderick ML, Beringer J, Hutley LB (2008) An optimality-based model of the coupled soil moisture and root dynamics. *Hydrology and Earth System Sciences*, **12**, 913-932.
- Schymanski SJ, Sivapalan M, Roderick ML, Hutley LB, Beringer J (2009) An optimality-based model of the dynamic feedbacks between natural vegetation and the water balance. *Water Resources Research*, **45**, W01412.
- Sellers PJ, Berry JA, Collatz GJ, Field CB, Hall FG (1992) Canopy Reflectance, Photosynthesis, and Transpiration .3. a Reanalysis using Improved Leaf Models and a New Canopy Integration Scheme. *Remote Sensing of Environment*, **42**, 187-216.
- Sullivan NH, Bolstad PV, Vose JM (1996) Estimates of net photosynthetic parameters for twelve tree species in mature forests of the southern Appalachians. *Tree physiology*, **16**, 397-406.
- Swift LW, Cunningham J, G.B., Douglass JE (1988) Climatology and hydrology. In: *Forest Hydrology and Ecology at Coweeta* (eds Swank WT, Crossley JDA), pp. 35-55. Springer-Verlag, New York, NY, USA.
- Tague CL, Band LE (2004) RHESys: Regional Hydro-Ecologic Simulation System--an object-oriented approach to spatially distributed modeling of carbon, water, and nutrient cycling. *Earth Interactions*, **8**, 1-42.
- Taiz L, Zeiger E (2002) *Plant physiology*. Sinauer Associates, Sunderland, MA, USA.
- Tarboton DG (1997) A new method for the determination of flow directions and upslope areas in grid digital elevation models. *Water Resources Research*, **33**, 309-319.
- Tardif JC, Conciatori F (2006) A comparison of ring-width and event-year chronologies derived from white oak (*Quercus alba*) and northern red oak (*Quercus rubra*), southwestern Quebec, Canada. *Dendrochronologia*, **23**, 133-138.
- Thornton PE (1998) Regional Ecosystem Simulation: Combining Surface- and Satellite-Based Observations to Study Linkages between Terrestrial Energy and Mass Budgets, PhD thesis, University of Montana, Missoula, MT, USA.

- Thornton PE, Law BE, Gholz HL, et al (2002) Modeling and measuring the effects of disturbance history and climate on carbon and water budgets in evergreen needleleaf forests. *Agricultural and Forest Meteorology*, **113**, 185-222.
- Tilman D (1988) Plant Strategies and the Dynamics and Structure of Plant Communities. Princeton University Press, Princeton, NJ, USA.
- Todd RL, Waide JB, Cornaby BW (1975) Significance of Biological Nitrogen Fixation and Denitrification in a Deciduous Forest Ecosystem. In: *Mineral Cycling in Southeastern Ecosystems* (eds Howell FG, Gentry JB, Smith MH), pp. 729-735, Technical Information Center, Office of Public Affairs, U.S. Energy Research and Development Administration, Oak Ridge, TN, USA.
- van der Tol C, Dolman AJ, Waterloo MJ, Meesters AGCA (2008a) Optimum vegetation characteristics, assimilation, and transpiration during a dry season: 2. Model evaluation. *Water Resources Research*, **44**, W03421.
- van der Tol C, Meesters AGCA, Dolman AJ, Waterloo MJ (2008b) Optimum vegetation characteristics, assimilation, and transpiration during a dry season: 1. Model description. *Water Resources Research*, **44**, W03422.
- Vitousek PM, Howarth RW (1991) Nitrogen Limitation on Land and in the Sea - how can it Occur. *Biogeochemistry*, **13**, 87-115.
- Vose JM, Bolstad PV (2006) Biotic and abiotic factors regulating forest floor CO₂ flux across a range of forest age classes in the southern Appalachians. *Pedobiologia*, **50**, 577-587.
- Vose JM, Bolstad PV (1999) Challenges to modelling NPP in diverse eastern deciduous forests: species-level comparisons of foliar respiration responses to temperature and nitrogen. *Ecological Modelling*, **122**, 165-174.
- Wang YP, Leuning R (1998) A two-leaf model for canopy conductance, photosynthesis and partitioning of available energy I: Model description and comparison with a multi-layered model. *Agricultural and Forest Meteorology*, **91**, 89-111.
- White MA, Thornton PE, Running SW, Nemani RR (2000) Parameterization and sensitivity analysis of the BIOME-BGC terrestrial ecosystem model: net primary production controls. *Earth Interactions*, **4**, 1-85.
- Whittaker RH (1956) Vegetation of the Great Smoky Mountains. *Ecological Monographs*, **26**, 1-69.
- Wigmosta MS, Vail LW, Lettenmaier DP (1994) A Distributed Hydrology-Vegetation Model for Complex Terrain. *Water Resources Research*, **30**, 1665-1679.
- Wilson JB (1988) A Review of Evidence on the Control of Shoot-Root Ratio, in Relation to Models. *Annals of Botany*, **61**, 433-449.

- Wilson KB, Baldocchi DD, Hanson PJ (2000) Spatial and seasonal variability of photosynthetic parameters and their relationship to leaf nitrogen in a deciduous forest. *Tree physiology*, **20**, 565-578.
- Wilson KB, Hanson PJ, Mulholland PJ, Baldocchi DD, Wullschleger SD (2001) A comparison of methods for determining forest evapotranspiration and its components: sap-flow, soil water budget, eddy covariance and catchment water balance. *Agricultural and Forest Meteorology*, **106**, 153-168.
- Wullschleger SD (1993) Biochemical Limitations to Carbon Assimilation in C₃ Plants - A Retrospective Analysis of the A/C_i Curves from 109 Species. *Journal of experimental botany*, **44**, 907-920.
- Yeakley JA, Swank WT, Swift LW, Hornberger GM, Shugart HH (1998) Soil moisture gradients and controls on a southern Appalachian hillslope from drought through recharge. *Hydrology and Earth System Sciences*, **2**, 41-49.
- Zak DR, Tilman D, Parmenter RR, Rice CW, Fisher FM, Vose J, Milchunas D, Martin CW (1994) Plant-Production and Soil-Microorganisms in Late-Successional Ecosystems - a Continental-Scale Study. *Ecology*, **75**, 2333-2347.

Chapter 3 Topography-mediated controls on local vegetation phenology estimated from MODIS vegetation index

3.1 Abstract

Forest canopy phenology is an important control of annual water and carbon budgets, and has been shown to respond to interannual climate variations. In mountainous areas, there may be a detailed spatial variation in phenology in response to well expressed topoclimate. The near real-time remote sensing products from the moderate-resolution imaging spectro-radiometer (MODIS) are invaluable in understanding vegetation phenology across different spatial scales. In this paper, we used the MODIS vegetation indices to derive the topography-mediated vegetation phenology at a local scale. A simple post-processing analysis using multi-year trajectories was developed to provide an efficient way to filter out unqualified data points. Four local phenological variables (mid-days of greenup/senescence, lengths of greenup/senescence) are estimated by non-linearly fitting time-series of transformed vegetation indices with a difference logistic function.

Phenological variables are then related to local topographical variables by multiple regression analysis. Elevation had the most explanatory power for all phenological variables. The mid-day of greenup period showed a strong linear relationship with elevation, while the other three variables (mid-day of senescence, and lengths of greenup/senescence) exhibited quadratic responses.

Radiation proxies (transformed aspect and potential relative radiation) also had significant explanatory power for all these variables. Though hillslope position was not observed to have a significant effect on vegetation phenology at this coarse resolution (about 230 m), interannual

variations of vegetation phenology between very wet and dry years showed that more extended periods of greenup/senescence are found without shifting mid-days of greenup/senescence. These topography-mediated controls on local vegetation phenology are closely related to micro-climate variations, vegetation community types, and hydrological position. The capability of detecting the topography-mediated local phenology also offers the potential to detect vegetation responses to climate change in mountainous terrains, and can serve as the basis to develop ecohydrological models incorporating space-time variations in vegetation phenology.

3.2 Introduction

In recent decades, changes in global vegetation phenology (e.g. timing of greenup and senescence) induced by global-warming have been studied by many researchers (e.g. Menzel and Fabian 1999; Zhou *et al.* 2001; Walther *et al.* 2002; Matsumoto *et al.* 2003). These changes are believed to be closely linked to the amplitude and timing of seasonal cycles of atmospheric CO₂ (Keeling *et al.* 1996; Myneni *et al.* 1997; Randerson *et al.* 1999; Churkina *et al.* 2005) (but see White and Nemani 2003; Angert *et al.* 2005 for counter example). Specifically, much research has focused on climate controls on vegetation phenology in the mid- and high-latitudes, where phenological patterns are more sensitive to global warming (Zhou *et al.* 2001; Randerson *et al.* 1999; White *et al.* 1997; Jenkins *et al.* 2002; Zhang *et al.* 2004, 2006). This is believed to occur because vegetation phenology in the mid- and high-latitudes is more controlled by temperature and photoperiod, while vegetation phenology in the tropics and in semi-arid areas is primarily controlled by seasonal rainfall (Childs 1988; Botta *et al.* 2000; Jolly and Running 2004; Jolly *et al.* 2005, and references therein). Single climate factors, however, are not always sufficient to explain vegetation phenology at a given location. Rather, multiple factors act on phenology together or at different phases of vegetation (White *et al.* 1997; Junttila 1980; Nilsen and Muller 1981; Partanen *et al.* 1998).

A time-series analysis of vegetation indices from global satellite images (e.g. normalized difference vegetation index, enhanced vegetation index) make it possible to understand phenological signals across different spatial scales (e.g. White *et al.* 1997; Jenkins *et al.* 2002; Zhang *et al.* 2006; Jolly and Running 2004; Schwartz *et al.* 2002; Fisher *et al.* 2006, 2007; Beck *et al.* 2006). Whereas several researchers have used field measurements to study the topography-mediated controls on vegetation phenology (e.g. Fisher *et al.* 2006; Seghieri and Simier 2002; Tateno *et al.* 2005; Richardson *et al.* 2006), few studies have used satellite imagery for this purpose. The lack of studies using global satellite products for topography-mediated vegetation phenology is mostly due to sensor coarse spatial scales, which may obscure the fine-scale variations in phenological signals despite their frequent temporal resolution (1 ~ 2 days).

Spatial variations in vegetation phenology have significant impacts on terrestrial ecohydrologic modeling at the local scale especially during vegetation transition periods (e.g. Nemani *et al.* 1993; Running and Nemani 1991; Obrist *et al.* 2003; Huntington 2004). Topography-related controls on vegetation phenology are not only mediated by micro-climate factors (e.g. temperature, radiation etc.), but also by species distributions, and hydrological gradients. Though most phenological models use climate variables (e.g. Jolly *et al.* 2005; Richardson *et al.* 2006; Chuine *et al.* 2000; Arora and Boer 2005), topographic factors (e.g. elevation, aspect and slope etc.) are more easily measurable and scalable especially in topographically complex regions. An understanding of the topography-mediated controls on vegetation phenology may therefore yield more accurate prediction of climate change effects on local vegetation in complex terrain.

The U.S. National Aeronautics and Space Administration (NASA) Earth Observing System (EOS; <http://modis.gsfc.nasa.gov/>) currently produces a global vegetation index (VI) for the entire terrestrial earth surface at 250-m spatial resolution (MOD13Q1) to provide a consistent measure of vegetation conditions from the MODerate Resolution Imaging Spectroradiometer (MODIS) sensor aboard Terra/Aqua platforms launched in 1999 and 2002 (Huete *et al.* 2002). The MODIS land

products offer significant advantages over previous global satellite products (e.g. AVHRR) in terms of radiometric and geometric properties, combined with improved calibration, atmospheric correction and cloud screening (Justice *et al.* 1998). Previous global satellite products often included high-level noise for the lack of precise calibration, cloud screening information, and view angle biases (e.g. Goward *et al.* 1991). MODIS land products provide more stable information on vegetation phenology in both the spatial and temporal domains, and have been successfully compared with field measurements (Zhang *et al.* 2003, 2004, 2006; Beck *et al.* 2006; Fisher and Mustard 2007; Sakamoto *et al.* 2005).

The MODIS spatial scale may not be fine enough to find all topography-mediated controls on local vegetation phenology, especially in topographically complex terrain, because major topographical factors still have significant sub-grid variability within a MODIS pixel. However, this approach can give us basic information on how vegetation phenology varies with topography, and which factors (e.g. micro-climate, hydrological position, and vegetation community types) are dominant in controlling phenology at the local scale.

The objectives of this study are (1) to develop a robust approach to extract phenological signals from the multi-year trajectories of MODIS NDVI, (2) to detect topography-mediated controls on local vegetation phenology at the MODIS scale, and (3) to understand these spatial phenological patterns based on spatial variations of micro-climate and other factors (e.g. vegetation community types, hillslope positions).

3.3 Materials and methods

3.3.1 Study area

The Coweeta Hydrologic Lab is located in western North Carolina, USA and is representative of the Southern Appalachian forest (Figure 3.1). The Southern Appalachian forest has very diverse

flora as a result of the complex terrain and consequent variability in microclimates and soil moisture (Whittaker 1956; Day and Monk 1974). Mean monthly temperature varies from 3.6 °C in January to 20.2 °C in July. The climate in the Coweeta Basin is classified as marine, humid temperate, and precipitation is relatively even in all seasons; annual precipitation ranges from 1870 mm to 2500 mm with about a 5% increase for each 100 m (Swift *et al.* 1988). The dominant canopy species are oaks and mixed hardwoods including *Quercus* spp. (oaks), *Carya* spp. (hickory), *Nyssa sylvatica* (black gum), *Liriodendron tulipifera* (yellow poplar), and *Tsuga canadensis* (eastern hemlock), while major evergreen undergrowth species are *Rhododendron maximum* (rhododendron) and *Kalmia latifolia* (mountain laurel) (Day *et al.* 1988). Spatial distributions of forest community types in this study area are closely related to the elevation, aspect, and moisture gradients (Figure 3.2; Day *et al.* 1988), associated with distinct phenological patterns as a function of topographic positions. Note that it is classified as Northern Hardwood forest types in higher elevation regions, dominated by *Betula lutea* (yellow birch), *Tilia heterophylla* (basswood), *Aesculus octandra* (buckeye), and *Q. rubra* (northern red oak) etc. The local vegetation phenology is well preserved in the study site, even though there were some partial logging experiments in several of the watersheds in the 1950's and 1970's. Detailed disturbance histories for the sub-watersheds are available at the Coweeta LTER homepage (<http://coweeta.ecology.uga.edu/ecology/cbase.html>).

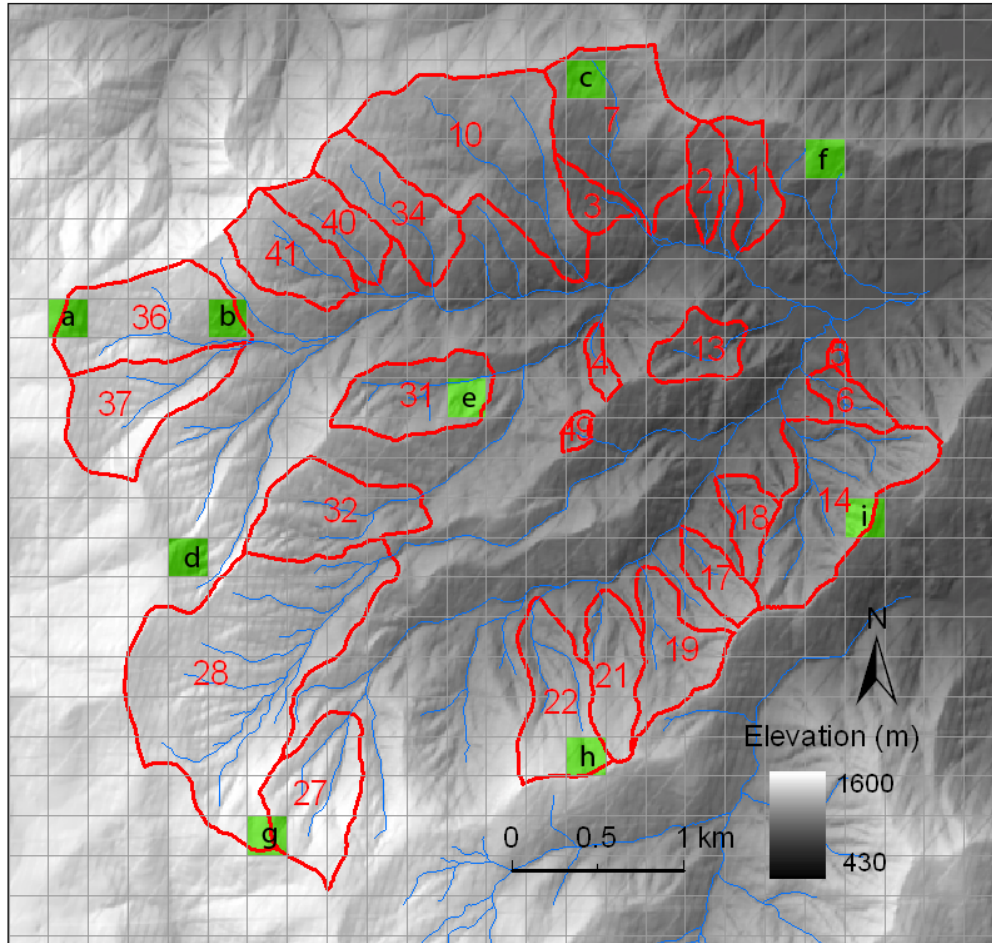


Figure 3.1: A study site (Coweeta Hydrologic Lab). Grids represent the MODIS (MOD13Q1; about 230 m) pixels. Red lines represent the boundaries of watersheds. Letters indicates the pixels for examples of filtering and fitting methods (Figure 3.3; Figure 3.4).

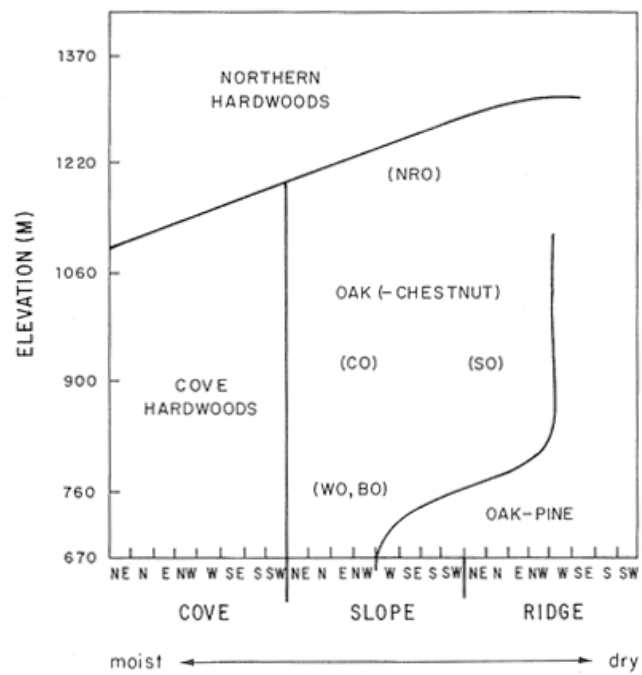


Figure 3.2: A typic diagram from Day *et al.* (1988), which describes vegetation community types within the study site as a function of slope, aspect, elevation, and hillslope positions.

3.3.2 MODIS vegetation index

Due to its high temporal frequency, the MODIS normalized difference vegetation index (NDVI) is particularly useful to detect subtle phenological changes. NDVI is a normalized ratio between of surface reflectance red and near infrared bands:

$$NDVI = (\rho_{NIR} - \rho_{RED}) / (\rho_{NIR} + \rho_{RED}) \quad (3.1)$$

where ρ_{RED} and ρ_{NIR} are surface reflectance of red and near-infrared bands, respectively. MODIS VI products (MOD13Q1 version 5) are released in the HDF-EOS data format as Sinusoidal projections with 16-day temporal resolution and approximately 250-m spatial resolution (Huete *et al.* 2002), reprojected to the GeoTIFF file format with the Universal Transverse Mercator (UTM) coordinate system by MODIS reprojection tool (MRT;

https://lpdaac.usgs.gov/lpdaac/tools/modis_reprojection_tool).

NDVI, however, usually has a non-linear relationship with Leaf Area Index (LAI) (Myneni *et al.* 2002), which is a more meaningful measure of actual vegetation. This non-linearity can result in significant bias, including exaggerated phenological signals in low NDVI ranges (Fisher *et al.* 2006). We estimated this non-linear relationship locally by matching 1-km MODIS NDVI (MOD13A2) and LAI (MOD15A2) of the study area. We then use this relationship to transform the 250-m MODIS NDVI (MOD13Q1) into estimated LAI values to analyze phenological signals.

There are two main reasons why we used transformed MODIS NDVI (MOD13Q1) values rather than MODIS LAI (MOD15A2) values for extracting local phenological patterns. First, MODIS LAI is temporally unstable even though they are provided more frequently (8-day temporal resolution) than MODIS NDVI. It seems that both quality control (QC) and the extra QC flags in MOD15 cannot remove unqualified data well because of the substantial spatial variations in microclimate in this humid and mountainous area. Second, MODIS LAI (MOD15A2) is currently provided only at

about 1-km spatial resolution, which is too coarse to retrieve the differences in phenological patterns between various topographic positions in this complex terrain.

In the production of VI values from 2001 to 2008, only good and marginal VI values were chosen based on the pixel reliability values, a parameter which was recently added to MODIS VI products (version 5) and is usually recommended for post-processing analysis (Didan and Huete 2006). We included marginal data for this study because there were not enough points with good quality data to show the full phenological patterns, and even good quality data have unreasonable phenological patterns by cloud contaminations in this high-precipitation region. Rather, we incorporated the post-processing analysis to remove false data points. The day of composite information at each pixel, another parameter recently added into collection 5 datasets of MODIS VI, was also retrieved to get the exact acquisition date during each composite period (Didan and Huete 2006). This information was suggested to be quite important for extracting exact phenological signals (Fisher and Mustard 2007).

Two experimental watersheds (WS01, WS17; Figure 3.1), where white pine (*Pinus strobus* L.) was planted in 1957 and 1956 respectively, were masked with adjacent pixels to exclude the distinct phenological patterns featured by coniferous forests. Also, three experimental watersheds that were recently subjected to artificial treatments (WS06, WS07, and WS13; Figure 3.1) were excluded because full successional vegetation is not yet established.

3.3.3 *Post-processing analysis*

There are several traditional filtering or fitting methods developed for time-series VI, including the Best Index Slope Extraction (BISE) method (Viovy *et al.* 1992), the modified BISE algorithm (Lovell and Graetz 2001), the Fourier Transform (FT) algorithm (Olsson and Eklundh 1994; Verhoef *et al.* 1996; Roerink *et al.* 2000), the wavelet transform algorithm (Sakamoto *et al.* 2005), the weighted least-square linear or non-linear fit method (Jonsson and Eklundh 2002; Chen *et al.*

2004), and the mean-value iteration filter (Ma and Veroustraete 2006). As discussed previously, MODIS land products offer significant advantages over earlier global satellite products in terms of radiometric and geometric properties (Running *et al.* 2000; Heinsch *et al.* 2003). We integrated two-step simple filtering methods to identify occasional sudden negative or positive spikes not indicated by the quality assurance flags as false VI values. Most spikes were negative forms due to remnant cloud cover, aerosols, or cloud shadow, all of which tend to decrease the NDVI values (Didan and Huete 2006).

First, we eliminated unqualified data points from 8-year historical phenological trajectories (2001 ~ 2008) by assuming that temporal phenological patterns of forest-based ecosystems are quite periodic and that interannual variations are relatively small. From historical trajectories of estimated MODIS LAI as a function of day of year at each pixel (Figure 3.3), we made a group at each data point by identifying all data points occurring within 16 days before and after. If the data point is classified as an outlier beyond the ends of the Whiskers, defined as 1.5 times the inter-quartile range from the lower and upper quartiles of the group, we excluded it from further analysis. By including the 16 days before and after each LAI value for this outlier-exclusion analysis, we can account for interannual variations in phenological changes, especially in transition periods, and obtain statistically significant numbers for outlier analysis. This outlier-exclusion technique can be applied to both sides, so that positive spikes can be filtered without specifying different threshold values (Figure 3.3).

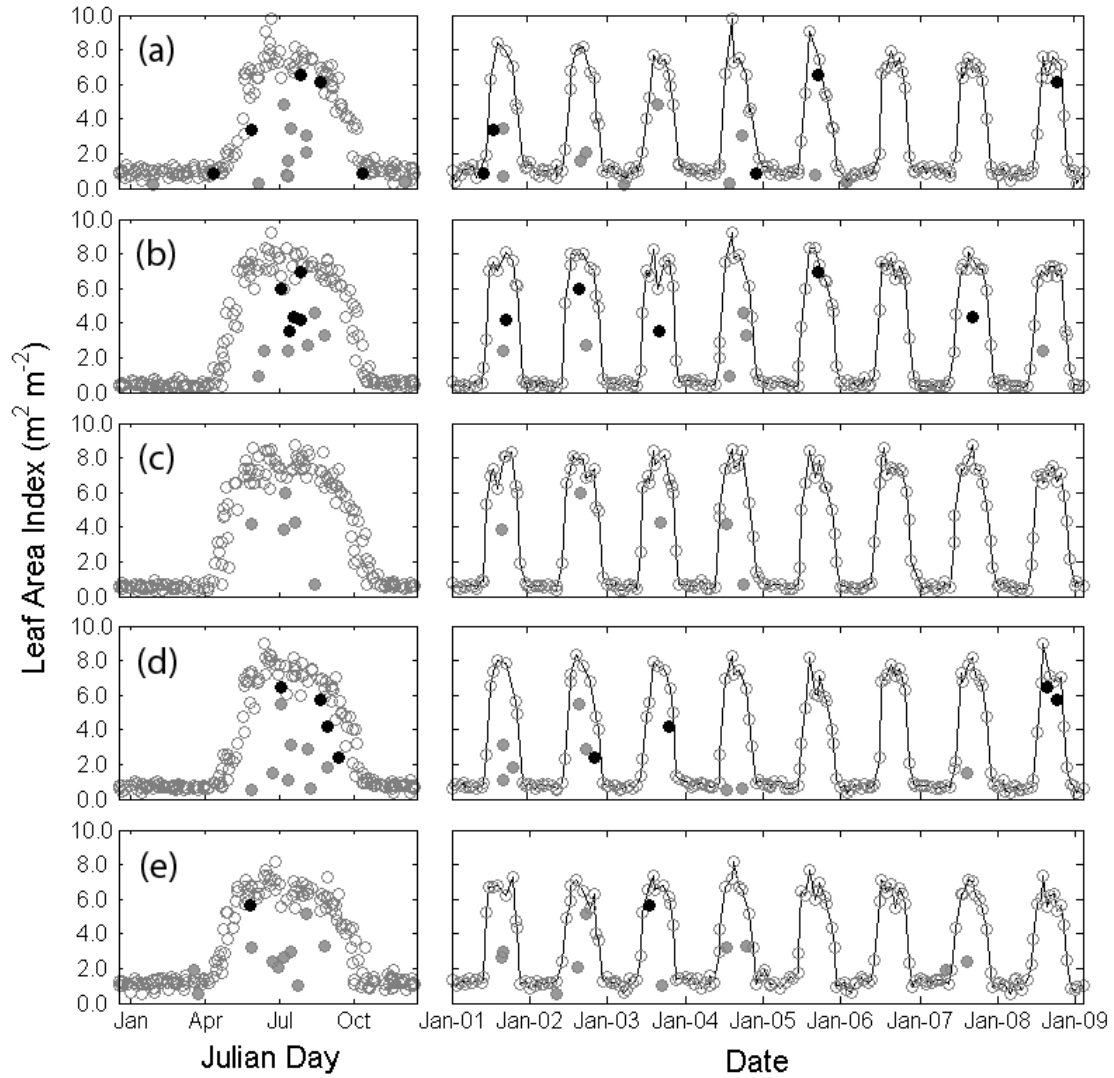


Figure 3.3: Examples of two-step filtering methods from 8-year historical trajectories (left column) and time-series (right column) of estimated LAI at selected MODIS pixels ((a) ~ (i); Figure 3.1). Grey and black dots represent filtered values by the outlier exclusion analysis and the modified BISE methods, respectively.

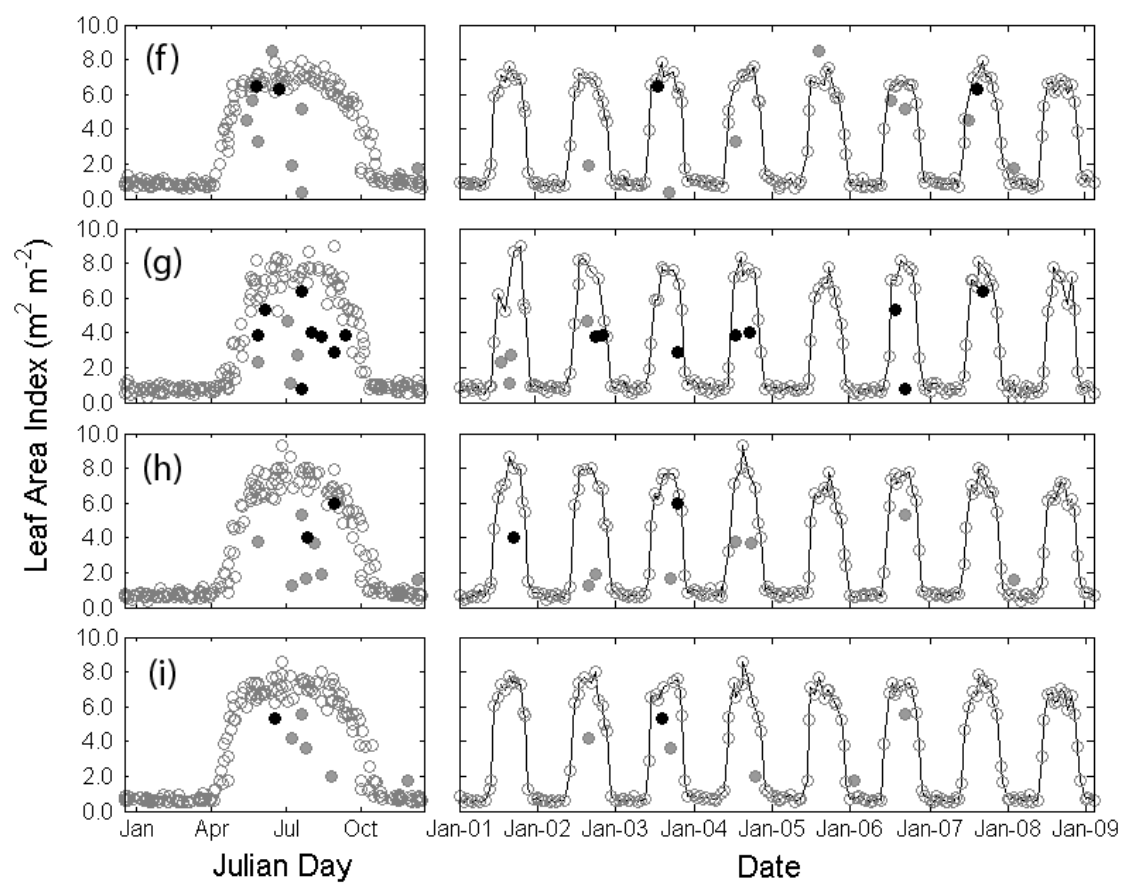


Figure 3.3 (cont'd)

Second, we used the modified BISE method with a 30-day window size to remove the remnant spikes (Lovell and Graetz 2001). Recently, this method was also applied to the temporal MOD15 data as a complementary or post-process method after filtering the data with the original quality control flags (Reichstein *et al.* 2007). A main difference between our method and the original method is that we applied the modified BISE method to time-series of transformed LAI values, by which we are using stricter threshold values in high VI ranges than low VI ranges. We did not use the modified BISE method alone mainly because it was not working well with consecutive false composite VI data points with a narrow window size, which are common phenomena in this humid region. Increasing the window size can solve some of these problems, but it can result in the loss of distinct phenological signals by over-smoothing (Viovy *et al.* 1992).

Our simple filtering technique was very effective in excluding unqualified data points from the time-series of transformed MODIS LAI values for selected pixels in topographically different positions in the study site (Figure 3.3). This outlier-exclusion method from historical trajectories is especially useful for rare positive spikes and consecutive false data points from composite periods. It also worked well around transition periods by allowing flexibility in interannual phenological variations, when unqualified data points could easily be confused with real phenological signals.

3.3.4 A phenology model for multi-year VI datasets

A common phenology model for temporal MODIS VI or LAI values is the logistic function (Zhang *et al.* 2003, 2004; Ahl *et al.* 2006; Kang *et al.* 2003), which can be expressed as:

$$y(t) = \frac{c}{1 + e^{a+bt}} + d \quad (3.2)$$

where $y(t)$ is the NDVI or LAI value at time t (day of year), a and b are fitting coefficients, d is the minimum or background NDVI or LAI value, and c is the difference between maximum and

minimum NDVI or LAI. Logistic phenology models are generally used for a single growth or senescence phase (Zhang *et al.* 2003), which may be hard to define from a multi-year time series of MODIS VI or LAI. Phenological changes in forest-based ecosystems, however, are quite periodic (as opposed to grass-based ecosystems), so there is usually a single mode of growth and senescence per year. We therefore selected the difference logistic function to develop a functional representation of a one-year period from multi-year records of LAI values (Fisher *et al.* 2006). The difference logistic function has the following form:

$$y(t) = \left(\frac{1}{1 + e^{a+bt}} - \frac{1}{1 + e^{a'+b't}} \right) \cdot c + d \quad (3.3)$$

where a and b are fitting variables for the greenup period, and a' and b' are fitting variables for the senescence period. In this model, all available multi-year MODIS LAI data are analyzed together as a function of day of year, which helps us extract the general topography-mediated controls on vegetation phenology without considering interannual variations. The difference logistic function has been shown to describe time-series of NDVI data better than the Fourier series or the asymmetric Gaussian function (Beck *et al.* 2006). This model also reduces the number of fitting variables and assures the continuity of maximum and minimum LAI values between phases in multi-year LAI datasets.

We used the nonlinear regression function (*nlinfit*) in Matlab (Matlab R2007b, MathWorks Inc., Natick, MA) to find least-squares parameter estimates for the difference logistic model. This function uses the Gauss-Newton algorithm with Levenberg-Marquardt modifications for global convergence (Seber and Wild 1989). The fitting mechanism was halted either after 2000 iterations, or when marginal improvements of the residual sum of squares fell below the specified threshold (10^{-8}).

Stable fitted temporal patterns of MODIS LAI are established at MODIS pixels in topographically different positions within the study area, averaged from the 8-year period (2001 ~

2008) (Figure 3.4). Distinct phenological patterns were found at different topographic positions within the study area, induced by the combined effects of micro-climate conditions, vegetation types and hillslope positions.

3.3.5 *Analytical solutions for phenological transition dates*

Following Zhang *et al.* (2003, 2004), phenological transition dates (greenup, maturity, senescence, and dormancy onset) in the logistic model can be determined from the local minima and maxima for the rate of curvature change (CCR; grey lines in Figure 3.5d), the derivative of the signed curvature of the logistic function (Eq. 3 in Zhang *et al.* 2003). Because this equation cannot be solved analytically, cumbersome numerical solutions are usually used to find the local minima and maxima for transition dates (Ahl *et al.* 2006).

However, if the slope (y') is relatively small, the approximation of the signed curvature (κ) is equivalent to the second derivative (y'') as follows:

$$\kappa = \frac{y''}{(1 + y'^2)^{3/2}} \approx y'' \quad (3.4)$$

In this case, transition dates (t') can be obtained from the analytic solution of the fourth derivative of the logistic function as follows (Appendix):

$$t' = \frac{\ln(5 \pm 2\sqrt{6}) - a}{b} \quad (3.5)$$

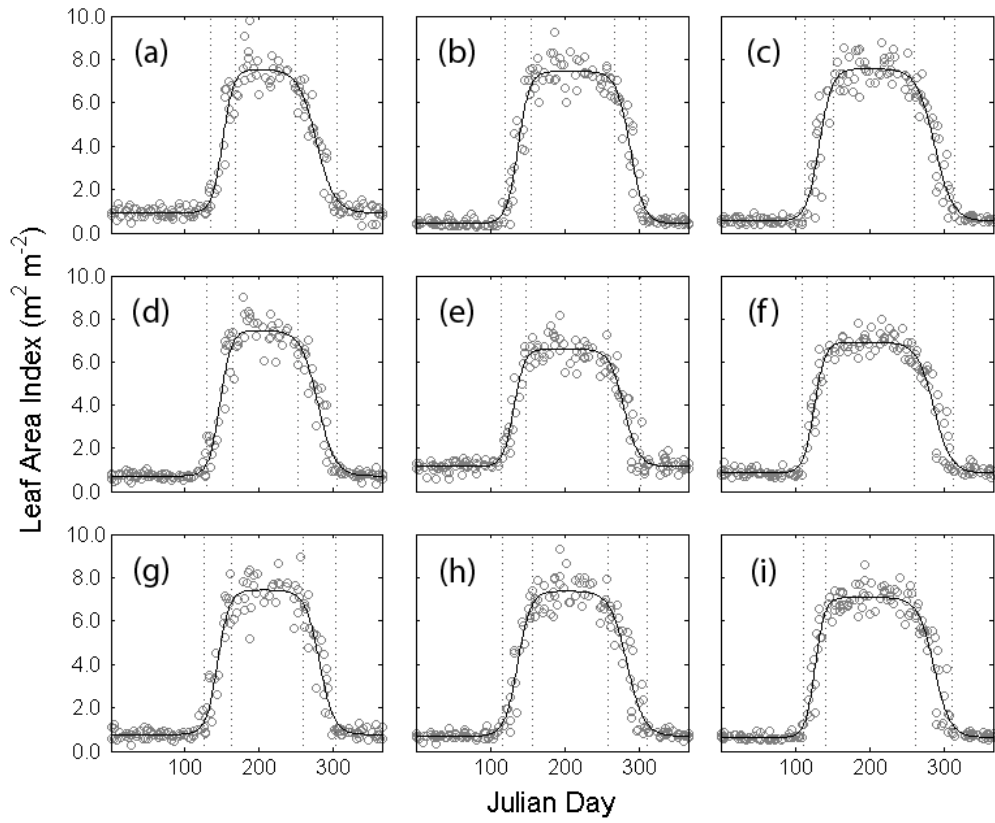


Figure 3.4: Examples of the difference logistic function fitting for 8-year estimated LAI datasets at selected MODIS pixels ((a) ~ (i); Figure 3.1). Vertical dotted lines are phenological transition dates (t) from Eq. 3.5.

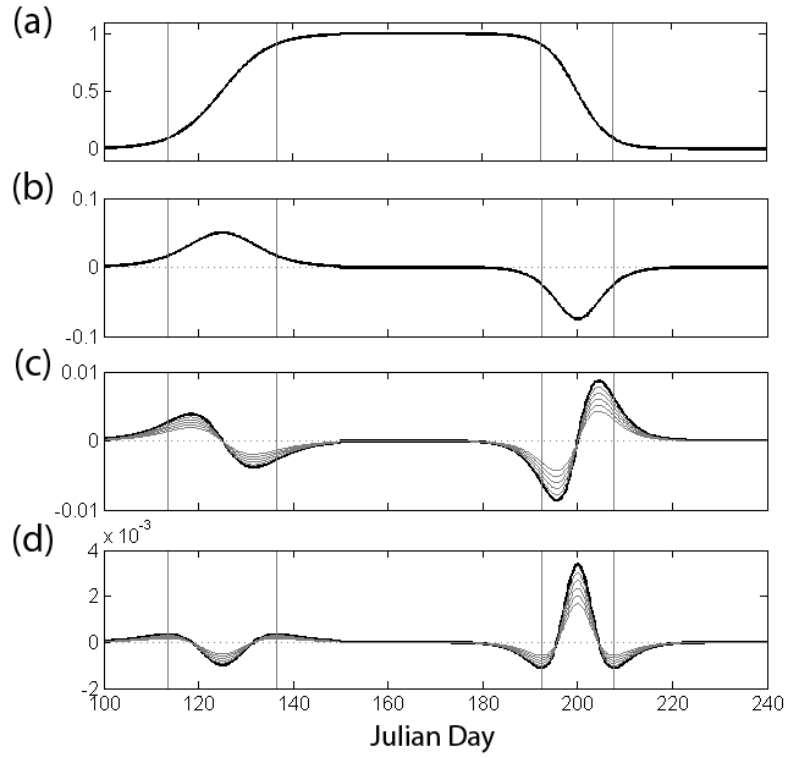


Figure 3.5: Analytical solutions of phenological variables; (a) the difference logistic function, (b) the first derivative, (c) the second derivative (a thick line) and curvature (grey lines; Eq. 3.4), and (d) the third derivative (a thick line) and the rate of curvature change (CCR; grey lines). The curvature and CCR curves are drawn with different c parameter values (0.5 ~ 4.0; Eq. 3.2). The vertical grey lines are analytical solutions for phenological variables from Eq. 3.5, not changed with different c parameter values.

Even in cases when the slope (y') is not relatively small, the transition dates at which the local minima and maxima values are established do not change (Figure 3.5d) because the slope (y') values determine only amplitudes of the curvature curves (Eq. 3.4). This property of the logistic function is shown in Figure 3.5, where the first (Figure 3.5b), second (Figure 3.5c), and third (Figure 3.5d) derivative curves of the logistic function (Figure 3.5a) were drawn with the curvature functions (grey lines in Figure 3.5c) and rate of curvature functions (grey lines in Figure 3.5d) for different values of the c parameter (0.5 ~ 4.0; Eq. 3.2). Analytical solutions for the local maxima and minima of the third derivative (Appendix) from Eq. 3.5 (vertical lines in Figure 3.5) are the same as those for the rate of curvature change (Figure 3.5d), and do not change with different c parameter values.

From these solutions, we can calculate the length of growth and senescence periods between two transition dates to characterize the local phenological patterns of the study site (Eq. 3.6). Note that each length of greenup/senescence period ($Length_{on}$ or $Length_{off}$) is only a function of the b (or b') parameter related to the shape of the logistic function.

$$Length = \log\left(\frac{5 + 2\sqrt{6}}{5 - 2\sqrt{6}}\right) / b \quad (3.6)$$

The above two equations (Eq. 3.5 and 3.6) show that phenological transition dates are only a function of the a and b parameters, while the lengths of greenup/senescence periods ($Length_{on}$ and $Length_{off}$) are determined only by the b parameter.

We used the mid-day of leaf greenup/senescence periods (Mid_{on} and Mid_{off}) for the statistical analysis in this study, equivalent to inflection points for the difference logistic function (Figure 3.5b). These dates can easily be calculated from the a and b parameters ($-a/b$), where NDVI or LAI values are established at the half-point between maximum and minimum values. These inflection points have been incorporated by several previous phenological studies (White *et al.* 1997, 2002;

Schwartz *et al.* 2002; Fisher *et al.* 2006; Fisher and Mustard 2007; Bradley *et al.* 2007) for a number of different reasons. First, NDVI values at low ranges are often mixed with soil reflectance because they are very sensitive to canopy background variations (Huete 1988; Huete *et al.* 1994). Second, these points are more ecologically meaningful and measurable in that the change rates of greenness are most rapid around these dates (White *et al.* 1997). Third, solving for the inflection points can create a more robust solution for vegetation phenology reducing the errors in conventional transition dates (e.g. greenup, maturity, senescence, and dormancy onset) associated with their greater sensitivity to data availability and to early spring understory growth (Fisher *et al.* 2006).

3.3.6 Topographical variables

We relate phenological variables to basic topographic variables (e.g. elevation, aspect, slope, and wetness index) for each MODIS pixel (Figure 3.1). Elevation (*elev*) data were upscaled from North Carolina LIDAR digital elevation model (about 6.1-m resolution dataset from the North Carolina flood mapping program: <http://www.ncfloodmaps.com>). In this region, elevation is related not only to local temperature with lapse rate (Bolstad *et al.* 1998), but also to precipitation which increases by approximately 5% with each 100 m rise in elevation (Swift *et al.* 1988). From these upscaled elevation datasets, aspect and slope were calculated at the same spatial scale. To create a more direct measure of radiation load for statistical analysis, aspect was transformed into a relative number ranging from -1 (for northeast-facing slopes) to 1 (for southwest-facing slopes) (*taspect*) (Beers *et al.* 1966).

$$taspect = -\cos(aspect - 45^\circ) \quad (3.7)$$

Slope is also related to incoming radiation. In addition, the transformed aspect term cannot explain seasonal variation in incoming radiation, which is a function of solar zenith and azimuth

angles. Potential relative radiation (*PRR*; Pierce *et al.* 2005) is introduced to better represent seasonal radiation potential at each topographic position, using the *Hillshade* function in ArcGIS (ArcGIS 9.2, ESRI Inc., Redlands, CA). While transformed aspect (*taspect*) only uses aspect to estimate radiation potentials, *PRR* sums up hourly hillshade radiation calculated from aspect, slope, solar zenith, and azimuth angles. We calculated *PRR* values for each month using mean solar period, and then derived the growing season (Apr, May; *PRR_g*), senescence season (Oct, Nov; *PRR_s*), and whole-year *PRR* values.

Wetness index (*topidx*; Beven and Kirkby 1979) was calculated at the original LIDAR elevation data scale to represent hydrological gradients with hillslope position, then upscaled to the MODIS scale. This is because detailed hydrological variations can be lost when we calculate wetness index at the MODIS scale, in contrast to aspect and slope. Upslope contributing area for the wetness index was calculated with the *D*-infinity (D_{∞}) method, which allows flow to be proportioned among multiple neighboring downslope pixels according to gradient (Tarboton 1997).

All phenological and topographic variables are summarized in

Table 3.1.

3.3.7 *Interannual variations between wet and dry years*

At the MODIS scale, much of the local topographic variations are lost by being aggregated to coarse spatial resolution, and the range of wetness indices is significantly reduced. This scale issue makes it more difficult to detect the topography-mediated controls on vegetation phenology in terms of hillslope position. For this reason, we decided to compare phenological variables between very wet and very dry years to determine whether soil moisture status has a significant effect on vegetation phenology.

Table 3.1: Summary of phenological and topographic variables

Abbreviation	Description	Unit	Equation or reference
Phenological variables			
Mid_{on}	Mid-day of the greenup period	DOY	$-a/b$ from Eq. 3.3
Mid_{off}	Mid-day of the senescence period	DOY	$-a'/b'$ from Eq. 3.3
$Length_{on}$	Length of the greenup period	days	Eq.3.6
$Length_{off}$	Length of the senescence period	days	Eq.3.6
LAI_{min}	Fitted minimum LAI value	unitless	d from Eq. 3.3
LAI_{max}	Fitted maximum LAI value	unitless	$c+d$ from Eq. 3.3
Topographic variables			
$elev$	Elevation	m	http://www.ncfloodmaps.com
$taspect$	Transformed aspect	unitless	Eq.3.7
PRR	Potential relative radiation for the whole year	unitless	(Pierce <i>et al.</i> 2005)
PRR_g	Potential relative radiation for growing season	unitless	PRR from Apr, May
PRR_f	Potential relative radiation for falling season	unitless	PRR from Oct, Nov
$topidx$	Wetness index (or topographic index)	unitless	(Beven and Kirkby 1979)

In this region, we have experienced exceptionally wet and dry situations since 2000. Phenological signals were assembled and analyzed from two extremely dry years (2002, 2008) and two extremely wet years (2003, 2005), with drought conditions determined by the Palmer Drought Severity Index (Palmer 1965). By using phenological signals from independent years of extreme moisture conditions, we may attribute phenological differences to interannual variations of moisture condition, minimizing the effect of interannual variations of other climate variables (e.g. temperature, radiation etc.). We may also explore how major topography-mediated controls on vegetation phenology change between wet and dry years, and how we can interpret such changes with respect to the role of moisture status for vegetation phenology.

3.3.8 Statistical analysis

We used a multiple regression analysis to relate phenological variables to topographic variables. A multiple regression allows us to test and model multiple independent variables (topographic variables) simultaneously with one predictor variable (phenological variables). Correlation and interactions between explanatory variables often complicate the multiple regression analysis, especially in case of near-linear relations among explanatory variables, leading to unstable parameter estimates. For this reason, we did not include the slope variable in this analysis. In this study area, there is a significant positive correlation between slope and elevation (Pearson correlation coefficients; $R = 0.592$, $P < 2 \times 10^{-16}$), and the inclusion of the slope factor would complicate the interaction structure of the data. A Pearson correlation matrix between all explanatory and response variables indicates that there is no significant correlation among explanatory variables (Table 3.2) except for the correlation between radiation proxies (transformed aspect and PRR values). Therefore, only one radiation proxy was used for multiple regression analysis at a time, *taspect* (*model 1*) or PRR (*model 2*) (Table 3.3). In addition, each seasonal PRR value (PRR_g or PRR_f) seems to be more correlated to each seasonal phenological variable than to

the other seasonal *PRR* value or the whole-year *PRR* value (Table 3.2). We therefore used each seasonal *PRR* value, instead of the whole-year *PRR* value, as a radiation proxy in *model 2*. Paired graphs show some possible non-linear responses to explanatory variables (Figure 3.6). We therefore included quadratic terms for each of three explanatory variables, as well as interaction terms among explanatory variables for both models. Correlation coefficients of fitted LAI values (LAI_{min} and LAI_{max}) with topographic and other phenological variables show the spatial pattern of vegetation type and their relationship with vegetation phenology in this study site (Table 3.2). A strong negative correlation between LAI_{min} and LAI_{max} ($R = -0.697$, $P < 2 \times 10^{-16}$; Table 3.2) indicates that their spatial pattern is related to the vegetation composition of coniferous and understory evergreen species (Figure 3.2), represented with lower NDVI in summer and higher NDVI in winter. Therefore, LAI_{min} effectively represent the amount of evergreen vegetation which has distinct phenological patterns compared to deciduous broadleaf forests. To explain the effect of evergreen vegetation in phenological signals, LAI_{min} was also added into explanatory variables in the multiple regression analysis.

To minimize the risk of over-parameterization, we used the automatic model simplification function *stepAIC* in Package **MASS** version 7.2 for R (version 2.7.0, The R Foundation for Statistical Computing) for parsimonious models, which performs stepwise model selection by a penalized log-likelihood (Akaike's Information Criterion). We also manually pruned insignificant variables in sequence ($P > 0.005$) (see Crawley 2007 for a detailed methodology).

The analysis of covariance technique is incorporated to test the inequality of regression lines (for separate lines) between topographic controls on vegetation phenology for wet and dry years. This technique allows us to test whether the responses of the independent variables (phenological variables) are different between groups as a linear function of the predictor variables (topographic variables). Only major linear topographic controls on vegetation phenology were tested to simplify this procedure.

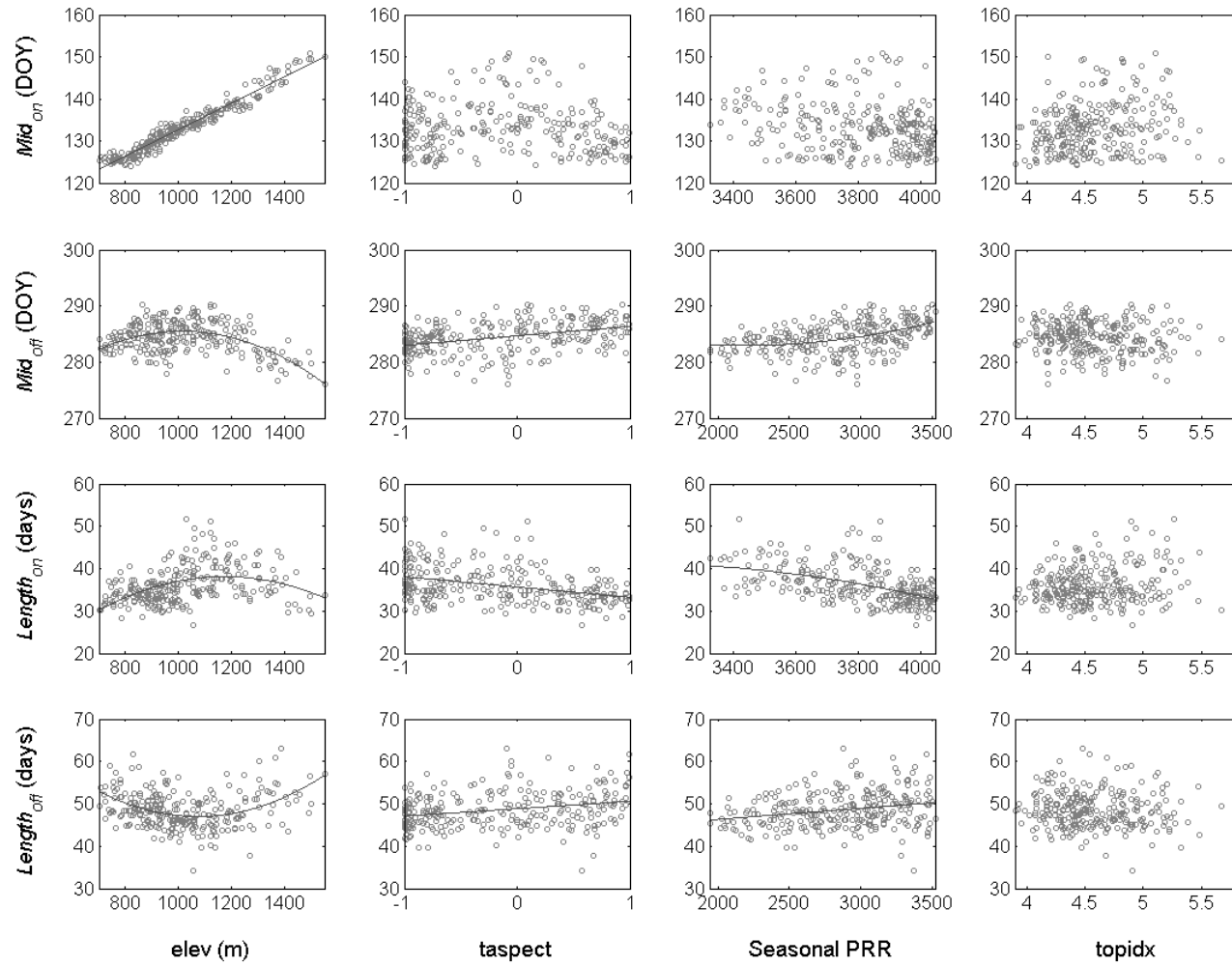


Figure 3.6: Paired scatter plots between topographic and phenological variables. Fitted lines show strongly significant relationships from multiple regression models (Table 3.3).

Table 3.2: Pearson correlation coefficients between topographic factors and phenological variables ($n = 252$)

	<i>elev</i>	<i>taspect</i>	<i>PRR</i>	<i>PRR_g</i>	<i>PRR_f</i>	<i>topidx</i>	<i>Mid_{on}</i>	<i>Mid_{off}</i>	<i>Length_{on}</i>	<i>Length_{off}</i>	<i>LAI_{min}</i>	<i>LAI_{max}</i>
<i>elev</i>	1.0											
<i>taspect</i>	-0.051	1.0										
<i>PRR</i>	-0.129	0.915	1.0									
<i>PRR_g</i>	-0.247	0.841	0.966	1.0								
<i>PRR_f</i>	-0.110	0.919	0.998	0.954	1.0							
<i>topidx</i>	0.112	-0.134	-0.132	-0.138	-0.127	1.0						
<i>Mid_{on}</i>	0.972	-0.040	-0.103	-0.218	-0.084	0.180	1.0					
<i>Mid_{off}</i>	-0.229	0.373	0.397	0.384	0.395	-0.070	-0.327	1.0				
<i>Length_{on}</i>	0.307	-0.371	-0.455	-0.514	-0.440	0.159	0.251	-0.085	1.0			
<i>Length_{off}</i>	0.058	0.193	0.183	0.162	0.184	-0.049	-0.108	-0.410	-0.124	1.0		
<i>LAI_{min}</i>	-0.440	-0.137	-0.101	-0.007	-0.113	-0.135	-0.324	-0.523	-0.281	0.028	1.0	
<i>LAI_{max}</i>	0.766	-0.008	-0.117	-0.246	-0.098	0.079	0.698	0.148	0.471	0.069	-0.697	1.0

3.4 Results

3.4.1 Topographical controls on local vegetation phenology

Summaries of the multiple regression analyses are shown in Table 3.3. For both models (*Model 1* and *Model 2*), *elev* usually has the most explanatory power for all phenological variables. However, in both models *Mid_{on}* exhibits a linear relationship with *elev*, while the other three phenological variables (*Mid_{off}*, *Length_{on}*, and *Length_{off}*) exhibit quadratic responses. Radiation proxies (*taspect* and seasonal *PRRs*) are also significant for phenological variables ($P < 0.005$), which usually exhibit linear relationships with *taspect*, and linear or quadratic relationships with seasonal *PRRs*. For both models, *LAI_{min}* is strongly significant for two mid-day phenological variables (*Mid_{on}* and *Mid_{off}*), whereas *topidx* has some explanatory power only for *Mid_{on}*. All interaction and quadratic terms other than *elev*taspect*, *elev*², and *PRR*² are insignificant for both models.

Introducing the seasonal *PRR* (*PRR_g* or *PRR_f*) as a radiation proxy resulted in some improvement in model performance (R^2) for *Mid_{off}* and *Length_{on}* (Table 3.3). Moreover, 95% confidence intervals for the coefficients of the remaining independent variables (*elev*², *elev*, and *topidx*) overlapped significantly for both models, indicating that the choice of radiation proxy has minimal influence on the relationships among other topographic and phenological variables.

The mid-day of greenup period (*Mid_{on}*) is delayed by about 3.1 days for every 100 m increase in elevation (Figure 3.7). This pattern of delay with elevation is quite comparable to Hopkin's Law which states the onset of spring is delayed by one day with 30 m increase in elevation (Hopkins 1918; Fitzjarald *et al.* 2001). Interestingly, fitted quadratic graphs between elevation and phenological variables show very similar ranges of the inflection point from the 1100 m to 1200 m elevation bands (Figure 3.7), usually regarded as a transition zone from the Southern Appalachian forests to the Northern Hardwood forests (Figure 3.2).

Table 3.3: Summaries of multiple regression models ($n = 252$)

	Model 1 (<i>taspect</i>)	Model 2 (<i>PRR</i>)
<i>Mid_{on}</i>	Equation: $Mid_{on} \sim elev + topidx + taspect + LAI_{min} + elev * taspect$	Equation: $Mid_{on} \sim elev + topidx + PRR_g + LAI_{min}$
	Coefficients $elev: 3.40 \times 10^{-2} \pm 4.17 \times 10^{-4} (P < 2 \times 10^{-16})$ $topidx: 1.57 \pm 0.18 (P = 1.02 \times 10^{-15})$ $taspect: -3.00 \pm 0.63 (P = 2.90 \times 10^{-6})$ $LAI_{min}: 4.86 \pm 0.38 (P < 2 \times 10^{-16})$ $elev * taspect: 3.53 \times 10^{-3} \pm 6.4 \times 10^{-4} (P = 8.54 \times 10^{-8})$	Coefficients $elev: 3.35 \times 10^{-2} \pm 4.2 \times 10^{-4} (P < 2 \times 10^{-16})$ $topidx: 1.51 \pm 0.19 (P = 9.95 \times 10^{-14})$ $PRR_g: 1.63 \times 10^{-3} \pm 3.8 \times 10^{-4} (P = 2.08 \times 10^{-5})$ $LAI_{min}: 4.45 \pm 0.39 (P < 2 \times 10^{-16})$
	Multiple R^2 : 0.972	Multiple R^2 : 0.969
<i>Mid_{off}</i>	Equation : $Mid_{off} \sim elev^2 + elev + taspect + LAI_{min}$	Equation : $Mid_{off} \sim elev^2 + elev + PRR_f^2 + LAI_{min}$
	Coefficients: $elev^2: -2.74 \times 10^{-5} \pm 2.2 \times 10^{-6} (P < 2 \times 10^{-16})$ $elev: 5.16 \times 10^{-2} \pm 4.8 \times 10^{-3} (P < 2 \times 10^{-16})$ $taspect: 1.16 \pm 0.14 (P = 4.39 \times 10^{-15})$ $LAI_{min}: -9.10 \pm 0.52 (P < 2 \times 10^{-16})$	Coefficients: $elev^2: -2.75 \times 10^{-5} \pm 2.2 \times 10^{-6} (P < 2 \times 10^{-16})$ $elev: 5.21 \times 10^{-2} \pm 4.7 \times 10^{-3} (P < 2 \times 10^{-16})$ $PRR_f^2: 3.61 \times 10^{-7} \pm 4.0 \times 10^{-8} (P < 2 \times 10^{-16})$ $LAI_{min}: -9.04 \pm 0.51 (P < 2 \times 10^{-16})$
	Multiple R^2 : 0.751	Multiple R^2 : 0.761
<i>Length_{on}</i>	Equation : $Length_{on} \sim elev^2 + elev + taspect + LAI_{min}$	Equation : $Length_{on} \sim elev^2 + elev + PRR_g^2 + LAI_{min}$
	Coefficients: $elev^2: -3.39 \times 10^{-5} \pm 5.6 \times 10^{-6} (P = 6.74 \times 10^{-9})$ $elev: 7.78 \times 10^{-2} \pm 1.23 \times 10^{-2} (P = 1.31 \times 10^{-9})$ $taspect: -2.60 \pm 0.36 (P = 3.23 \times 10^{-12})$ $LAI_{min}: -4.43 \pm 1.33 (P = 0.00096)$	Coefficients: $elev^2: -3.25 \times 10^{-5} \pm 5.3 \times 10^{-6} (P = 4.11 \times 10^{-9})$ $elev: 7.26 \times 10^{-2} \pm 1.17 \times 10^{-2} (P = 2.23 \times 10^{-9})$ $PRR_g^2: -1.50 \times 10^{-6} \pm 1.6 \times 10^{-7} (P < 2 \times 10^{-16})$ $LAI_{min}: -4.30 \pm 1.24 (P = 0.00063)$
	Multiple R^2 : 0.366	Multiple R^2 : 0.435
<i>Length_{off}</i>	Equation : $Length_{off} \sim elev^2 + elev + taspect$	Equation : $Length_{off} \sim elev^2 + elev + PRR_f$
	Coefficients: $elev^2: 4.25 \times 10^{-5} \pm 5.7 \times 10^{-6} (P = 1.74 \times 10^{-12})$ $elev: -9.01 \times 10^{-2} \pm 1.24 \times 10^{-2} (P = 4.70 \times 10^{-12})$ $taspect: 1.18 \pm 0.36 (P = 0.0012)$	Coefficients: $elev^2: 4.23 \times 10^{-5} \pm 5.7 \times 10^{-6} (P = 2.50 \times 10^{-12})$ $elev: -8.94 \times 10^{-2} \pm 1.24 \times 10^{-2} (P = 7.56 \times 10^{-12})$ $PRR_f: 1.82 \times 10^{-3} \pm 5.9 \times 10^{-4} (P = 0.0021)$
	Multiple R^2 : 0.216	Multiple R^2 : 0.213

Both radiation proxies (*taspect* and seasonal *PRR*) show significant positive relationships with two senescence variables (*Mid_{off}* and *Length_{off}*), and a significant negative relationships with *Length_{on}* (Table 3.3; Figure 3.6). However, they show weak mixed effect on *Mid_{on}*, which depends on including an interaction term with *elev* (Table 3.3). An approximately 2.3-day delay in *Mid_{off}* is indicated on south-facing slopes as compared to north-facing slopes. *Length_{on}* on south-facing slopes is about 5.2 days shorter than on north-facing slopes, whereas *Length_{off}* is about 2.4 days longer. *Mid_{on}* is delayed by about 3.1 days for every unit increase in *topidx*.

Strong significant relationships between *LAI_{min}* and two mid-day phenological variables (*Mid_{on}* and *Mid_{off}*) (Table 3.3) may be attributable to mixed phenological patterns with evergreen vegetation, reflecting delayed greenup and earlier senescence. *LAI_{max}* shows a significant quadratic relation with elevation ($R^2 = 0.630$, $P < 2 \times 10^{-16}$; Figure 3.7), reflecting the strong orographic effect along elevation gradients up to 1300 m and the transition into Northern Hardwood forest which have usually brighter infrared reflectance.

3.4.2 Vegetation phenology between wet vs. dry years

Figure 3.8 presents scatter plots of six phenological variables (*Mid_{on}*, *Length_{on}*, *Mid_{off}*, *Length_{off}*, *LAI_{min}*, and *LAI_{max}*;

Table 3.1) between wet and dry years for each MODIS pixel. Overall, there is no significant difference for either mid-day variables (*Mid_{on}* and *Mid_{off}*), though greenup is occasionally delayed at wet years in mid- and high-elevation regions (Figure 3.8). Both length variables (*Length_{on}* and *Length_{off}*), however, are significantly larger in wet years than in dry years at most pixels with *Length_{off}* values exhibiting greater increases. *LAI_{max}* values for wet years are higher than those for dry years, especially in low LAI ranges, while fitted *LAI_{min}* values are similar for wet and dry years (Figure 3.8). This difference in fitted *LAI_{max}* values between wet and dry years demonstrates that

these extended transition periods during wet years are not artifacts from more cloud contamination, which can possibly reduce NDVI values and extend fitted lengths of transition periods. The shorter transition periods ($Length_{on}$ and $Length_{off}$) in dry years appears to be more related to the lower LAI_{max} values, as less soil water availability may limit leaf growth early and hasten leaf drop. This is also supported by the significant positive correlation between LAI_{max} and $Length_{on}$ at the spatial scale ($R = 0.471$; $P = 2.4 \times 10^{-15}$; Table 3.2).

Figure 3.9 shows the differences in major topography-mediated controls (*elev* and *taspect*) on two phenological length variables ($Length_{on}$ and $Length_{off}$) between wet and dry years. These controls on $Length_{on}$ and $Length_{off}$ show clear shifts between wet and dry years, while generally preserving their trends. However, there are some differences in these shift patterns. *taspect* controls show parallel shifts between wet and dry years (Figure 3.9b, d). The analysis of covariance tests for separate lines shows that the slopes of the regression lines are not significantly different between wet and dry years ($P > 0.1$), indicating that *taspect* controls on the two phenological length variables does not vary substantially with interannual variations in moisture condition. In contrast, *elev* controls on the two phenological length variables do vary substantially between wet and dry years. Though elevational controls on $Length_{on}$ show mixed signals, the differences between wet and dry years are smallest in low-elevation ranges (Figure 3.9a). The differences in $Length_{off}$ between wet and dry years are smallest in mid-elevation ranges and largest in high- and low-elevation ranges (Figure 3.9c). This means that in wet years more extended senescence periods are expected in high- and low-elevation ranges than in mid-elevation ranges.

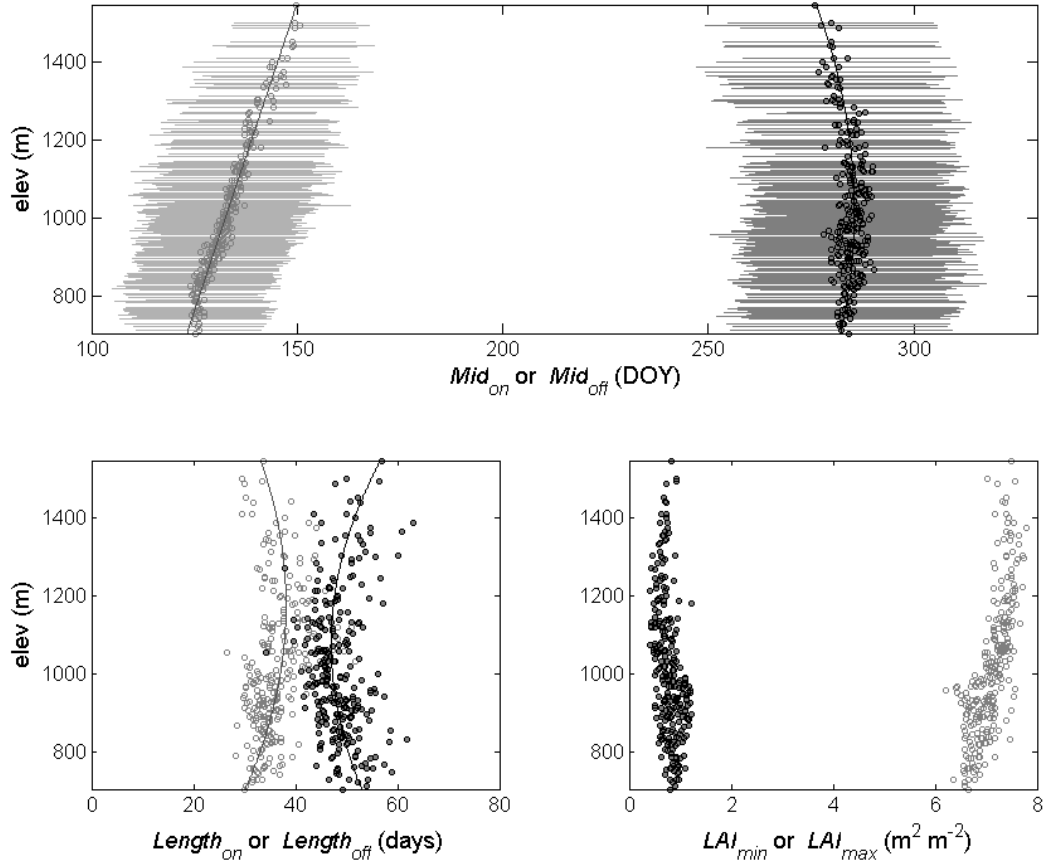


Figure 3.7: Elevational controls on (a) Mid_{on} (grey) and Mid_{off} (black), (b) $Length_{on}$ (grey) and $Length_{off}$ (black), and (c) LAI_{max} (grey) and LAI_{min} (black). Horizontal error bars represent $Length_{on}$ and $Length_{off}$.

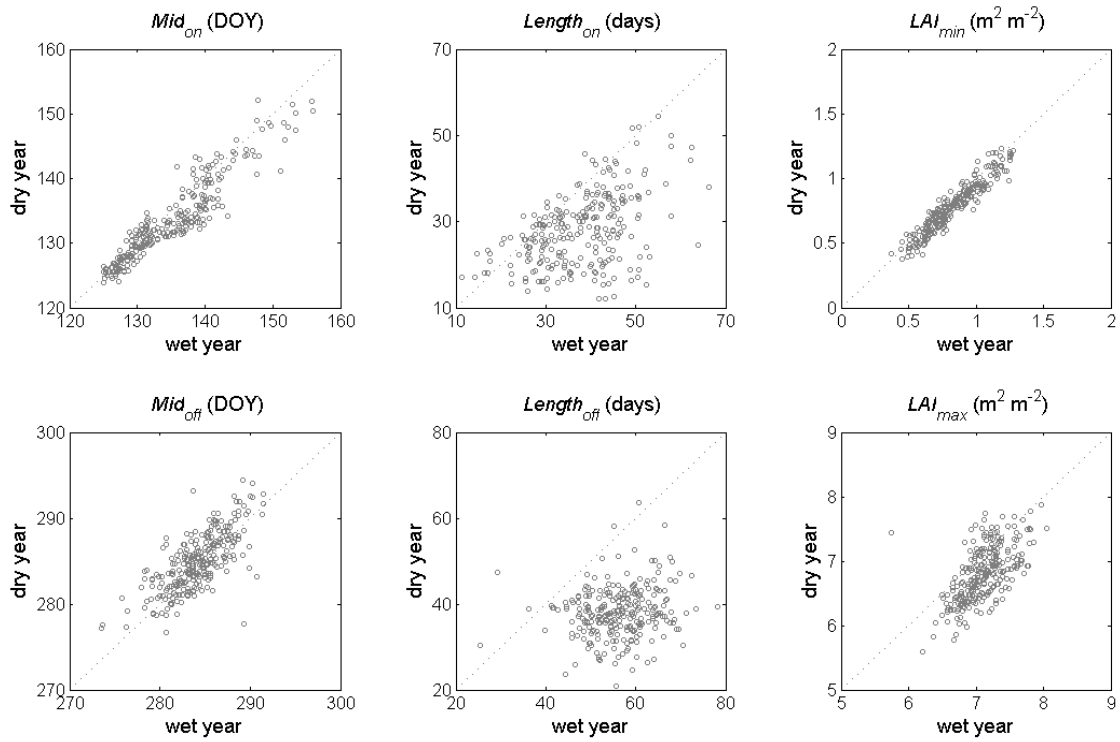


Figure 3.8: Scatter plots of six phenological variables (Mid_{on} , Mid_{off} , $Length_{off}$, $Length_{on}$, LAI_{min} , and LAI_{max}) between extremely wet (2003, 2005) and dry (2001, 2008) years.

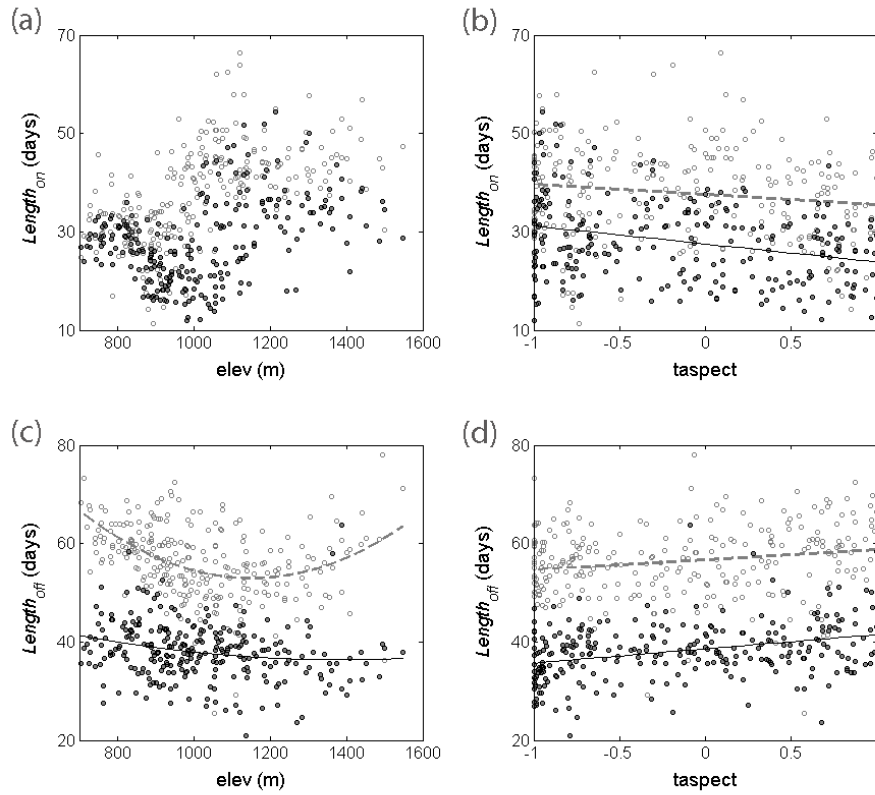


Figure 3.9: Major topographic controls (*elev*, *taspect*) on length phenological variables ($Length_{on}$, $Length_{off}$) between wet (light circles and dashed lines) and dry years (dark circles and solid line).

3.5 Discussion and conclusions

3.5.1 *Temperature controls on vegetation phenology*

This study quantifies how local vegetation phenology is mediated by topographic factors (e.g. elevation, aspect, and hillslope positions), closely related to micro-climate variations, vegetation community types, and soil water availability in the study site. In particular, elevation is a primary factor to characterize topography-mediated phenological features, associated with environmental temperature lapse rate (Bolstad *et al.* 1998) and orographic precipitation increases (Swift *et al.* 1988).

The mid-day of greenup (Mid_{on}) is a strong linear function of elevation, exactly following general empirical trends (Hopkin's law) (Hopkins 1918; Fitzjarrald *et al.* 2001). This is induced by the dominant temperature effect on on-set of spring, especially daily minimum temperature. Interestingly, the start of spring (Mid_{on}) is a little delayed with increase of the topographic wetness index ($topidx$), which can be explained by cold air drainage along hillslope gradient, not by plant water availability. Bolstad *et al.* (1998) found that temperature lapse rates decreased along local hillslope gradients in this study region, which was attributed to cold air drainage downslope formed by radiative cooling during still nights (Mahrt *et al.* 2001; Soler *et al.* 2002). Bolstad *et al.* (1998) also found that reduced lapse rates are most pronounced during the early spring, a period critical to on-set phenological timing, and lapse rates for minimum temperature are negative throughout the year because cold air drainage is predominant at night-time. Many studies show that minimum (or suboptimal) temperature is a stronger constraint on vegetation phenology across various ecosystems (e.g. Jolly *et al.* 2005; Larcher and Bauer 1981; Jarvis and Linder 2000). Fisher *et al.* (2006) also reported a significant impact of cold air drainage on greenup phenology, a strong negative correlation between elevation and on-set date along four elevational transects in New England.

It is also possible that transitions to cove hardwoods species (e.g. *L. tulipifera*, *T. canadensis* and *A. rubrum* etc.) in cove regions (Figure 3.2; Day *et al.* 1988) lead to unique sensitivity of greenup phenological variable to the *topidx* variable. However, observed phenology of five major deciduous species in the study area reported that there was no significant difference in greenup timing between these species (Day and Monk 1977). *T. canadensis* (eastern hemlock), one of the principal riparian and cove species, may have unique phenological patterns compared to broadleaf deciduous species. However, it is facing recent severe extirpation by the introduced insect (hemlock woolly adelgid) (Ford and Vose 2007), so it may have limited effect on recently observed phenological signals in this study.

3.5.2 Photoperiod controls on vegetation phenology

Radiation proxies (*taspect* and *PRRs*) are also significant for all phenological variables (Table 3.3; Figure 3.6), which may be related to photoperiod, temperature, and water stress. Many studies have shown that photoperiod plays an important role in both greenup and senescence vegetation phenology across different ecosystems (e.g. White *et al.* 1997; Partanen *et al.* 1998; Hanninen 1990; Hakkinen *et al.* 1998). Radiation proxies have positive relationships with two senescence phenological variables (*Mid_{off}* and *Length_{off}*) in this study, while a negative relationship with *Length_{on}*. However, they show weak mixed effect on *Mid_{on}* depending on including the interaction term with *elev* (Table 3.3). Note that *taspect* controls on length phenological variables (*Length_{on}* and *Length_{off}*) between wet and dry years are consistent (Figure 3.9), which possibly involves photoperiod controls on vegetation phenology. In addition, radiation proxies have more explanatory power for senescence timing (*Mid_{off}*) than greenup timing (*Mid_{on}*).

Elongated photoperiods on south-facing slopes can delay *Mid_{off}* and lengthen *Length_{off}*. There have also been some studies that the cessation of vegetation growth stage is closely related to photoperiod (Zhang *et al.* 2004; Junttila 1980; Hanninen *et al.* 1990; Schwartz 1990). Even

though there is no common agreement on an appropriate model structure for leaf senescence (Schaber and Badeck 2003), some studies reviewed more dominant roles of photoperiod on senescence (or dormancy onset) than greenup phenology (greenup onset or dormancy release) for cool and temperate woody plants (White *et al.* 1997, 2002; Wareing 1956; Lee *et al.* 2003).

However, shorter $Length_{on}$ are also observed on south-facing slopes, which is hard to explain with photoperiod alone. We found that longer $Length_{on}$ may correspond to higher vegetation density (LAI_{max}) both along elevation gradients (Figure 3.7) and interannually (Figure 3.8). However, multiple regression analysis (not shown here) show that radiation proxies are not significant for LAI_{max} ($P > 0.1$; not shown here), which implies that shorter $Length_{on}$ on south-facing slopes are not related to lower vegetation density. In addition, radiation proxies also show weak negative relationships with Mid_{on} if the interaction terms with $elev$ are included for both models (Table 3.3). They may represent faster growth of vegetation by combined effect of photoperiod and temperature, but more limited growth or belowground allocation by water stress on south-facing slopes.

In this study, radiation proxies are more significant for $Length_{on}$ than for Mid_{on} (Table 3.3). This result implies that radiation proxies are more related to photoperiod and photosynthetically active radiation (PAR) (or daily temperature amplitude) than to minimum temperature, which is more important for Mid_{on} . There are some disagreements as to whether the timing of growth onset is regulated solely by temperature (Partanen *et al.* 1998; Richardson *et al.* 2006; Chuine *et al.* 1999). Interactions between photoperiod and temperature may limit foliar phenology. As an example, bud-burst may not be triggered by temperature without corresponding photoperiod changes especially in high-latitude regions (Partanen *et al.* 1998; Hakkinen *et al.* 1998; Heide 1993). However, many studies in deciduous forests also reported that a large portion of the spatial and interannual variations in spring canopy development are explained by temperature alone (Jenkins *et al.* 2002; Richardson *et al.* 2006; Chuine and Cour 1999).

3.5.3 Other controls on vegetation phenology

Temperature effects alone cannot explain the quadratic responses of the three phenological variables (Mid_{off} , $Length_{on}$, and $Length_{off}$) to elevation (Figure 3.7), which could be explained by combined effects with orographic precipitation patterns (Swift *et al.* 1988). Delayed senescence in the mid-elevation region is related to higher water availability and vegetation density following orographic precipitation increases with elevation (Figure 3.7). Fitted maximum LAI values (LAI_{max}) show this increased vegetation density along elevational gradients up to 1200 m, correlated not only to increased water availability but also to increased wet deposition of nitrogen following precipitation (Knoepp *et al.* 2008). The increase of LAI_{max} is possibly from the increase of NDVI by the transition into Northern Hardwood forest at higher elevation, which has usually brighter infrared reflectance. Higher vegetation density (LAI_{max}) is also relevant to longer greenup period ($Length_{on}$) at mid-elevation regions, represented by a significant positive correlation at the MODIS spatial scale (Table 3.2).

The comparison of LAI_{max} between wet and dry years shows that water availability is a more limiting factor at lower elevation regions (Figure 3.8). Greater increases of LAI_{max} in wet years are found in lower LAI_{max} ranges, usually developed at lower elevation regions (Figure 3.7). Also, elevational controls on $Length_{off}$ between wet and dry years show higher increases in lower elevation regions (Figure 3.9c). Vegetation in lower elevation regions is more sensitive to precipitation than mid-elevation regions, as water (or nitrogen) is a more limiting factor for their growth.

Temperature is still a dominant factor for other phenological variables in high elevation regions, represented as early litterfall, shorter greenup period, and longer senescence period. Combined effects of temperature and orographic precipitation show distinct quadratic responses of three phenological variables as a function of elevation, also moderated by forest community types. Note that high elevation regions are regarded as transition zones from Southern Appalachian to Northern

Hardwoods forest (Figure 3.2), which has different phenological responses to climate factors (Fisher *et al.* 2007). These patterns also relate to different limiting factors of vegetation growth along elevational gradients, water or nitrogen limited at lower elevation regions and temperature limited at higher elevation regions (Knoepp and Swank 1998; Knoepp *et al.* 2008).

Strong significance of LAI_{min} to two mid-day phenological variables effectively represents the effect of coniferous and understory evergreen species on vegetation phenology (Table 3.3), which is characterized as more delayed greenup and earlier senescence with higher LAI_{min} . Seasonal dynamics of pine LAI in this study site show typical sinusoidal patterns (Vose and Swank 1990; Vose *et al.* 1994), which may reduce the length of a growing season at both ends. In addition, early development of understory broadleaf may not be detected well by the sensor due to overstory evergreen vegetation in low NDVI ranges. This may also result in delayed greenup and early senescence in averaged phenological signals within a MODIS pixel.

3.5.4 Growing season length (GSL) vs. vegetation growth

Growing season length (GSL) is usually defined as the length between greenup onset and dormancy onset (Churkina *et al.* 2005; Chen *et al.* 1999b). In this study, interannual variations of GSL between wet and dry years show a possible correlation of GSL with vegetation growth (Figure 3.8). Earlier greenup and extended senescence periods were observed in wet years (Figure 3.8). Extended GSL is also associated with higher vegetation growth (maximum LAI), known to be tightly coupled with net ecosystem production (e.g. Barr *et al.* 2004). However, this correlation between GSL and vegetation growth depends on how GSL is defined from LAI trajectories. If GSL is defined as the length between Mid_{on} and Mid_{off} (White *et al.* 1999), there is not much difference of GSL between wet and dry years (Figure 3.8).

Many studies point out a major role of GSL in the terrestrial carbon cycle (Keeling *et al.* 1996; Myneni *et al.* 1997; Randerson *et al.* 1999; White *et al.* 1999; Chen *et al.* 1999b; Black *et al.*

2000; Churkina *et al.* 2005). However, recent studies also reviewed the possibility that more soil water depletion could cancel out early spring carbon assimilation by enhancing summer drought (White and Nemani 2003; Angert *et al.* 2005). From multi-year flux tower measurements, leaf phenology is known to be strongly correlated with annual net ecosystem production in temperate and boreal forests (Goulden *et al.* 1996; Baldocchi *et al.* 2001; White and Nemani 2003; Barr *et al.* 2004).

Most studies of the relationship between GSL and carbon uptake by vegetation have focused on early greenup onset driven by increased temperature and its impact on atmospheric CO₂ amplitudes and carbon uptake by vegetation. They usually report that there was no significant extension of growing season during the fall despite early greenup (Myneni *et al.* 1997; Randerson *et al.* 1999; Chen *et al.* 1999b; Black *et al.* 2000; Barr *et al.* 2004). However, this study shows that GSL can be extended at both growth and senescence ends in extremely wet years compared to extremely dry years, possibly related to higher vegetation growth (LAI_{max}) and more carbon uptake by vegetation. A dominant role of seasonal rainfall or soil water stress on vegetation phenology has usually been reported for most drought-deciduous species in tropics and semi-arid areas (Nilsen and Muller 1981; Childs 1988; Borchert 1994; Botta *et al.* 2000; Bach 2002; Jolly and Running 2004), where greenup is initiated by the first large precipitation event, and senescence is more slowly modulated by available soil water. In the Piedmont area, Pataki and Oren (2003) found that early autumn leaf senescence and abscission is the primary effect of severe drought rather than stress-driven stomatal closure from sap flux measurements of six common deciduous species in eastern oak-hickory forest during severe drought.

Note that we could not find any significant positive correlation between GSL and LAI_{max} at the MODIS spatial scale. Some studies reported inter-site positive correlations between GSL and net ecosystem production (White *et al.* 1999; Baldocchi *et al.* 2001; Churkina *et al.* 2005). However,

we found a significant correlation between $Length_{on}$ and LAI_{max} at local patterns of topography-mediated vegetation phenology (Table 3.2).

3.5.5 *Spatial scale issues*

In this study, sub-grid variability of topographic variables, especially *taspect* and *topidx*, suggests important scale issues in the relationship between topographic and phenological variables. The hillslope position (*topidx*) seems significant only for the Mid_{on} variables, which can be explained by cold air drainage rather than soil water availability. The insignificance of *topidx* to senescence phenological variables may be attributed to the transition of vegetation community types into cove hardwood species, for which phenological features may be constrained by other factors (e.g. light) rather than soil water availability. However, we found strong precipitation-related controls on phenological variables in terms of both orographic and interannual variations. Therefore, sub-grid variability can be a more reasonable explanation for the insensitivity of vegetation senescence as a function of hillslope position. Averaged *topidx* ranges at the MODIS scale are from 4 to 5.5 (Figure 3.6), not enough to examine full controls of soil water on phenological features at finer scales. Interestingly, cold air drainage effects on greenup vegetation phenology came out in this study because cold air drainage may show broader flowpath patterns than water along hillslope gradient at the MODIS scale. Note that *topidx* at MODIS scale was calculated from aggregating values from the original DEM scale, while radiation proxies were calculated from degraded DEM to MODIS scale.

Micro-topography can be lost when aspect and *PRRs* are calculated at the MODIS scale. Contrary to elevation, very diverse sub-grid distributions of aspect and *PRRs* are expected within a single MODIS pixel, so it is possible that phenological responses to these radiation proxies are more exaggerated at finer scale. Comparisons of radiation proxies between two different upscaling methods would clarify this point. Figure 3.10 shows scatter plots between radiation proxies at each

MODIS pixel from two different upscaling methods. Radiation proxies on the x-axis are calculated from upscaled DEM, while those on the y-axis from aggregating radiation proxies at the original DEM scale. They show some reasonable correlations, but different patterns between them.

As for *taspect*, we have narrower ranges when they are aggregated from the original DEM (Figure 3.10). The pixel classified as south-facing at MODIS scale can have diverse aspects in the level of sub-grid variability. Note that *taspect* is a relative term between -1 and 1 to represent radiation potentials at each pixel. However, PRR_g values from upscaled DEM show narrower ranges than those aggregated from the original DEM (Figure 3.10). It is mainly because the coarse DEM simplifies topography and reduces slope, so it may lose some micro-topographic features which usually decreases the heterogeneity of incident radiation.

This scaling issue implies that phenological responses to radiation proxies described in this study show reduced gradients compared to actual vegetation responses by filtering their signals and topographic variables at the MODIS scale. Previous studies have also shown that aggregating topographic variables into a coarse resolution (e.g. AVHRR, MODIS) can significantly reduce variations in these variables and resulting LAI values (e.g. Band *et al.* 1991; Band 1993; Band and Moore 1995).

Continuous field measurements of optical LAI at six different locations in this study site (unpublished data from Dr James Vose), apparently supports reduced phenological responses at coarser resolution, especially in terms of radiation proxies. Temporal patterns of LAI were previously measured at six different locations represented as high-, mid-, low-elevation and south-, north-facing slopes within the study site throughout the year. Very similar relationships between topographical factors and vegetation phenological patterns were found in the field measurements. In terms of greenup timing, elevation was a dominant factor, whereas both elevation and aspect were crucial for senescence timing. Estimated Mid_{on} and Mid_{off} in this study, largely corresponded with

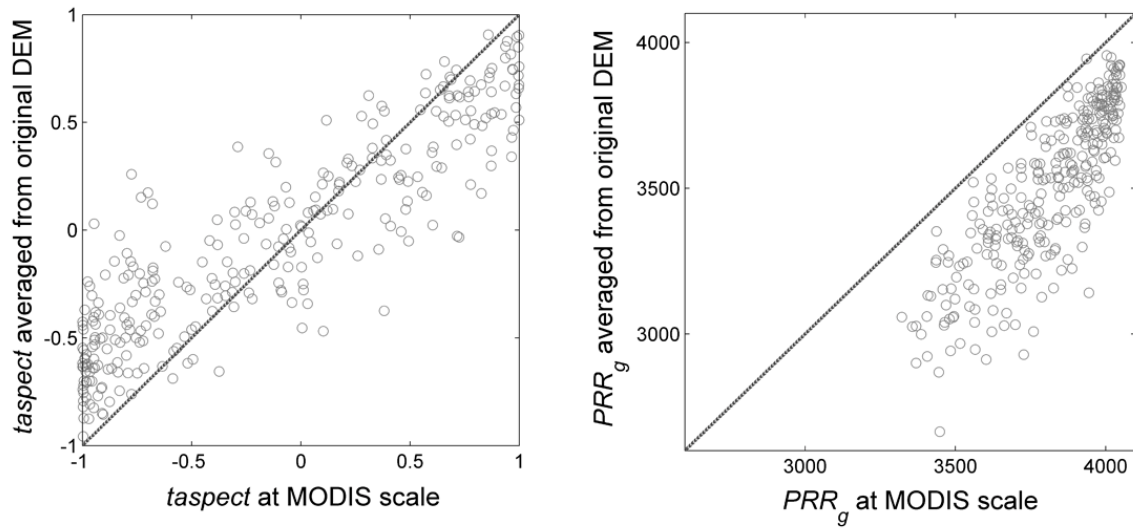


Figure 3.10: Comparison of radiation proxies (*taspect*, PRR_g) from two different upscaling methods at each MODIS pixels. Radiation proxies of x-axis were calculated from upscaled DEM at MODIS scale (about 250 m), while those of y-axis from averaging of the original scale radiation proxies from LIDAR DEM (about 6 m).

those from field measurements. However, field measurements between south and north facing slopes exhibited more than a 3-day differences in Mid_{off} , estimated in this study. The scale variance nature of both qualitative and quantitative radiation proxies (Figure 3.10) makes it hard to find a consistent relationship with phenological variables.

3.5.6 Conclusions

In this study, we extract phenological signals from 8-year MODIS NDVI (2001 ~ 2008) with a two-step filtering and non-linear fitting method within the Coweeta LTER site. These phenological signals are related to topographic variables, such as elevation, aspect, potential relative radiation, and wetness index, by multiple regression analysis. Elevation shows strong linear or quadratic relationships with four phenological variables. Quadratic responses of three phenological variables (Mid_{off} , $Length_{on}$, and $Length_{off}$) with elevation are explained by combined effects of temperature and precipitation along the elevation gradient. Radiation proxies ($taspect$ and $PRRs$) also have explanatory power for phenological variables, associated with photoperiod controls on vegetation phenology. Hillslope positions ($topidx$) show significant effects on the Mid_{on} phenological variables, possibly related to decreased temperature lapse rates along local hillslope gradients by cold air drainage downslope. Though topographic wetness position was not observed to have a significant effect on vegetation phenology from MODIS NDVI, the difference of vegetation phenology between extremely wet and dry years reveals possible extended growing season length in wet years. These topography-mediated phenological patterns are strongly supported by field measurements at different topographic positions within the study site. However, phenological responses to radiation proxies might be mitigated due to the scale variance nature of both radiation proxies between fine and coarse resolutions.

In conclusion, topography-mediated controls on local vegetation phenology are closely related to the combined effect of micro-climate variations, vegetation community types, and hydrological

positions. The capability of detecting the topography-mediated local phenology offers the potential to detect vegetation responses to future global climate change in mountainous terrains.

Acknowledgements

We specifically thank Dr. Jim Vose for providing valuable field measurements of vegetation phenology. This research was supported by the National Science Foundation award to the Coweeta Long Term Ecologic Research project (DEB #0823293). This paper is co-authored by Dr. L. E. Band and Dr. C. Song. Dr. L. E. Band provided overall directions to this research study as a dissertation advisor and gave insights toward data analysis and interpretation. This paper is co-authored by Dr Lawrence E. Band and Dr. Conghe Song. Dr. L. E. Band provided overall directions to this research study as a dissertation advisor and gave insights toward data analysis and interpretation. Dr. C. Song was involved in the analysis of MODIS data and discussions of interpreting the data.

Appendix

The fourth derivative of the logistic function (Eq. 3.2) is solved as

$$\frac{d^4 y}{dt^4} = \frac{24b^4 ce^{4(a+bt)}}{(1+e^{a+bt})^5} - \frac{36b^4 ce^{3(a+bt)}}{(1+e^{a+bt})^4} + \frac{14b^4 ce^{2(a+bt)}}{(1+e^{a+bt})^3} - \frac{b^4 ce^{a+bt}}{(1+e^{a+bt})^2}$$

If we substitute $e^{a+bt} = x$ and rearrange this equation

$$\frac{d^4 y}{dt^4} = \frac{b^4 cx \{24x^3 - 36x^2(1+x) + 14x(1+x)^2 - (1+x)^3\}}{(1+x)^5} = \frac{b^4 cx(x^3 - 11x^2 + 11x - 1)}{(1+x)^5}$$

Then, this equation can be factorized as

$$\frac{d^4 y}{dt^4} = \frac{b^4 cx \{(x-1)(x^2 + x + 1) - 11x(x-1)\}}{(1+x)^5} = \frac{b^4 cx(x-1)(x^2 - 10x + 1)}{(1+x)^5}$$

We can get local minima and maxima values of the third derivative of the logistic function (Figure 3.5d) by setting the above equation to zero. Note that x cannot be zero.

$$x = 1 \text{ or } x^2 - 10x + 1 = 0$$

where the first ($x = 1$) represents the middle minima or maxima values and the latter ($x^2 - 10x + 1 = 0$) represents both side maxima or minima values (Figure 3.5d). From the quadratic formula, we can get this solution as

$$x = 5 \pm 2\sqrt{6}$$

If x is resubstituted by t , we can get final solutions for transition dates.

$$t' = \frac{\ln(5 \pm 2\sqrt{6}) - a}{b}$$

References

- Ahl DE, Gower ST, Burrows SN, Shabanov NV, Myneni RB, Knyazikhin Y (2006) Monitoring spring canopy phenology of a deciduous broadleaf forest using MODIS. *Remote Sensing of Environment*, **104**, 88-95.
- Angert A, Biraud S, Bonfils C, Henning CC, Buermann W, Pinzon J, Tucker CJ, Fung I (2005) Drier summers cancel out the CO₂ uptake enhancement induced by warmer springs. *Proceedings of the National Academy of Sciences of the United States of America*, **102**, 10823-10827.
- Arora VK, Boer GJ (2005) A parameterization of leaf phenology for the terrestrial ecosystem component of climate models. *Global Change Biology*, **11**, 39-59.
- Bach CS (2002) Phenological patterns in monsoon rainforests in the Northern Territory, Australia. *Austral Ecology*, **27**, 477-489.
- Baldocchi D, Falge E, Gu LH, et al (2001) FLUXNET: A new tool to study the temporal and spatial variability of ecosystem-scale carbon dioxide, water vapor, and energy flux densities. *Bulletin of the American Meteorological Society*, **82**, 2415-2434.
- Band LE (1993) Effect of Land-Surface Representation on Forest Water and Carbon Budgets. *Journal of Hydrology*, **150**, 749-772.
- Band LE, Moore ID (1995) Scale - Landscape Attributes and Geographical Information-Systems. *Hydrological Processes*, **9**, 401-422.
- Barr AG, Black TA, Hogg EH, Kljun N, Morgenstern K, Nesic Z (2004) Inter-annual variability in the leaf area index of a boreal aspen-hazelnut forest in relation to net ecosystem production. *Agricultural and Forest Meteorology*, **126**, 237-255.
- Beck PSA, Atzberger C, Hogda KA, Johansen B, Skidmore AK (2006) Improved monitoring of vegetation dynamics at very high latitudes: A new method using MODIS NDVI. *Remote Sensing of Environment*, **100**, 321-334.
- Beers TW, Dress PE, Wensel LC (1966) Aspect Transformation in Site Productivity Research. *Journal of Forestry*, **64**, 691-692.
- Beven K, Kirkby M (1979) A physically-based variable contributing area model of basin hydrology. *Hydrologic Science Bulletin*, **24**, 43-69.
- Black TA, Chen WJ, Barr AG, et al (2000) Increased carbon sequestration by a boreal deciduous forest in years with a warm spring. *Geophysical Research Letters*, **27**, 1271-1274.

- Bolstad PV, Swift L, Collins F, Regniere J (1998) Measured and predicted air temperatures at basin to regional scales in the southern Appalachian mountains. *Agricultural and Forest Meteorology*, **91**, 161-176.
- Borchert R (1994) Soil and Stem Water Storage Determine Phenology and Distribution of Tropical Dry Forest Trees. *Ecology*, **75**, 1437-1449.
- Botta A, Viovy N, Ciais P, Friedlingstein P, Monfray P (2000) A global prognostic scheme of leaf onset using satellite data. *Global Change Biology*, **6**, 709-725.
- Bradley BA, Jacob RW, Hermance JF, Mustard JF (2007) A curve fitting procedure to derive inter-annual phenologies from time series of noisy satellite NDVI data. *Remote Sensing of Environment*, **106**, 137-145.
- Chen J, Jonsson P, Tamura M, Gu ZH, Matsushita B, Eklundh L (2004) A simple method for reconstructing a high-quality NDVI time-series data set based on the Savitzky-Golay filter. *Remote Sensing of Environment*, **91**, 332-344.
- Chen WJ, Black TA, Yang PC, et al (1999) Effects of climatic variability on the annual carbon sequestration by a boreal aspen forest. *Global Change Biology*, **5**, 41-53.
- Childes SL (1988) Phenology of Nine Common Woody Species in Semi-Arid Deciduous Kalahari Sand South Africa Vegetation. *Vegetatio*, **79**, 151-164.
- Chuine I, Cambon G, Comtois P (2000) Scaling phenology from the local to the regional level: advances from species-specific phenological models. *Global Change Biology*, **6**, 943-952.
- Chuine I, Cour P (1999) Climatic determinants of budburst seasonality in four temperate-zone tree species. *New Phytologist*, **143**, 339-349.
- Chuine I, Cour P, Rousseau DD (1999) Selecting models to predict the timing of flowering of temperate trees: implications for tree phenology modelling. *Plant Cell and Environment*, **22**, 1-13.
- Churkina G, Schimel D, Braswell BH, Xiao XM (2005) Spatial analysis of growing season length control over net ecosystem exchange. *Global Change Biology*, **11**, 1777-1787.
- Crawley MJ (2007) *The R Book*. John Wiley & Sons Inc., Hoboken, NJ, USA.
- Day FP, Philips DL, Monk CD (1988) Forest communities and patterns. In: *Forest Hydrology and Ecology at Coweeta* (eds Swank WT, Crossley JDA), pp. 141-149. Springer-Verlag, New York, NY, USA.
- Day FP, Monk CD (1977) Net Primary Production and Phenology on a Southern Appalachian Watershed. *American Journal of Botany*, **64**, 1117-1125.

- Day FP, Monk CD (1974) Vegetation Patterns on a Southern Appalachian Watershed. *Ecology*, **55**, 1064-1074.
- Didan K, Huete A (2006) MODIS Vegetation Index Product Series Collection 5 Change Summary.
- Fisher JJ, Mustard JF (2007) Cross-scalar satellite phenology from ground, Landsat, and MODIS data. *Remote Sensing of Environment*, **109**, 261-273.
- Fisher JJ, Mustard JF, Vadeboncoeur MA (2006) Green leaf phenology at Landsat resolution: Scaling from the field to the satellite. *Remote Sensing of Environment*, **100**, 265-279.
- Fisher JJ, Richardson AD, Mustard JF (2007) Phenology model from surface meteorology does not capture satellite-based greenup estimations. *Global Change Biology*, **13**, 707-721.
- Fitzjarrald DR, Acevedo OC, Moore KE (2001) Climatic consequences of leaf presence in the eastern United States. *Journal of Climate*, **14**, 598-614.
- Ford CR, Vose JM (2007) *Tsuga canadensis* (L.) Carr. mortality will impact hydrologic processes in southern appalachian forest ecosystems. *Ecological Applications*, **17**, 1156-1167.
- Goulden ML, Munger JW, Fan SM, Daube BC, Wofsy SC (1996) Exchange of carbon dioxide by a deciduous forest: Response to interannual climate variability. *Science*, **271**, 1576-1578.
- Goward SN, Markham B, Dye DG, Dulaney W, Yang JL (1991) Normalized Difference Vegetation Index Measurements from the Advanced very High-Resolution Radiometer. *Remote Sensing of Environment*, **35**, 257-277.
- Hakkinen R, Linkosalo T, Hari P (1998) Effects of dormancy and environmental factors on timing of bud burst in *Betula pendula*. *Tree physiology*, **18**, 707-712.
- Hanninen H (1990) Modelling Bud Dormancy Release in Trees from Cool and Temperate Regions. *Acta Forestalia Fennica*, **213**, 1-47.
- Hanninen H, Hakkinen R, Hari P, Koski V (1990) Timing of Growth Cessation in Relation to Climatic Adaptation of Northern Woody-Plants. *Tree physiology*, **6**, 29-39.
- Heide OM (1993) Dormancy Release in Beech Buds (*Fagus-Sylvatica*) Requires both Chilling and Long Days. *Physiologia Plantarum*, **89**, 187-191.
- Heinsch FA, Reeves M, Votava P, et al (2003) User's Guide, GPP and NPP (MOD17A2/A3) Products, NASA MODIS Land Algorithm.
- Hopkins AD (1918) Periodical events and natural law as guides to agricultural research and practice. *Monthly Weather Review*, **9 (Suppl.)**, 1-42.

- Huete A, Didan K, Miura T, Rodriguez EP, Gao X, Ferreira LG (2002) Overview of the radiometric and biophysical performance of the MODIS vegetation indices. *Remote Sensing of Environment*, **83**, 195-213.
- Huete A, Justice C, Liu H (1994) Development of Vegetation and Soil Indexes for Modis-Eos. *Remote Sensing of Environment*, **49**, 224-234.
- Huete AR (1988) A Soil-Adjusted Vegetation Index (Savi). *Remote Sensing of Environment*, **25**, 295-309.
- Huntington TG (2004) Climate change, growing season length, and transpiration: Plant response could alter hydrologic regime. *Plant Biology*, **6**, 651-653.
- Jarvis P, Linder S (2000) Constraints to growth of boreal forests. *Nature*, **405**, 904-905.
- Jenkins JP, Braswell BH, Frolking SE, Aber JD (2002) Detecting and predicting spatial and interannual patterns of temperate forest springtime phenology in the eastern U.S. *Geophysical Research Letters*, **29**, 54-1-4.
- Jolly WM, Nemani R, Running SW (2005) A generalized, bioclimatic index to predict foliar phenology in response to climate. *Global Change Biology*, **11**, 619-632.
- Jolly WM, Running SW (2004) Effects of precipitation and soil water potential on drought deciduous phenology in the Kalahari. *Global Change Biology*, **10**, 303-308.
- Jonsson P, Eklundh L (2002) Seasonality extraction by function fitting to time-series of satellite sensor data. *IEEE Transactions on Geoscience and Remote Sensing*, **40**, 1824-1832.
- Junttila O (1980) Effect of photoperiod and temperature on apical growth cessation in two ecotypes of *Salix* and *Betula*. *Physiologia Plantarum*, **48**, 347-352.
- Justice CO, Vermote E, Townshend JRG, et al (1998) The Moderate Resolution Imaging Spectroradiometer (MODIS): Land remote sensing for global change research. *IEEE Transactions on Geoscience and Remote Sensing*, **36**, 1228-1249.
- Kang S, Running SW, Lim JH, Zhao MS, Park CR, Loehman R (2003) A regional phenology model for detecting onset of greenness in temperate mixed forests, Korea: an application of MODIS leaf area index. *Remote Sensing of Environment*, **86**, 232-242.
- Keeling CD, Chin JFS, Whorf TP (1996) Increased activity of northern vegetation inferred from atmospheric CO₂ measurements. *Nature*, **382**, 146-149.
- Knoepp JD, Swank WT (1998) Rates of nitrogen mineralization across an elevation and vegetation gradient in the southern Appalachians. *Plant and Soil*, **204**, 235-241.

- Knoepp JD, Vose JM, Swank WT (2008) Nitrogen deposition and cycling across an elevation and vegetation gradient in southern Appalachian forests. *International Journal of Environmental Studies*, **65**, 389-408.
- Larcher W, Bauer H (1981) Ecological significance of resistance to low temperature. In: *Encyclopedia of Plant Physiology* (eds Lange OL, Nobel PS, Osmond CB, Ziegler H), pp. 403-437. Springer-Verlag, Berlin, German.
- Lee DW, O'Keefe J, Holbrook NM, Feild TS (2003) Pigment dynamics and autumn leaf senescence in a New England deciduous forest, eastern USA. *Ecological Research*, **18**, 677-694.
- Lovell JL, Graetz RD (2001) Filtering pathfinder AVHRR land NDVI data for Australia. *International Journal of Remote Sensing*, **22**, 2649-2654.
- Ma M, Veroustraete F (2006) Reconstructing pathfinder AVHRR land NDVI time-series data for the Northwest of China. *Advances in Space Research*, **37**, 835-840.
- Mahrt L, Vickers D, Nakamura R, Soler MR, Sun JL, Burns S, Lenschow DH (2001) Shallow drainage flows. *Boundary-Layer Meteorology*, **101**, 243-260.
- Matsumoto K, Ohta T, Irasawa M, Nakamura T (2003) Climate change and extension of the Ginkgo biloba L. growing season in Japan. *Global Change Biology*, **9**, 1634-1642.
- Menzel A, Fabian P (1999) Growing season extended in Europe. *Nature*, **397**, 659-659.
- Myneni RB, Hoffman S, Knyazikhin Y, et al (2002) Global products of vegetation leaf area and fraction absorbed PAR from year one of MODIS data. *Remote Sensing of Environment*, **83**, 214-231.
- Myneni RB, Keeling CD, Tucker CJ, Asrar G, Nemani RR (1997) Increased plant growth in the northern high latitudes from 1981 to 1991. *Nature*, **386**, 698-702.
- Nemani R, Pierce L, Running S, Band L (1993) Forest Ecosystem Processes at the Watershed Scale: Sensitivity to Remotely-Sensed Leaf Area Index Estimates. *International Journal of Remote Sensing*, **14**, 2519-2534.
- Nilsen ET, Muller WH (1981) Phenology of the Drought-Deciduous Shrub Lotus-Scoparius - Climatic Controls and Adaptive Significance. *Ecological Monographs*, **51**, 323-341.
- Obrist D, Verburg PSJ, Young MH, Coleman JS, Schorran DE, Arnone JA (2003) Quantifying the effects of phenology on ecosystem evapotranspiration in planted grassland mesocosms using EcoCELL technology. *Agricultural and Forest Meteorology*, **118**, 173-183.
- Olsson L, Eklundh L (1994) Fourier-Series for Analysis of Temporal Sequences of Satellite Sensor Imagery. *International Journal of Remote Sensing*, **15**, 3735-3741.

- Palmer WC (1965) *Meteorological Drought. Report Number 45*, U.S. Weather Bureau, Washington DC, USA.
- Partanen J, Koski V, Hanninen H (1998) Effects of photoperiod and temperature on the timing of bud burst in Norway spruce (*Picea abies*). *Tree physiology*, **18**, 811-816.
- Pataki DE, Oren R (2003) Species differences in stomatal control of water loss at the canopy scale in a mature bottomland deciduous forest. *Advances in Water Resources*, **26**, 1267-1278.
- Pierce KB, Lookingbill T, Urban D (2005) A simple method for estimating potential relative radiation (PRR) for landscape-scale vegetation analysis. *Landscape Ecology*, **20**, 137-147.
- Randerson JT, Field CB, Fung IY, Tans PP (1999) Increases in early season ecosystem uptake explain recent changes in the seasonal cycle of atmospheric CO₂ at high northern latitudes. *Geophysical Research Letters*, **26**, 2765-2768.
- Reichstein M, Ciais P, Papale D, et al (2007) Reduction of ecosystem productivity and respiration during the European summer 2003 climate anomaly: a joint flux tower, remote sensing and modelling analysis. *Global Change Biology*, **13**, 634-651.
- Richardson AD, Bailey AS, Denny EG, Martin CW, O'Keefe J (2006) Phenology of a northern hardwood forest canopy. *Global Change Biology*, **12**, 1174-1188.
- Roerink GJ, Menenti M, Verhoef W (2000) Reconstructing cloudfree NDVI composites using Fourier analysis of time series. *International Journal of Remote Sensing*, **21**, 1911-1917.
- Running SW, Thornton PE, Nemani R, Glassy JM (2000) Global terrestrial gross and net primary productivity from the earth observing system. In: *Methods in Ecosystem Science* (eds Sala OE, Jackson RB, Mooney HA, Howarth RW), pp. 44-57. Springer-Verlag, New York.
- Running SW, Nemani RR (1991) Regional Hydrologic and Carbon Balance Responses of Forests Resulting from Potential Climate Change. *Climatic Change*, **19**, 349-368.
- Sakamoto T, Yokozawa M, Toritani H, Shibayama M, Ishitsuka N, Ohno H (2005) A crop phenology detection method using time-series MODIS data. *Remote Sensing of Environment*, **96**, 366-374.
- Schaber J, Badeck FW (2003) Physiology-based phenology models for forest tree species in Germany. *International journal of biometeorology*, **47**, 193-201.
- Schwartz MD (1990) Detecting the Onset of Spring a Possible Application of Phenological Models. *Climate Research*, **1**, 23-30.
- Schwartz MD, Reed BC, White MA (2002) Assessing satellite-derived start-of-season measures in the conterminous USA. *International Journal of Climatology*, **22**, 1793-1805.
- Seber GAF, Wild CJ (1989) *Nonlinear Regression*. John Wiley & Sons Inc., Canada.

- Seghieri J, Simier M (2002) Variations in phenology of a residual invasive shrub species in Sahelian fallow savannas, south-west Niger. *Journal of Tropical Ecology*, **18**, 897-912.
- Soler MR, Infante C, Buenestado P, Mahrt L (2002) Observations of nocturnal drainage flow in a shallow gully. *Boundary-Layer Meteorology*, **105**, 253-273.
- Swift LW, Cunningham J, G.B., Douglass JE (1988) Climatology and hydrology. In: *Forest Hydrology and Ecology at Coweeta* (eds Swank WT, Crossley JDA), pp. 35-55. Springer-Verlag, New York, NY, USA.
- Tarboton DG (1997) A new method for the determination of flow directions and upslope areas in grid digital elevation models. *Water Resources Research*, **33**, 309-319.
- Tateno R, Aikawa T, Takeda H (2005) Leaf-fall phenology along a topography-mediated environmental gradient in a cool-temperate deciduous broad-leaved forest in Japan. *Journal of Forest Research*, **10**, 269-274.
- Verhoef W, Menenti M, Azzali S (1996) A colour composite of NOAA-AVHRR-NDVI based on time series analysis (1981-1992). *International Journal of Remote Sensing*, **17**, 231-235.
- Viovy N, Arino O, Belward AS (1992) The Best Index Slope Extraction (BISE) - a Method for Reducing Noise in NDVI Time-Series. *International Journal of Remote Sensing*, **13**, 1585-1590.
- Vose JM, Swank WT (1990) Assessing Seasonal Leaf-Area Dynamics and Vertical Leaf-Area Distribution in Eastern White-Pine (*Pinus-Strobus* L) with a Portable Light-Meter. *Tree physiology*, **7**, 125-134.
- Vose JM, Dougherty PM, Long JN, Smith FW, Gholz HL, Curran PJ (1994) Factors influencing the amount and distribution of leaf area of pine stands. *Ecological Bulletins*, **43**, 102-114.
- Walther GR, Post E, Convey P, et al (2002) Ecological responses to recent climate change. *Nature*, **416**, 389-395.
- Wareing PF (1956) Photoperiodism in Woody Plants. *Annual Review of Plant Physiology and Plant Molecular Biology*, **7**, 191-214.
- White MA, Nemani AR (2003) Canopy duration has little influence on annual carbon storage in the deciduous broad leaf forest. *Global Change Biology*, **9**, 967-972.
- White MA, Nemani RR, Thornton PE, Running SW (2002) Satellite evidence of phenological differences between urbanized and rural areas of the eastern United States deciduous broadleaf forest. *Ecosystems*, **5**, 260-273.
- White MA, Running SW, Thornton PE (1999) The impact of growing-season length variability on carbon assimilation and evapotranspiration over 88 years in the eastern US deciduous forest. *International journal of biometeorology*, **42**, 139-145.

- White MA, Thornton PE, Running SW (1997) A continental phenology model for monitoring vegetation responses to interannual climatic variability. *Global Biogeochemical Cycles*, **11**, 217-234.
- Whittaker RH (1956) Vegetation of the Great Smoky Mountains. *Ecological Monographs*, **26**, 1-69.
- Zhang XY, Friedl MA, Schaaf CB (2006) Global vegetation phenology from Moderate Resolution Imaging Spectroradiometer (MODIS): Evaluation of global patterns and comparison with in situ measurements. *Journal of Geophysical Research-Biogeosciences*, **111**, G04017.
- Zhang XY, Friedl MA, Schaaf CB, Strahler AH (2004) Climate controls on vegetation phenological patterns in northern mid- and high latitudes inferred from MODIS data. *Global Change Biology*, **10**, 1133-1145.
- Zhang XY, Friedl MA, Schaaf CB, Strahler AH, Hodges JCF, Gao F, Reed BC, Huete A (2003) Monitoring vegetation phenology using MODIS. *Remote Sensing of Environment*, **84**, 471-475.
- Zhou LM, Tucker CJ, Kaufmann RK, Slayback D, Shabanov NV, Myneni RB (2001) Variations in northern vegetation activity inferred from satellite data of vegetation index during 1981 to 1999. *Journal of Geophysical Research-Atmospheres*, **106**, 20069-20083.

Chapter 4 Estimation of real-time vegetation dynamics for distributed ecohydrological modeling by fusing multi-temporal MODIS and Landsat NDVI data

4.1 Abstract

Canopy phenology is an important driver of seasonal to annual water and carbon budgets. Recent developments in remote sensing technology provide the potential to link dynamic canopy measurements with integrated process descriptions within distributed ecohydrological modeling frameworks. In particular, near real-time global satellite products (e.g. MODIS) make it possible to integrate temporal patterns of vegetation dynamics for distributed hydrological modeling. However, the coarse spatial resolution is not able to discriminate catchment scale ecohydrological dynamics. In addition, global satellite products significantly average a large portion of the landscape terrain variance, therefore a significant bias can result from lumped representation of hydrological processes. Two downscaling methods are developed to overcome this issue by fusing multi-temporal MODIS and Landsat data in conjunction with topographic information to estimate high resolution daily vegetation density over complex terrain. MODIS FPAR (fraction of absorbed photosynthetically active radiation) is used to provide medium resolution phenology, while sub-grid variability of vegetation density is estimated from composite Landsat NDVI images as a function of day of year. The relationship between the downscaled MODIS FPAR and the composite sub-grid NDVI values is represented with a simple linear proportionality parameter, which includes the

linear relationship between sub-grid NDVI and FPAR, as well as proportional phenological discrepancy between the MODIS FPAR and the Landsat composite NDVI. Combining spatial resolution of Landsat and temporal resolution of MODIS can bridge gaps between spatial and temporal limitations of both image sets in applications to catchment-scale distributed hydrological modeling. This method is used to assimilate downscaled MODIS-derived seasonal phenology into dynamic simulations of high spatial resolution patterns of water, carbon and nutrient cycling in mountainous watersheds.

4.2 Introduction

Remote sensing products provide valuable information for distributed hydrological modeling across different spatial and temporal scales, including key estimates of water and carbon state variables (e.g. soil moisture, snow, leaf area index), climatic forcing variables (e.g. precipitation, temperature), and other spatial information (e.g. land cover). The near real-time global satellite products from the moderate-resolution imaging spectro-radiometer (MODIS) on the Terra/Aqua platforms make it possible to estimate the spatial and temporal variations of water fluxes (e.g. evapotranspiration, streamflow) by assimilating several key variables for distributed hydrological modeling; snow cover (MOD10), land surface temperature/emissivity (MOD11), land cover (MOD12), leaf area index (LAI)/fraction of absorbed photosynthetically active radiation (FPAR) (MOD15), and white sky albedo (MOD43) (Andreadis and Lettenmaier 2006; Cleugh *et al.* 2007; Mu *et al.* 2007; Leuning *et al.* 2008; Pan *et al.* 2008; Zhang *et al.* 2008).

However, global satellite products from MODIS significantly average a large portion of the landscape terrain variance. Therefore, a significant bias can be derived from lumped representation of surface resistance and significant sensitivity of vapor and heat flux to soil water distributions (Band *et al.* 1993; Band and Moore 1995). For example, non-Gaussian sub-grid variability in soil moisture distributions especially under dry conditions (Famiglietti *et al.* 1999; Ryu and Famiglietti

2005) result in significant bias in modeling water and energy fluxes at the global scale, associated with non-linear responses of ecohydrological processes to soil moisture condition, transpiration (Rodrigueziturbe *et al.* 1991; Avissar 1992), runoff generation (Bronstert and Bardossy 1999; Grayson *et al.* 1997; Uchida *et al.* 2005), net primary production (Band 1993; Band and Moore 1995; Hwang *et al.* 2008), and boundary layer development (Walko *et al.* 2000).

For this reason, there have been efforts to integrate the spatio-temporal distribution of soil moisture sub-grid variability for macro-scale hydrological models, based on a priori probability distribution function of precipitation (Entekhabi and Eagleson 1989; Liang *et al.* 1996), terrain variables (Famiglietti and Wood 1994; Band *et al.* 1991; Avissar 1992; Band and Moore 1995), snow cover (Luce *et al.* 1999; Luce and Tarboton 2004), and soil properties (Liang *et al.* 1996; Liang and Xie 2001). However, a major problem of this approach is that there is no consensus for the appropriate probability distribution function for sub-grid variability (see Ryu and Famiglietti 2005). Particularly in applications for topographically complex regions, it is hard to solve for the appropriate probability density function analytically considering non-linear interactions and complex covariance structures with other biophysical variables (e.g. LAI, rooting depth).

The sub-grid variability of vegetation is often integrated into macro-scale hydrological models as a form of vegetative fraction (Gutman and Ignatov 1998), calculated from maximum and minimum vegetation indices (e.g. NDVI, EVI). A recently developed MODIS evapotranspiration algorithm estimates seasonal and spatial variations of vegetative fraction to linearly partition net radiation into vegetative and non-vegetative fraction within a MODIS pixel (Nishida *et al.* 2003; Cleugh *et al.* 2007; Mu *et al.* 2007). However, this method simplified sub-grid variability of vegetation density for the application to global evapotranspiration estimates, and may not be appropriate for local or catchment scale simulations.

Combining multi-resolution imagery can provide a possible solution for this problem. Landsat has 30-m spatial resolution with 16-day overpass frequency, but cloud contamination often limits

the ability to detect dynamics of biophysical properties such as vegetation phenology. MODIS has more frequent temporal resolution (twice a day), but a coarser spatial scale (about 250 m for red and near-infrared bands, about 500 m for other bands) than Landsat. Landsat and Terra have equal orbital parameters and less than a 30 minute difference in equator crossing time. MODIS bands have slightly narrower bandwidths compared to corresponding bands of Landsat Thematic Mapper (TM) (Table 4.1). Therefore, combining the spatial resolution of Landsat TM and the temporal resolution of MODIS can bridge gaps between limitations of both image sets in applications to distributed hydrological modeling at local scales.

Traditional studies fusing multi-resolution images have focused on producing high resolution multi-spectral images by combining a fine resolution panchromatic band and coarse resolution spectral bands (e.g. Pohl and van Genderen 1998). Recently, Gao *et al.* (2006) successfully produced high-resolution spatial reflectance by blending Landsat Enhanced TM+ and MODIS surface reflectance with the spatial and temporal adaptive reflectance fusion model (STARFM). However, this method is too dependent on finding pure coarse-resolution neighborhood pixels and is hard to apply for topographically complex terrain where the solar bidirectional reflectance distribution function (BRDF) changes not only temporally, but also as a function of topographic position. Roy *et al.* (2008) also suggested an interesting fusing method between Landsat and MODIS data using the MODIS BRDF/albedo products (MCD43). They used a simple ratio to estimate Landsat reflectance on a prediction date from reflectance on an observation date. The ratio was calculated from the 500 m surface reflectance on both dates, simulated with the MODIS BRDF parameters and sun-sensor geometry (Roy *et al.* 2008). Note that the target variable of these fusing methods was reflectance at each spectral band.

Table 4.1: Landsat TM and MODIS bandwidths of red and near infrared bands

	Landsat TM bandwidth (nm)	MODIS band bandwidth (nm)
Red	630 ~ 690 (band 3)	620 ~ 670 (band 1)
Near infrared	760 ~ 900 (band 4)	841 ~ 876 (band 2)

The ‘ratioing’ indices (e.g. NDVI, EVI, SR) provide more consistent spatial and temporal criteria for vegetation conditions than reflectance after normalization of external radiometric and atmospheric effects. This is because they may cancel out a large portion of the multiplicative noise attributed to illumination differences, cloud shadows, topographic variations, and atmospheric conditions (Huete *et al.* 2002). Normalized difference vegetation index (NDVI) is a normalized ratio between surface reflectance of red and near infrared bands:

$$NDVI = (\rho_{NIR} - \rho_{RED}) / (\rho_{NIR} + \rho_{RED}) \quad (4.1)$$

where ρ_{RED} and ρ_{NIR} are surface reflectance of red and near-infrared bands. NDVI is directly related to various vegetation biophysical parameters (e.g. LAI, FPAR, canopy cover, and biomass) across different ecosystems (Tucker 1979; Asrar *et al.* 1984; Sellers 1985). The spatio-temporal consistency of NDVI for vegetation dynamics can provide significant advantages over reflectance as a target variable when applying multi-resolution methodology in topographically complex terrain.

Vegetation density is closely related to the fraction of absorbed photosynthetically active radiation (FPAR) and leaf area index (LAI). FPAR is a good indicator for energy absorption by vegetation and subsequent carbon uptake based on the light use efficiency. LAI is an important driver in process-based biogeochemical models, which tends to be correlated with aboveground net primary production and biomass across a broad range of ecosystems (Gower *et al.* 2001; Asner *et al.* 2003). LAI determines canopy interception capacity for evaporation and potential transpiration through stomata in the water cycle. Vegetation compromises between its growth and water stress for optimal carbon uptake (so-called ‘growth-stress trade-off’) (Mackay 2001; Kerkhoff *et al.* 2004), represented as a non-linear relationship between FPAR (energy use) and LAI (water use). These two important biophysical properties are linearly or non-linearly correlated with NDVI from

remote sensing images, so NDVI may play a crucial role for downscaling vegetation density by combining multi-resolution images at topographically complex terrain.

In this study, we suggest two downscaling methods of near real-time global satellite products (MODIS) into Landsat scale FPAR/LAI values for distributed hydrological modeling. MODIS FPAR can be downscaled into fine resolution each day, based only on sub-grid variability of composite Landsat TM NDVI with (a topographically corrected downscaling) or without (a simple downscaling) considering sub-grid variability of potential incoming radiation. Combining spatial resolution of Landsat and temporal resolution of MODIS can overcome temporal and spatial limitations of both image sets in applications of global satellite products into catchment-scale distributed hydrological modeling.

4.3 Method and Materials

4.3.1 Study site

The Coweeta Hydrologic Lab is located in western North Carolina, USA and is representative of the Southern Appalachian forest (Figure 4.1). The Southern Appalachian forest has very diverse flora as a result of the complex terrain and consequent variability in microclimates and soil moisture (Whittaker 1956; Day and Monk 1974). Mean monthly temperature varies from 3.6 °C in January to 20.2 °C in July. The climate in the Coweeta basin is classified as marine, humid temperate, and precipitation is relatively even in all seasons; annual precipitation ranges from 1870 mm to 2500 mm with about a 5% increase for each 100 m (Swift *et al.* 1988). The dominant species are oaks and mixed hardwoods including *Quercus* spp. (oaks), *Carya* spp. (hickory), *Nyssa sylvatica* (black gum), *Liriodendron tulipifera* (yellow poplar), and *Tsuga canadensis* (eastern hemlock), while major evergreen undergrowth species are *Rhododendron maximum* (rhododendron) and *Kalmia latifolia* (mountain laurel) (Day *et al.* 1988).

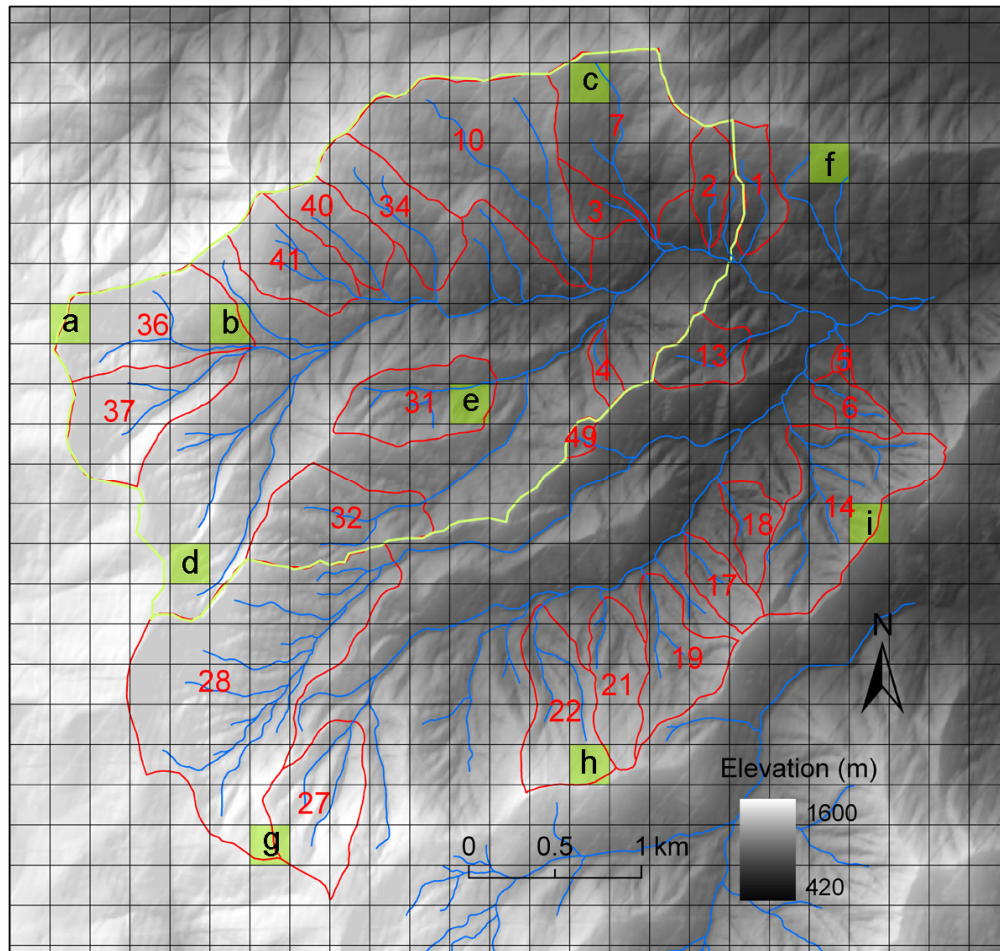


Figure 4.1: A study site (Coweeta Hydrologic Lab). Grids represent the MODIS (MOD13Q1; about 230 m) pixels. Red and yellow lines represent the boundaries of sub-watersheds and WS08 (an upper basin of Coweeta). Letters indicates the pixels for examples of fitting and downscaling methods (Figure 4.2; Figure 4.3; Figure 4.8; Figure 4.9)

A distributed hydrological model is simulated at the upper basin of Coweeta (Shope Fork creek; WS08; Figure 4.1) with 30-m grid scale ($n = 8654$), which includes very diverse ranges of topographic factors (elevation, aspect, slope, and topographic index). The Coweeta basin has distinct phenological patterns at different topographic positions. Onset of greenup is delayed by about a month as a strong linear relationship of elevation, and onset of dormancy also shows unique spatial patterns by a combination of temperature, orographic precipitation, and photoperiod (Chapter 3). These distinct spatial patterns of vegetation phenology within the basin facilitate the use of near real-time global satellite products for distributed hydrological simulation, with respect to not only interannual variations but also spatial variations of vegetation phenology.

4.3.2 *Landsat NDVI*

We acquired forty-nine Landsat 5 TM images in this study site from 2000 to 2008 (WRS path 19/row 36 and path 18/row 36), all of which are absolutely cloud-free for the study area and standard level-one terrain-corrected (L1T) products. The L1T product includes radiometric, systematic geometric, and precision correction using ground control chips, and uses digital elevation model (DEM) to correct parallax error due to local topographic relief (Johnson *et al.* 2009). Geolocation accuracy of the L1T product depends on the resolution of the DEM used. The geolocation error of L1T-level corrected Landsat images is less than 30 m in the United States even in areas with substantial terrain relief (Lee *et al.* 2004). All images are provided as a GeoTIFF file format with the Universal Transverse Mercator (UTM) coordinate system. Dark object subtraction (DOS) method is commonly used for Landsat TM imagery to correct atmospheric effects on surface reflectance (Chavez 1996). In this study, we used a modified DOS method which adds the effect of Rayleigh scattering to the conventional DOS method. This method was claimed to produce the best overall results in terms of classification and change detection, compared to other more complicated

atmospheric correction method (Song *et al.* 2001). A detailed methodology is available in Song *et al.* (2001).

Daily composite NDVI images at each day of year (DOY) are produced from Landsat images within 15-days after and before with an inverse distance weighting method. Based on daily composite NDVI images, near real-time MODIS NDVI values are downscaled into Landsat resolution. A compositing method is usually integrated to fill cloud-contaminated or missing pixels for near-daily global satellite products (e.g. AVHRR, MODIS) (Huete *et al.* 2002). In this study, however, this method is integrated to estimate the sub-grid variability of the MODIS NDVI at each DOY. Note that sub-grid variability of MODIS NDVI temporally changes as vegetation phenology has distinct temporal patterns at sub-grid scale by a combined effect of micro-climate condition, vegetation community types, and hillslope position in this study site (Chapter 3).

This method explicitly assumes that the sub-grid variability of MODIS NDVI changes seasonally, but has negligible interannual variations. Vegetation at the sub-grid scale may respond differently to interannual climatic variations, therefore this assumption introduces some error. A main reason why we do not produce daily composite NDVI images at each date is that there are not enough images to cover full phenological patterns each year. However, we believe that temporal variations of sub-grid variability are more dynamic and significant than interannual variations of sub-grid variability. We will check this assumption later. Therefore, interannual variations of vegetation phenology are solely dependent on temporal trajectories of MODIS NDVI, while sub-grid variability of MODIS NDVI is determined by composite Landsat NDVI on corresponding DOY.

4.3.3 *MODIS NDVI and FPAR*

MODIS NDVI products (MOD13Q1 version 5) are released in the HDF-EOS data format as Sinusoidal projections with 16-day temporal resolution and approximately 250-m spatial resolution.

The MODIS geolocation error is approximately 50 m at nadir (Wolfe *et al.* 2002). They are reprojected to the GeoTIFF file format with the UTM coordinate system using a bilinear resampling technique by the MODIS reprojection tool (MRT; https://lpdaac.usgs.gov/lpdaac/tools/modis_reprojection_tool). The current version of MODIS NDVI products (version 5) is provided with two newly added parameters; pixel reliability and day of composite (Didan and Huete 2006). Based on the pixel reliability, good and marginal NDVI values are chosen for post-processing analysis for the production of MODIS NDVI values from late 2000 to early 2009. Marginal data are included for this study as there is an insufficient number of good quality data to show the full range of phenological patterns, and even good quality data have unreasonable phenological patterns in this high-precipitation region. The day of composite information at each pixel is also retrieved to get the exact acquisition date during the composite period (Didan and Huete 2006). This information was suggested to be quite important for extracting exact phenological signals (Fisher and Mustard 2007).

A simple two-step filtering method is incorporated to filter out unqualified data points after initial quality control based on pixel reliability values at each pixel. This two-step filtering technique consists of an outlier exclusion method and a modified Best Index Slope Extraction (BISE) method (Chapter 3). After this simple post-processing, a difference logistic function is used to fit temporal MODIS NDVI values (Fisher *et al.* 2006).

$$y(t) = \left(\frac{1}{1 + e^{a+bt}} - \frac{1}{1 + e^{a'+b't}} \right) \cdot c + d \quad (4.2)$$

Details in filtering and fitting MODIS NDVI values are available in chapter 3.3. In the process of non-linear model fitting, fitting parameters are sometimes not identifiable as there are no proper intermediate values between maximum and minimum NDVI in the middle of the greenup and

senescence periods. In this case, we reduced fitting variables by using shape parameters (b and b' in Eq. 4.2) estimated from 8-year composite trajectories as a function of DOY (Figure 3.4).

Vegetation phenology at forest-based ecosystems is quite periodic. Therefore there is only a single mode of greenup and senescence per year. Compared to a logistic function, fitting with the difference logistic function can reduce the number of fitting variables and assure the continuity of maximum NDVI values between phases during the summer. At each year, the model is fitted between mid-days of dormancy periods in this year and the next year. Mid-day of dormancy periods are calculated from the model fitting of multi-year NDVI trajectories as a function of DOY at each pixel.

A key MODIS product to downscale is the fraction of absorbed photosynthetically active radiation (FPAR) (Myneni *et al.* 2002). Phenological patterns of FPAR are important not only for carbon assimilation based on light use efficiency, but also potential canopy interception capacity for evaporation in a water cycle. FPAR has a linear relationship with NDVI across different satellite sensors (Myneni *et al.* 2002; Sellers 1985; Asrar *et al.* 1992; Myneni and Williams 1994; Knyazikhin *et al.* 1998; Hall *et al.* 1992). The linear NDVI-FPAR relationship is known to be largely dependent on vegetation community type and structure. We estimated a linear NDVI-FPAR relationship locally by matching 1-km MODIS NDVI (MOD13A2) and FPAR (MOD15A2) in the study area. Note that the MODIS FPAR/LAI (MOD15A2) is currently provided at only about 1-km spatial resolution, so we used this linear NDVI-FPAR relationship to transform the 250-m MODIS NDVI (MOD13Q1) into estimated MODIS FPAR values.

4.3.4 Downscaling MODIS FPAR into sub-grid scale

MODIS FPAR represents the integrated effect of sub-grid FPAR values. There can be two ways to express the relationship between the MODIS FPAR and sub-grid FPAR values. First, the MODIS

FPAR on date t ($FPAR_t$) can be expressed as a mean value of all sub-grid FPAR values on date t ($FPAR_{i,t}$) as in

$$FPAR_t = \frac{\sum_{i=1}^n FPAR_{i,t}}{n} \quad (4.3)$$

where i represents sub-grid pixel locations, and n is the number of sub-grid pixels within a single MODIS pixel. The numbers of sub-grid pixels (n) are between 49 (7×7) and 64 (8×8) considering that MODIS (~ 230 m) and Landsat TM (30 m) spatial resolutions. However, this equation explicitly assumes that all sub-grid pixels receive uniform incident PAR. If we consider the sub-grid variability of incident PAR, $FPAR_t$ can be expressed with a weighted average of $FPAR_{i,t}$ with incident PAR at each sub-grid pixel on corresponding DOY ($IPAR_{i,DOY}$) as in

$$FPAR_t = \frac{\sum_{i=1}^n APAR_{i,t}}{\sum_{i=1}^n IPAR_{i,DOY}} = \frac{\sum_{i=1}^n (FPAR_{i,t} \cdot IPAR_{i,DOY})}{\sum_{i=1}^n IPAR_{i,DOY}} \quad (4.4)$$

where $APAR_{i,t}$ is the absorbed PAR at each sub-grid pixel i and date t . Total potential incoming PAR on each slope is a function of topography and solar geometry. Potential incoming radiation at each pixel ($IPAR_{i,DOY}$) is calculated at Terra crossing time (around 10 a.m. local time) on the corresponding DOY, based on MT-Clim algorithm (Running *et al.* 1987). Note that potential IPAR should be used for this equation, not actual PAR measurement, because fitted $FPAR_t$ values are not actual measurements, but estimates under the assumption of cloud-free conditions.

Checking the difference between Eq. 4.3 and 4.4 is to test scale invariance of FPAR; a concept proposed by Hall *et al.* (1992). The definition of scale invariance is that biophysical parameters estimated from aggregated radiance at coarse resolution (lumped) should be the same with aggregated biophysical parameters calculated from fine resolution radiance (averaged). In Eq. 4.3,

integrated FPAR ($FPAR_t$) is defined as aggregated mean from sub-grid FPAR ($FPAR_{i,t} = APAR_{i,t}/IPAR_{i,DOY}$), whereas $FPAR_t$ is calculated from aggregated IPAR ($\sum IPAR_{i,DOY}$) and APAR ($\sum APAR_{i,t}$) in Eq 4.4.

We used the composite Landsat NDVI image as an indicator for the sub-grid variability of the MODIS FPAR, assuming the simple linear relationship between sub-grid FPAR at each time ($FPAR_{i,t}$) and composite Landsat NDVI on corresponding DOY ($NDVI_{i,DOY}$) as in

$$FPAR_{i,t} = \alpha_t \cdot NDVI_{i,DOY} \quad (4.5)$$

where α_t is a key proportionality parameter of the downscaling process in each MODIS pixel that varies with time t . α_t parameter includes both the linear relationship between Landsat NDVI and sub-grid FPAR, as well as proportional phenological discrepancy between near real-time MODIS FPAR and composite Landsat NDVI on corresponding DOY. Note that $FPAR_{i,t}$ is a final target variable for a downscaling process, simply calculated by multiplying $NDVI_{i,DOY}$ with the time-varying proportionality parameter (α_t). This method explicitly assumes a constant coefficient of variance between $FPAR_{i,t}$ and $NDVI_{i,DOY}$. The equation is also based on the assumption that there is no disturbance during the simulation period, which may be true in this study site.

α_t can be solved by inserting Eq. 4.5 into Eq. 4.3 and 4.4 such as

$$\alpha_{t, simple} = \frac{FPAR_t \cdot n}{\sum_{i=1}^n NDVI_{i,DOY}} \quad (4.6)$$

$$\alpha_{t, topo-corrected} = \frac{FPAR_t \cdot \sum_{i=1}^n IPAR_{i,DOY}}{\sum_{i=1}^n (NDVI_{i,DOY} \cdot IPAR_{i,DOY})} \quad (4.7)$$

Both α_t are calculated at MODIS scale on each date, which provides proportionality between target variables ($FPAR_{i,t}$) and the composite NDVI values on corresponding DOY ($NDVI_{i,DOY}$). We would call these two techniques as a simple and a topographically corrected downscaling method. Note that all variables related to sub-grid variability ($NDVI_{i,DOY}$, $IPAR_{i,DOY}$) are calculated based on DOY, which would not only reduce computational loads, but also provide a basis of fusion between spatial and temporal resolutions of MODIS and Landsat image sets. For significant geolocation errors for both Landsat (< 30 m) and MODIS (< 50 m) images, Landsat pixels with two and more MODIS grids crossover, are calculated as a sub-pixel of the MODIS grid to which largest portion of these Landsat pixels belongs.

Finally, sub-grid LAI values are calculated from $FPAR_{i,t}$ values by a non-linear relationship between FPAR and LAI, which is locally derived by field measurements in the study area (Sullivan *et al.* 1996).

4.3.5 *Simulation of a distributed ecohydrological model*

A process-based ecohydrological model (RHESSys; Regional Hydro-Ecological Simulation System) (Band *et al.* 1993; Tague and Band 2004) is used in this study. The model is simulated at 30×30 m downscaled grid cell resolution within WS08 (patch; $n = 8654$). Daily climate (maximum and minimum temperature, precipitation, average vapor pressure deficit, total downward direct radiation) at two climate/rain gauge stations at low and high elevation (CS01/RG06 and CS28/RG31) are used in this study. For the model simulation, we used universal kriging with elevational trends from 7-point measurements within the Coweeta basin from 1991 to 1995 to develop long-term rainfall isohyets to scale daily precipitation over the terrain. Many physiological parameters and other (e.g. soil, nutrient) parameters measured within the study site are used (Hwang *et al.* 2009).

The model is calibrated with streamflow data varying three TOPMODEL parameters, m (the decay rate of hydraulic conductivity with depth), and the lateral/vertical K_{sat0} (saturated hydraulic conductivity at surface). Monte-Carlo simulation is implemented two thousand times with randomly sampled parameter values within certain acceptable ranges for a three-year calibration period (October 2003 ~ September 2006). To allow soil moisture to stabilize, a one and a half year initialization is employed before the calibration period. The Nash-Sutcliffe (N-S) coefficient (Nash and Sutcliffe 1970) for lognormal streamflow discharge is used to evaluate model performance because this objective function is biased toward base flow, which is more sensitive to vegetation dynamics.

4.4 Results

4.4.1 MODIS and Landsat NDVI values

Figure 4.2 shows 8-year (2001 ~ 2008) temporal patterns of filtered MODIS NDVI values and fitted models on MODIS pixels in topographically different positions within the study site (Figure 4.1). They show very periodic phenological patterns each year, as well as very stable maximum and minimum NDVI values during maturity and dormancy periods. The diverse phenological patterns shown within the Coweeta LTER site can be explained by the combined effect of micro-climate variations, vegetation community types, and hillslope position (Chapter 3). Note that there are some discontinued patterns between years because filtered MODIS data are non-linearly fitted independently with the difference logistic function for each year.

Figure 4.3 presents phenological patterns at selected MODIS pixels for the same 8-year period as a function of DOY. Interannual variations of vegetation phenology appear smaller than spatial variations. Senescence shows more interannual variation than greenup. This pattern can be observed more clearly from boxplots of all mid-days of greenup and senescence periods in each year ($n =$

369; Figure 4.4a, b), defined as inflection points of the difference logistic function (Eq. 4.2). The mid-days of greenup show smaller interannual variations than those of senescence for the Coweeta basin. The greenup was delayed significantly in 2005 compared to other years. Significantly delayed senescence was observed in 2005, while earlier senescence was found in 2001, 2003, and 2004.

All Landsat NDVI values are presented in Figure 4.5 as a function of DOY, where vertical lines represent 5th and 95th percentiles of spatial NDVI values within the WS08 watershed ($n = 8654$; Figure 4.1). The atmospheric correction method efficiently normalized NDVI values. It produces very stable patterns in terms of not only absolute mean values but also their spatial distributions except for greenup and senescence periods. Note how stable spatial distributions of Landsat NDVI values are between adjacent images even though there are some interannual differences in absolute terms. The consistency in spatial patterns of Landsat NDVI values is quite important as we estimate sub-grid variability of MODIS FPAR on each DOY based on composite spatial patterns without considering interannual variations. Note that there are still small systematic decreases of average Landsat NDVI values and small increases of their spatial distributions in the middle of winter (Figure 4.5). These phenomena are thought to be related to the underestimation of NDVI values at high solar zenith angle and large spatial variance of the cosine of illumination angle around the winter solstice. We discuss this issue later with respect to topographic correction.

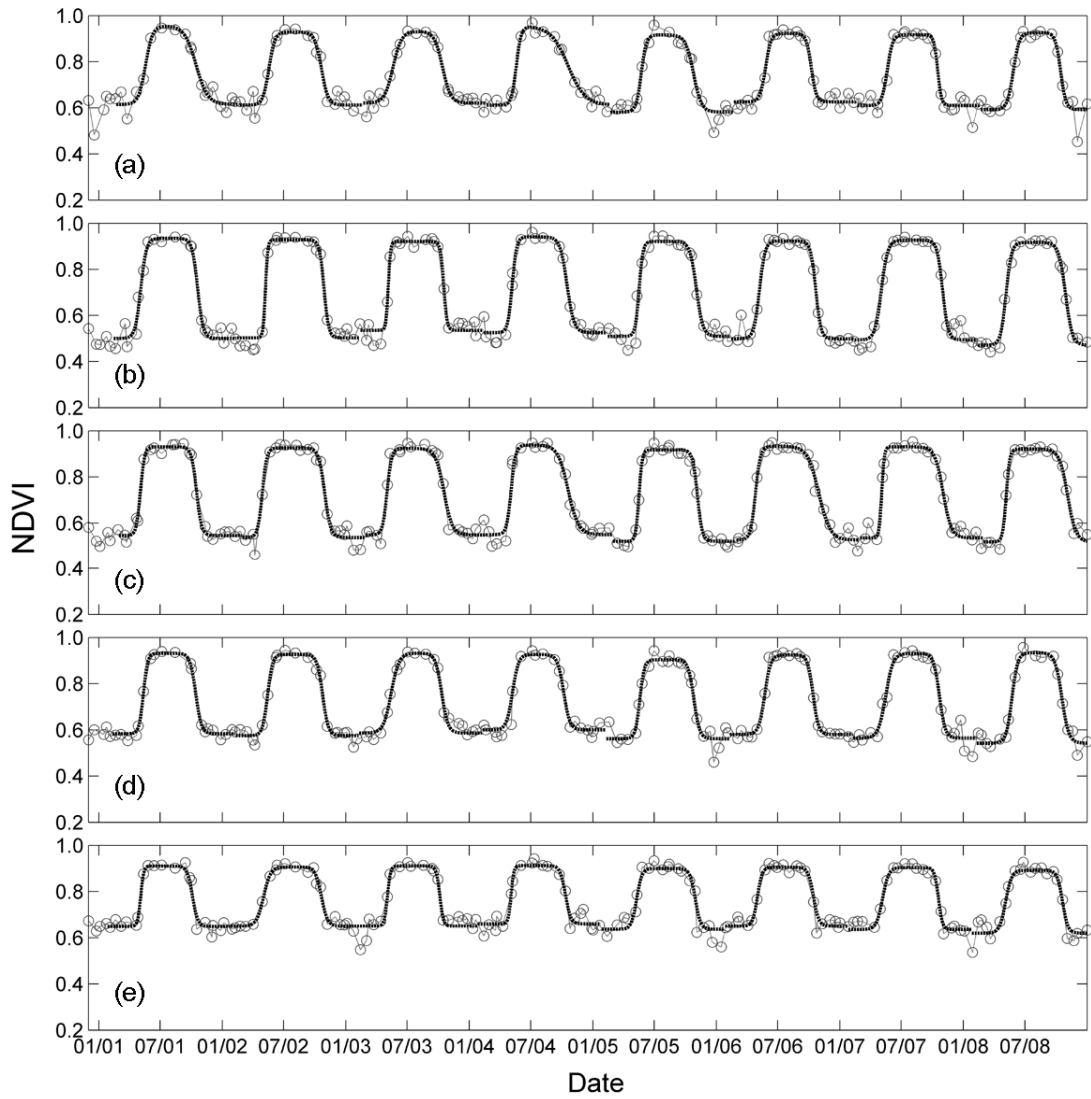


Figure 4.2: Examples of fitting by the difference logistic function for 8-year MODIS NDVI datasets (2001 ~ 2008) at selected MODIS pixels ((a) ~ (i); Figure 4.1).

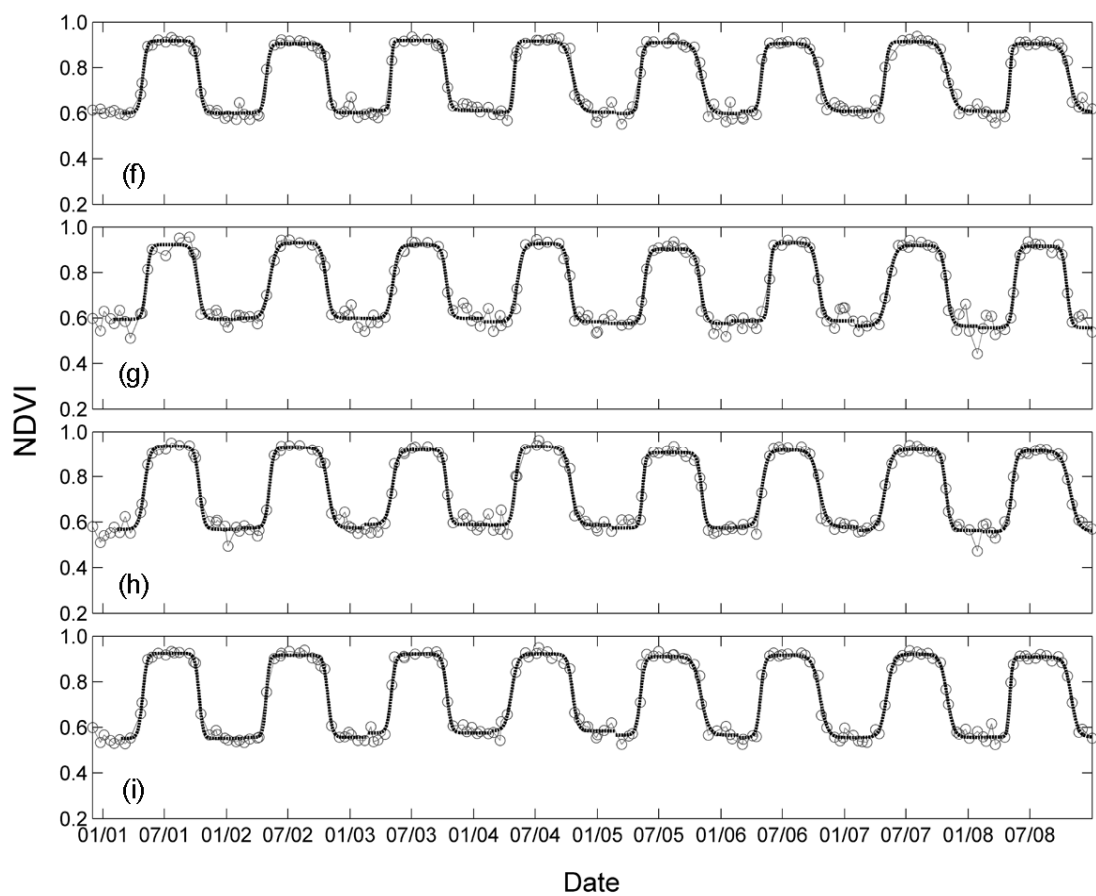


Figure 4.2 (cont'd)

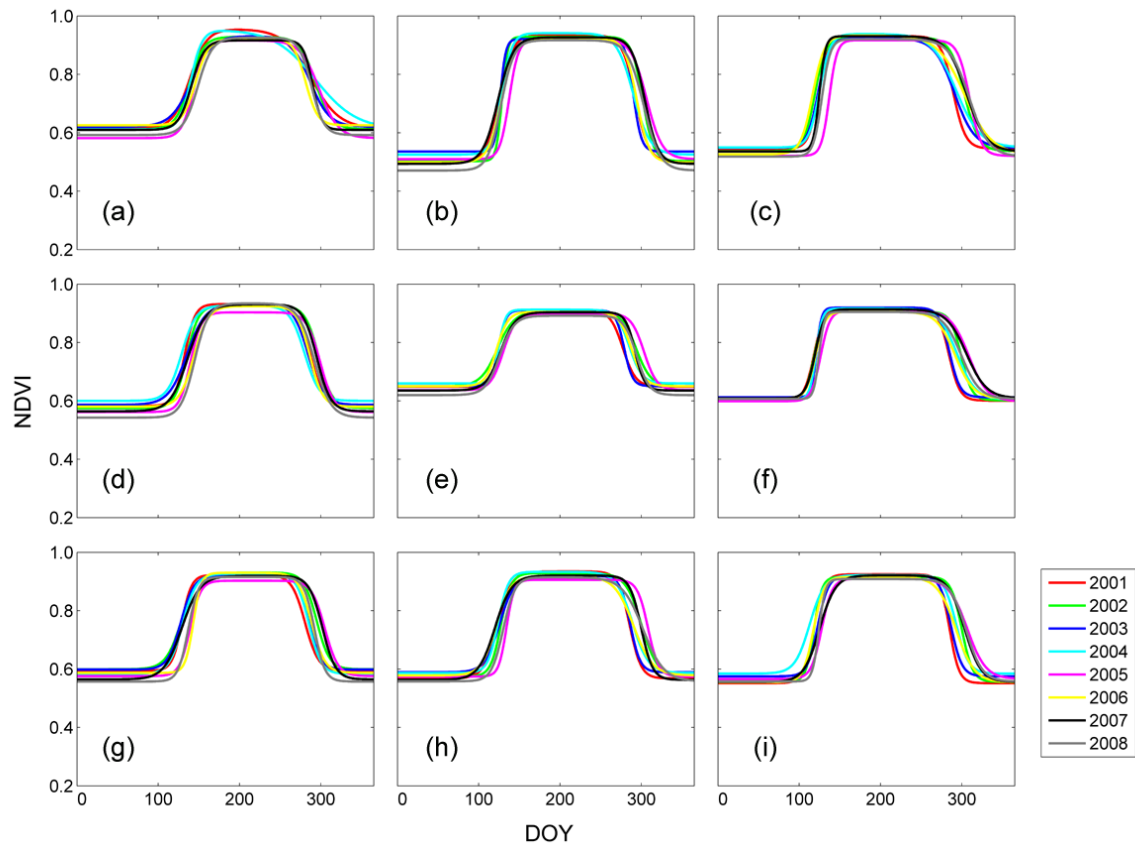


Figure 4.3: Interannual phenological variations of the fitted MODIS NDVI model at selected MODIS pixels ((a) ~ (i); Figure 4.1).

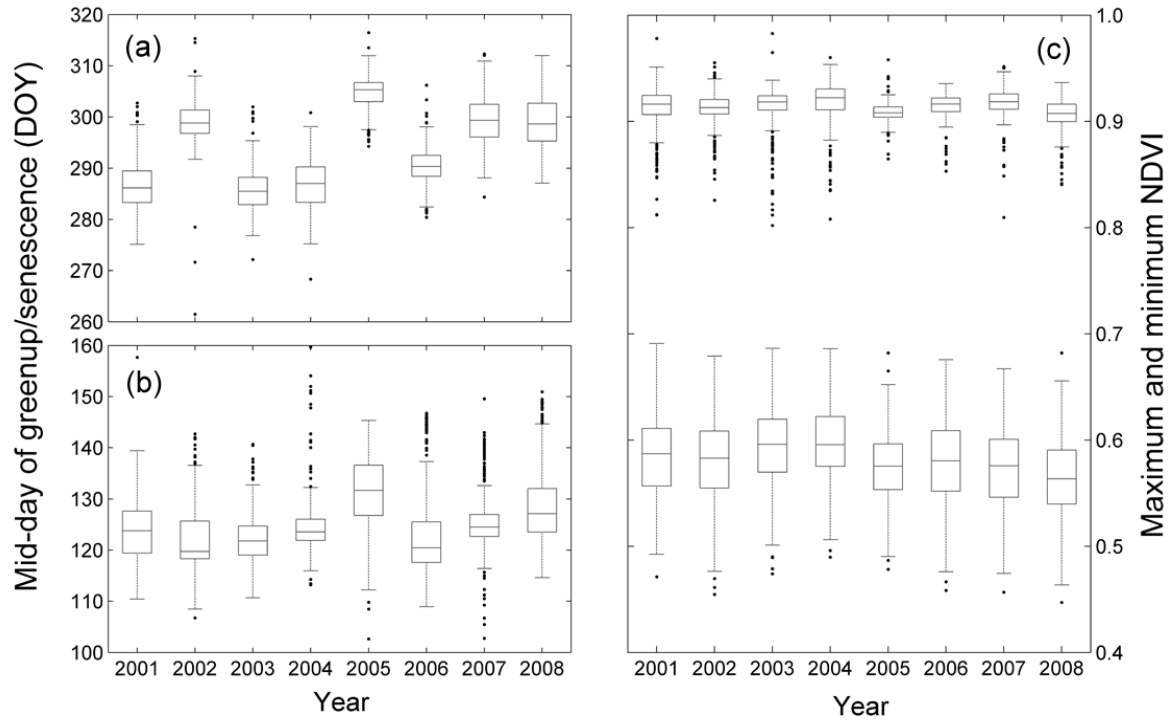


Figure 4.4: Boxplots for spatial variations of mid-day of (a) greenup and (b) senescence periods, and (c) fitted maximum and minimum NDVI values within the study site ($n = 369$) for each year, calculated from the fitted MODIS NDVI model (Figure 4.3). Boxes have lines at the lower, median, and upper quartile values. Lines are extended to the most extreme values within the Whiskers, defined as 1.5 times the inter-quartile range from the lower and upper quartiles. Outliers are displayed with black dots.

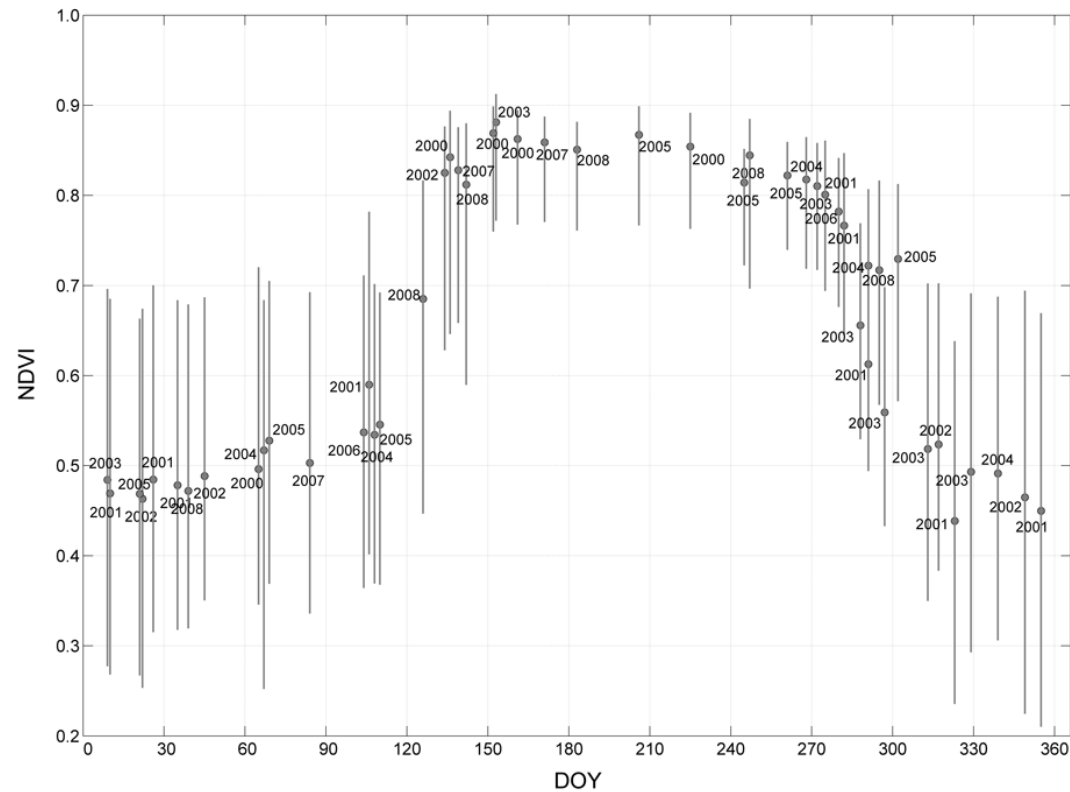


Figure 4.5: Spatio-temporal patterns of Landsat NDVI values within the Coweeta basin as a function of DOY. All Landsat TM images are from 2000 to 2008, and absolutely cloud-free. Points and vertical lines represent an average, and 5th and 95th percentiles of spatial NDVI values within the WS08 watershed ($n = 8654$; Figure 4.1).

Maximum and minimum values of Landsat NDVI (Figure 4.5) are consistently lower than those of fitted MODIS NDVI (Figure 4.4c). Note that Landsat NDVI is just used to estimate the sub-grid variability of MODIS pixels assuming the standard deviation is proportional to the mean value, so these differences in maximum and minimum NDVI values have limited effects on the suggested downscaling techniques. Greenup and senescence timing from Landsat NDVI images (Figure 4.5) are quite comparable to those from fitted MODIS NDVI (Figure 4.4a, b). Fall Landsat NDVI shows earlier senescence in 2001 and 2003, but is delayed in 2005 and 2008. Interannual variations in the mid-day of senescence from MODIS NDVI data (Figure 4.4a) exactly agree with these observed patterns from fall Landsat NDVI images, as well as their absolute timing as DOY values. Even though it is hard to see interannual variations in greenup timing for the lack of cloud-free Landsat TM images, earlier greenup is observed in 2001 compared to 2004 and 2005 (Figure 4.5), also partially supported by the MODIS data (Figure 4.4b).

4.4.2 *An example of downscaling*

Figure 4.6 presents an example of downscaling MODIS FPAR into Landsat-scale FPAR by the two methods. This downscaling example (May 5, 2008) is chosen around the middle of the greenup period (Figure 4.4b), when broad ranges of FPAR and NDVI are expected to show this downscaling process more efficiently. A fitted MODIS FPAR image (Figure 4.6a) and a composite Landsat NDVI image on corresponding DOY (Figure 4.6b) show very similar spatial patterns along the elevation gradient. A proportionality parameter (α_t) of the simple downscaling is calculated for each MODIS pixel by Eq. 4.6 (Figure 4.6c), which is multiplied by the composite NDVI image to produce a final downscaled FPAR map (Figure 4.6d). Gradual decreases of α_t value along the elevation gradient are observed except for several pixels around the basin outlet, where the Coweeta lab buildings are. Note that the α_t parameter adjusts Landsat NDVI values each day based on observed global satellite signals while preserving sub-grid variability. Therefore, this elevational

trend of the α_t parameter may explain the phenological discrepancy between MODIS FPAR and composite Landsat NDVI. The topographically corrected α_t parameter (not shown here) is calculated by Eq. 4.7 with estimated potential hourly radiation (Figure 4.6e). A final FPAR map developed by topographically corrected downscaling is shown in Figure 4.6f, which appears similar to a final FPAR map from the simple downscaling (Figure 4.6d).

More downscaling examples are available in Figure 4.7 for mid-summer (July 1, 2008; left column) and mid-winter (February 8, 2008; right column). Both composite NDVI images clearly show boundaries of coniferous watersheds (WS01, WS17; Figure 4.1), characterized as lower NDVI values in summer (Figure 4.7c) and higher NDVI values in winter (Figure 4.7d). These distinct patterns of coniferous watersheds are less distinguishable in the MODIS FPAR images (Figure 4.7a, b), where the effect of coniferous forests is mixed with adjacent pixels. FPAR maps from the topographically corrected downscaling (Figure 4.7e, f), show relatively good spatial continuity between adjacent pixels. In the middle of summer (maturity) and winter (dormancy), there is little interannual variation in vegetation phenology, so α_t parameters are expected to be more spatially uniform than those of the transition periods. However, there are still discrete downscaled FPAR patterns from MODIS pixels with mixed biome types especially in summer (Figure 4.7e). Note that few discrete patterns are found in winter (Figure 4.7f), when only coniferous and understory evergreen broadleaf (e.g. rhododendron, mountain laurel) forests are photosynthetically active.

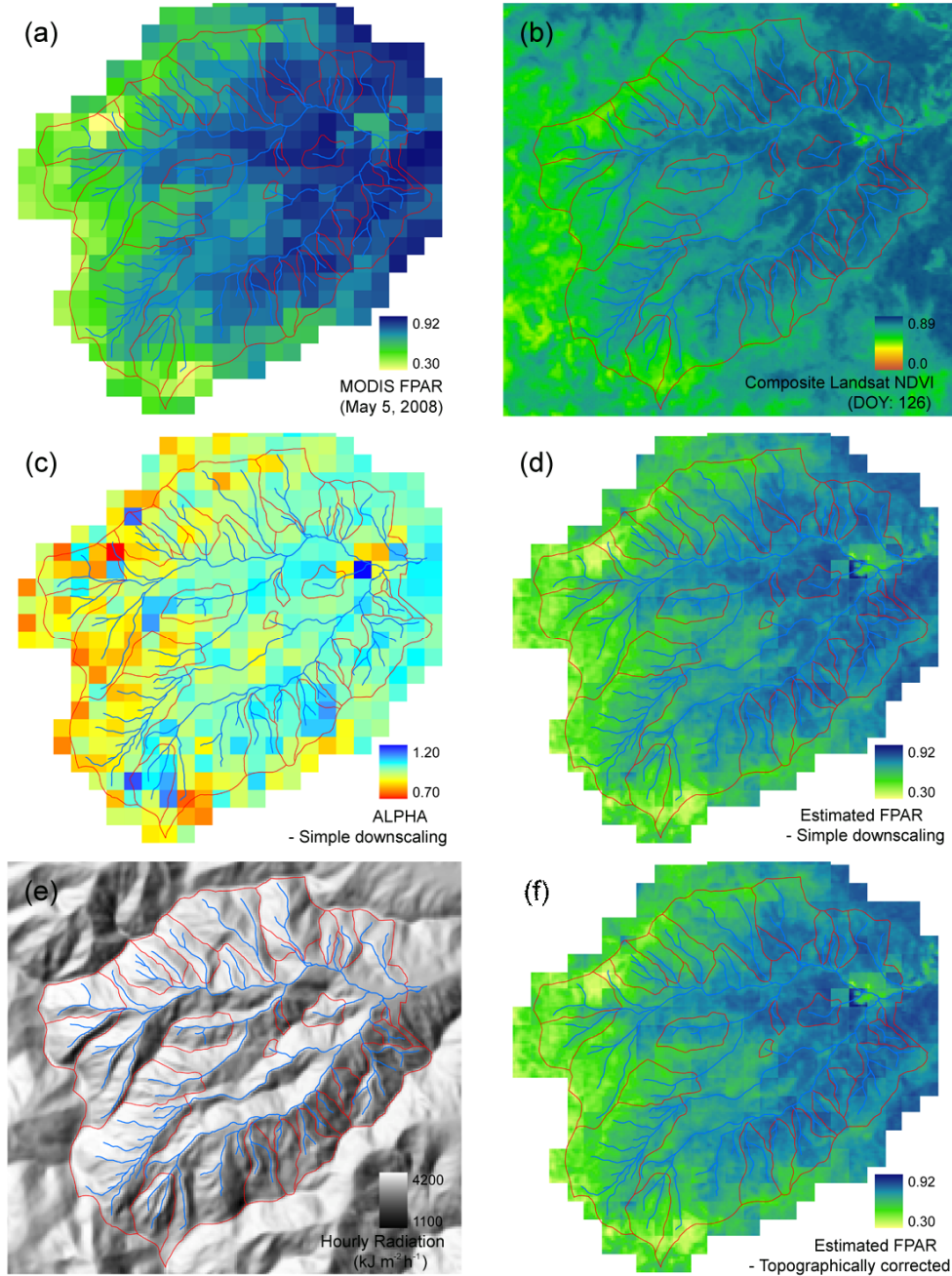


Figure 4.6: An example of two downscaling methods on May 5, 2008; (a) a fitted MODIS FPAR image, (b) a composite Landsat NDVI image, (c) a proportionality parameter (α_i) map by the simple downscaling method, (d) a downscaled FPAR map by the simple downscaling method, (e) a potential hourly radiation map ($\text{kJ m}^{-2} \text{h}^{-1}$), and (f) a downscaled FPAR map by the topographically corrected downscaling method.

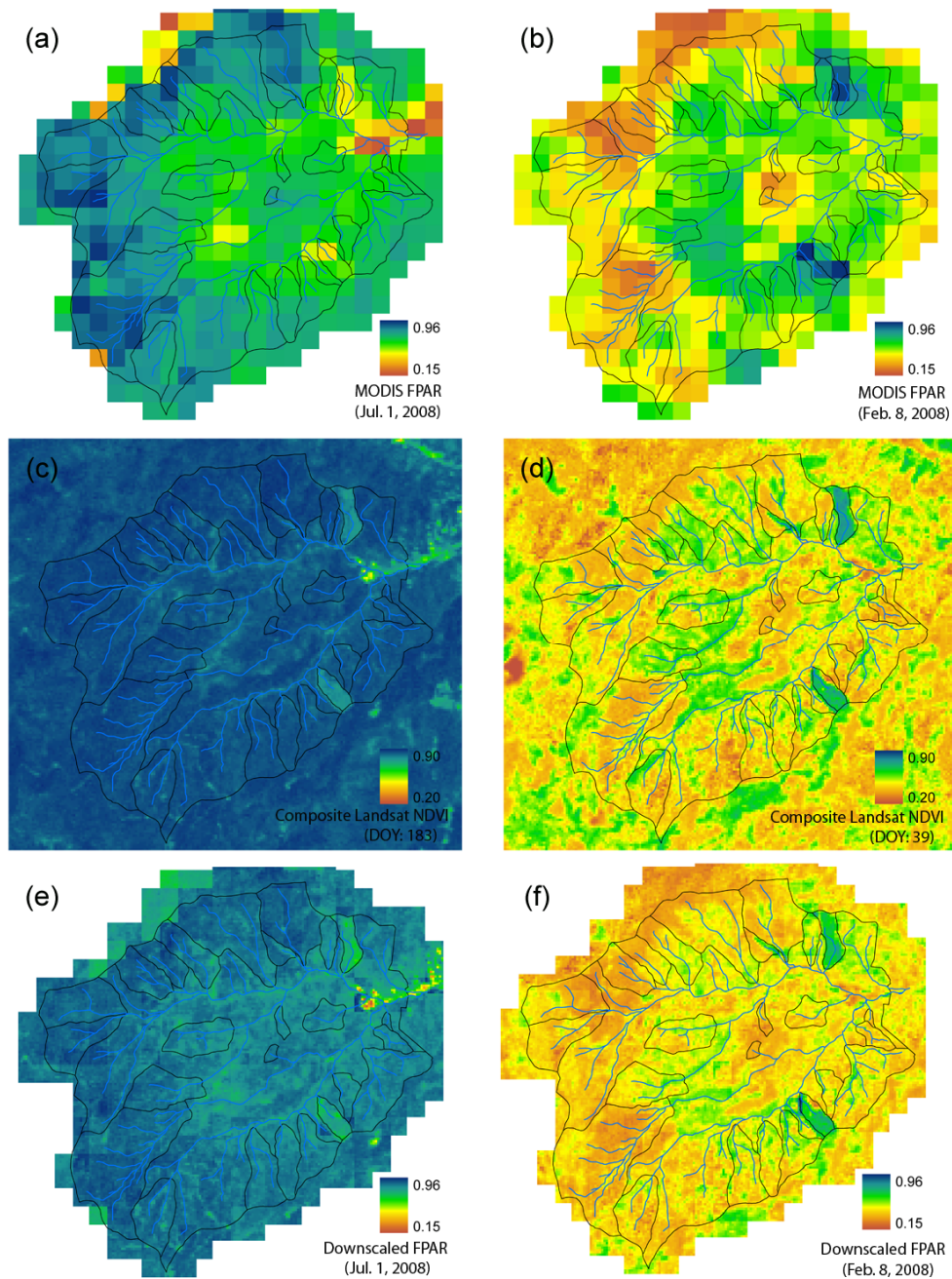


Figure 4.7: Two examples of the topographically corrected downscaling method on July 1, 2008 (left column) and February 8, 2008 (right column); (a) and (b) fitted MODIS FPAR images, (c) and (d) composite Landsat TM NDVI images, and (e) and (f) downscaled FPAR maps.

Figure 4.8 and Figure 4.9 show examples of downscaled FPAR and LAI values by the topographically corrected downscaling at selected MODIS pixels with 5-day intervals (Figure 4.1). Temporal patterns of downscaled FPAR show exaggerated spatial variance in low ranges due to the non-linear relationship between LAI and FPAR (Figure 4.8). Note that each MODIS pixel presents quite different downscaled FPAR and LAI patterns depending on temporally variant sub-grid variability estimated from composite Landsat NDVI images. Usually, relatively stable patterns of downscaled FPAR and LAI values are found during dormancy and maturity periods with a few crossovers. Some instability of downscaled FPAR might be from interannual variations of composite Landsat NDVI images or geolocation problems of both images (Figure 4.5). Note that increases of downscaled FPAR and LAI are found in some MODIS pixels in the middle of winter (Figure 4.8e, g and Figure 4.9e, g), which could not be true. We believe that this pattern is related to underestimation of NDVI in faintly illuminated areas with very high solar zenith angle around the winter solstice. This pattern is also related to systematic decreases of average Landsat NDVI values and small increases of their spatial distribution in the middle of winter (Figure 4.5). Note that these two MODIS pixels (Figure 4.1e, g) are located in north-facing slopes, where diffuse radiation is dominant during the winter season.

4.4.3 *The effect of the topographically corrected downscaling*

The example for two downscaling methods in spring shows that there is no apparent difference between final downscaled FPAR products (Figure 4.6d, f). The scatter plots between α_{simple} (a proportionality parameter in the simple downscaling; Eq. 4.6) and $\alpha_{topo_corrected}$ (a proportionality parameter in the topographically corrected downscaling; Eq. 4.7) in spring (May 5, 2008), winter (February 8, 2008), and summer (July 1, 2008) are shown in Figure 4.10. Note that final downscaled FPAR maps are developed as the product of composite NDVI images and the α parameters. Therefore, the effect of the topographically corrected downscaling can be assessed by

comparison between α parameters from both methods. In the summer, there is little difference between two α parameters. Few points are found out of the 1-to-1 line in the spring, but they are located within a broader range. The greatest deviations from the 1-to-1 line are in the winter season with the broadest range.

Increased discrepancy of the α parameters in winter is related to increased covariance between sub-grid NDVI values ($NDVI_{i,DOY}$; Eq. 4.7) and incident radiation ($IPAR_{i,DOY}$; Eq. 4.7). Most outlying points are located below the 1-to-1 line (Figure 4.10), such that the topographically corrected downscaling produces smaller α values than the simple downscaling. Smaller $\alpha_{topo_corrected}$ values than α_{simple} indicate that there exists significant positive covariance between sub-grid $IPAR_{i,DOY}$ and $NDVI_{i,DOY}$ values (Eq. 4.7) within the MODIS pixels. On the contrary, larger $\alpha_{topo_corrected}$ values are expected in MODIS pixels with significant negative covariance between sub-grid $IPAR_{i,DOY}$ and $NDVI_{i,DOY}$.

Temporal patterns of $\alpha_{topo_corrected}$ and α_{simple} parameters help to understand the effects of the topographically corrected downscaling. Figure 4.11 shows temporal patterns of the two α parameters at 5-day intervals from 2001 to 2008. Vertical lines represent 5th and 95th percentiles in terms of their spatial variations. Both α parameters remain stable during a maturity period (summer) with narrow ranges of spatial variations. Slightly increasing patterns are found during this period, as both MODIS and Landsat NDVI have a minor decrease by leaf color changes (Figure 4.2; Figure 4.5), but the fitted MODIS model does not represent this decrease. More fluctuating interannual patterns of both α parameters are observed during transition periods. Note that the α parameters compensate phenological discrepancy between composite Landsat NDVI images and fitted MODIS FPAR while preserving sub-grid variability. Therefore, it is quite clear that those values are more temporally variable during the greenup/senescence periods, when major interannual phenological variations may occur.

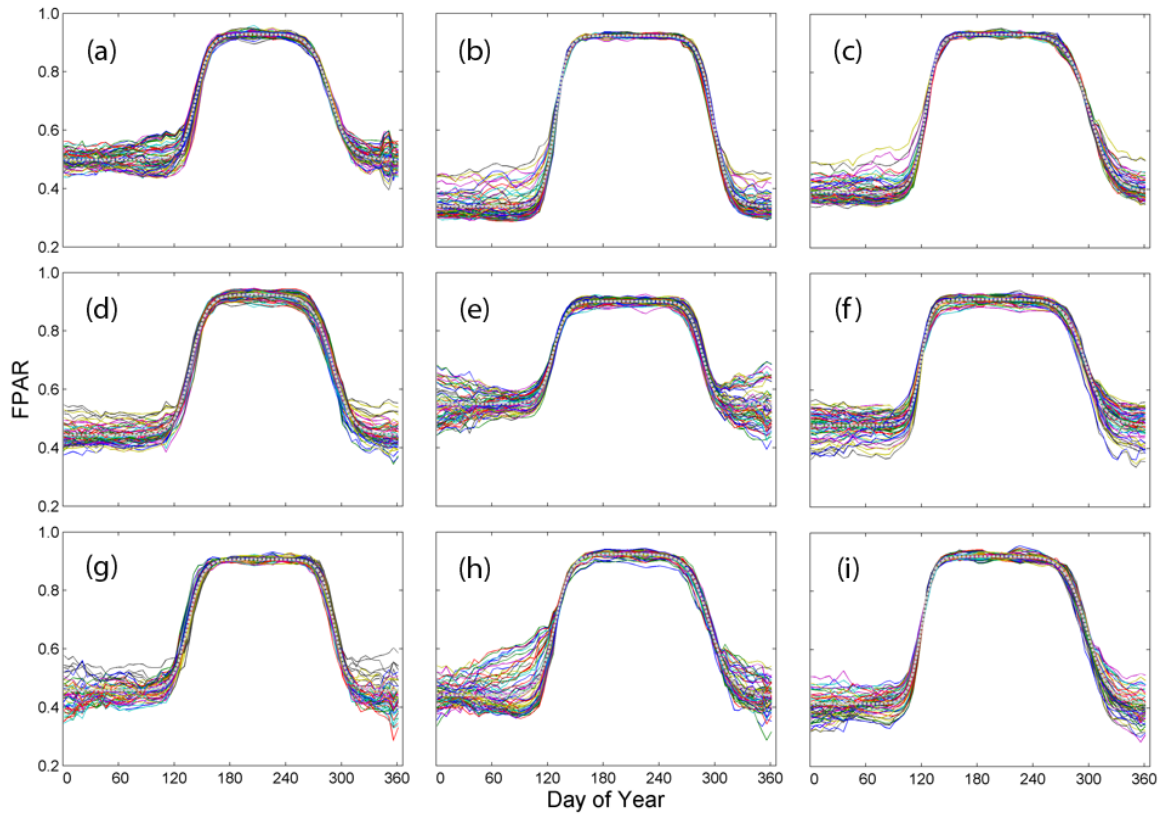


Figure 4.8: Examples of the topographically corrected downscaling for the MODIS FPAR at selected MODIS pixels in 2008 ((a) ~ (i); Figure 4.1). Grey dotted and color solid lines represent the fitted MODIS FPAR and the downscaled sub-grid FPAR values respectively.

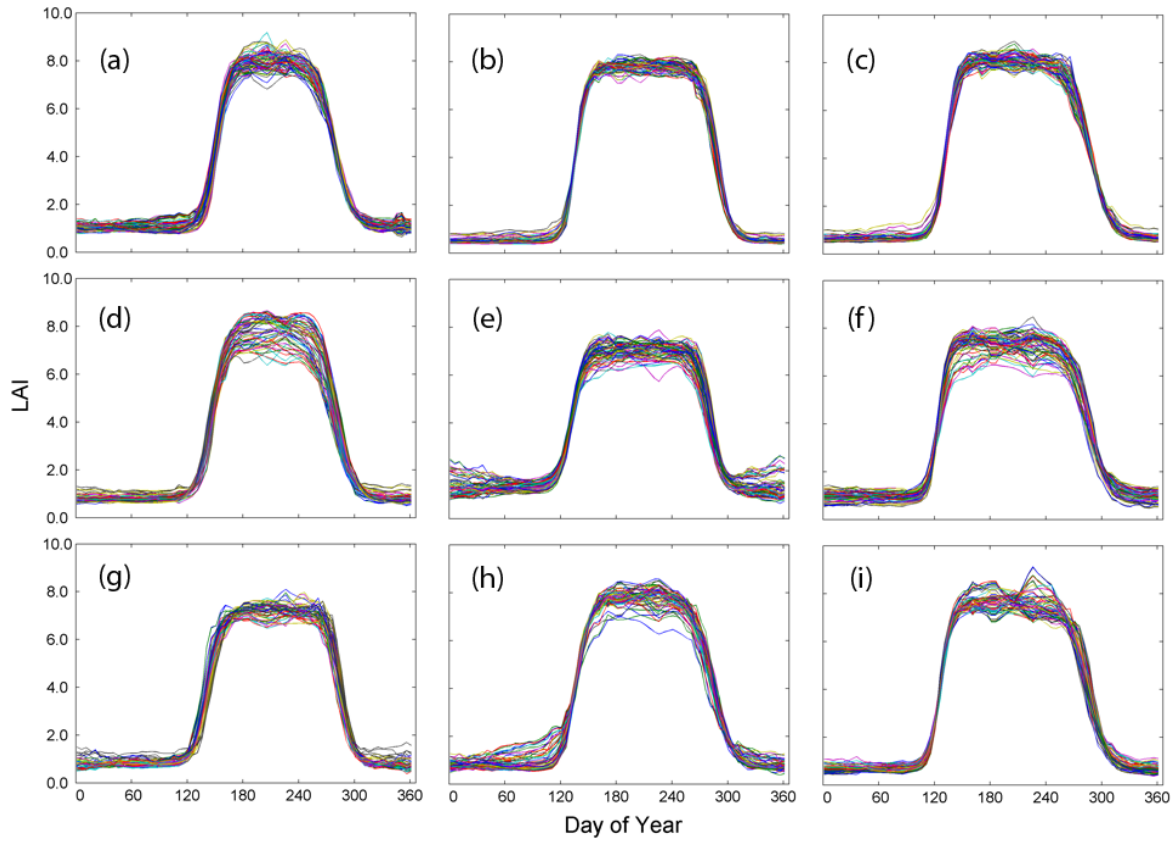


Figure 4.9: Examples of the topographically corrected downscaling at selected MODIS pixels in 2008 ((a) ~ (i); Figure 4.1). Color solid lines represent the downscaled sub-grid LAI values estimated from downscaled sub-grid FPAR values (Figure 4.8).

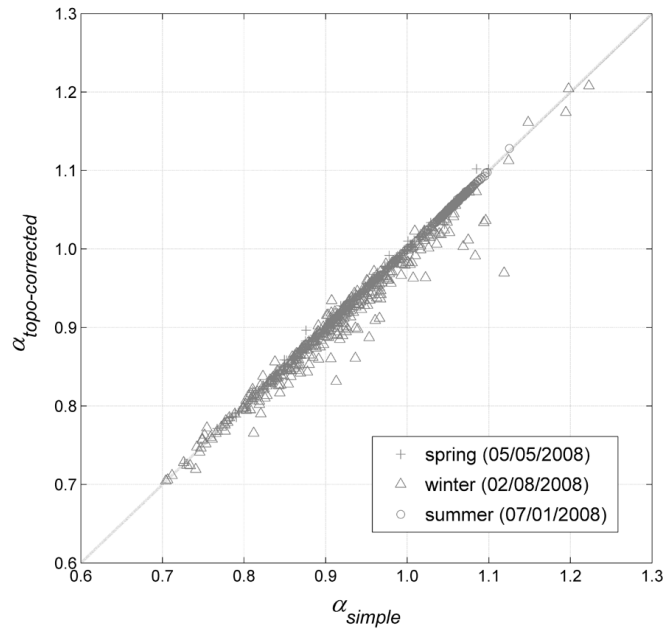


Figure 4.10: A scatter plot between $\alpha_{topo_corrected}$ (a proportionality parameter in the topographically corrected downscaling) and α_{simple} (a proportionality parameter in the simple downscaling) values on May 5 (cross), February 8 (triangle), and July 1 (circle), 2008.

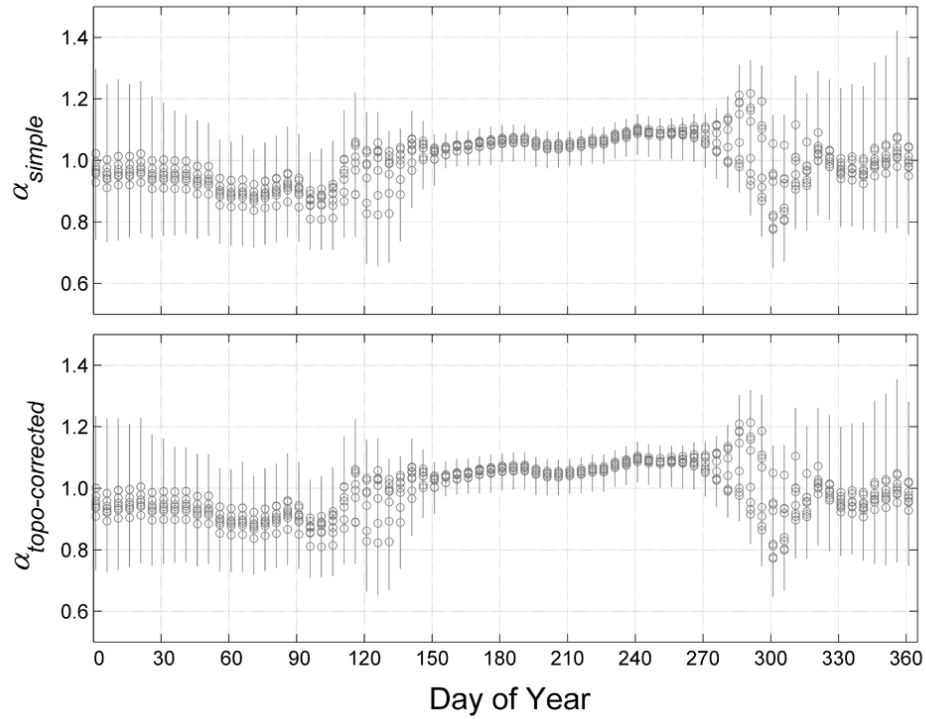


Figure 4.11: Temporal patterns of $\alpha_{topo_corrected}$ (upper) and α_{simple} (lower) values for a simulation period (2001 ~ 2008) with 5-day intervals. Points and vertical lines represent average, and 5th and 95th percentiles of spatial distributions in the study site ($n = 369$) on the same DOY each year. Note that α parameters are calculated each day, not each DOY.

The effects of the topographically corrected downscaling are evident only during the dormancy period (winter), already seen in Figure 4.10. Spatial variation of both α parameters increase in the middle of winter (Figure 4.11) with slightly reduced ranges in the topographically corrected downscaling. As mentioned earlier, these effects of the topographically corrected downscaling during the winter are due to positive covariance between sub-grid incident PAR and composite NDVI values, as well as increased sub-grid variability of incident PAR with a high sun zenith angle. This indicates greater evergreen species on south-facing slopes in the study site. Increased spatial variations of both α parameters in the middle of winter are also derived from systematic increases in the spatial variation of composite Landsat NDVI values (Figure 4.5).

4.4.4 *An example of distributed hydrological modeling*

Figure 4.12 shows observed and simulated daily streamflow within the study watershed from 2001 with integration of downscaled LAI, including the three-year calibration period (October 2003 ~ September 2006). The maximum efficiency value of the calibration period is 0.815, whereas that of the whole simulation period (January 2000 ~ February 2007) is 0.789. Note that precipitation is relatively even in this region throughout the year. For this reason, strong seasonal fluctuations of streamflow depend on phenological patterns of vegetation. The simulated level of low flows smoothly follows observed patterns without a seasonal bias, which indicates a seasonal pattern of evapotranspiration is well simulated by integrating vegetation dynamics downscaled from the real-time global satellite products. Note that simulated streamflow still misses some peak flows especially during the low flow periods. This is mainly because the steady-state assumption of TOPMODEL fails during summer storm periods (Beven 1997). The development of perched water tables in the study area with steep topography (Hewlett 1961) limits the validity of topographic index-based approach.

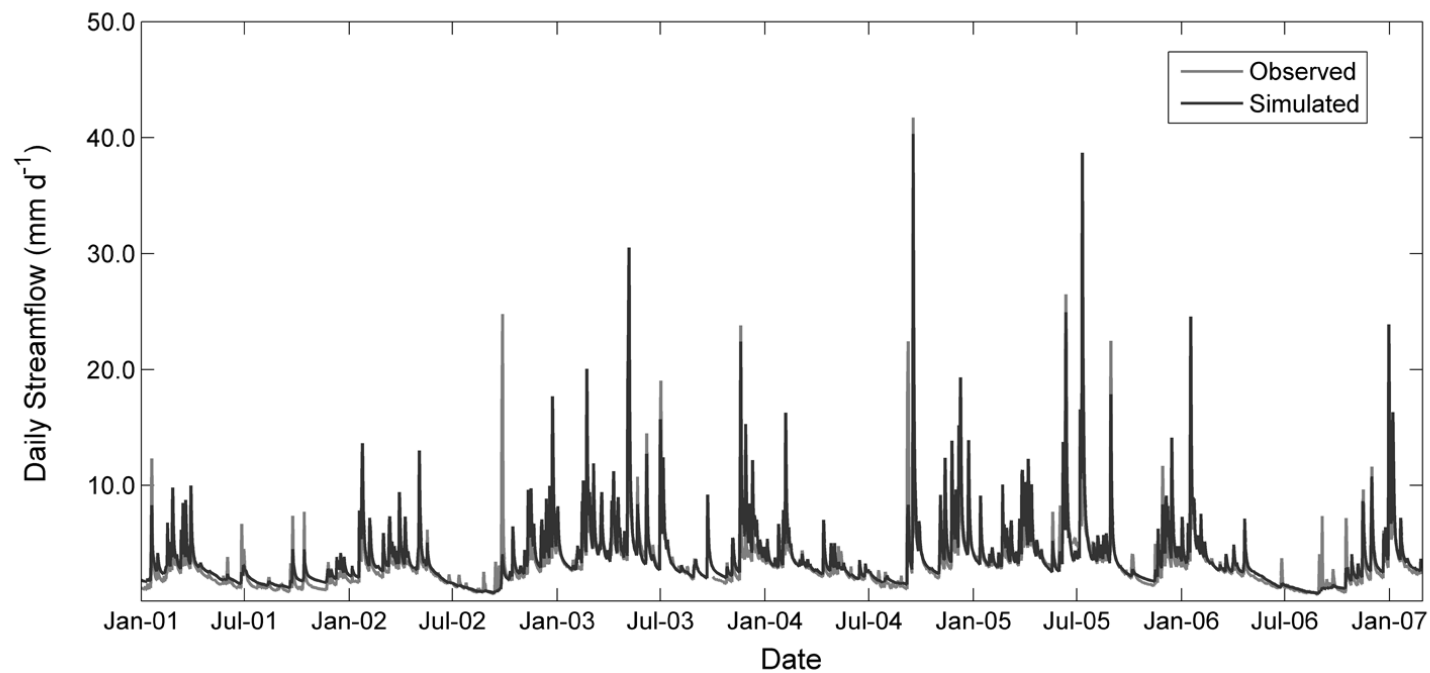


Figure 4.12: Observed and simulated daily streamflow at the study watershed (WS08; Figure 4.1), including the 3-year calibration period (October 2003 ~ September 2006).

Note that the improvement in prediction of watershed streamflow compared to a simulation that uses a constant (spatially invariant) phenology is small as long as the spatial mean interannual phenology is specified. However, we expect the significance of including spatially and temporally varying phenology will be much greater for spatial patterns of canopy and subcatchment response. This will be investigated in the future.

4.5 Discussion and conclusions

4.5.1 General discussion

In this study, we suggest two downscaling methods of near real-time MODIS FPAR to sub-grid scale, where sub-grid variability is estimated from composite Landsat TM NDVI images on corresponding DOY. Fusing the MODIS FPAR with the Landsat NDVI overcomes temporal and spatial limitations of both Landsat TM and MODIS image sets for the application to catchment-scale distributed hydrological modeling. Integration of sub-grid variability of potential incident radiation during the downscaling process may improve some downscaled results only in the winter, when substantial sub-grid variability of incident radiation and positive covariance between sub-grid incident radiation and NDVI are expected in this study site. As evaporation and transpiration processes are minimal during the winter season, there is no significant advantage of the topographically corrected downscaling compared to the simple downscaling for distributed hydrological modeling even in topographically complex terrain.

The spatio-temporal consistency of NDVI values provides an advantage in the downscaling process of vegetation dynamics over reflectance especially in topographically complex terrain. The ‘ratioing’ property of NDVI especially has an advantage in terms of spatial consistency as it cancels out a large portion of the multiplicative noise from illumination differences, cloud shadows, topographic variations, and atmospheric conditions. As mentioned earlier, MODIS

NDVI (Figure 4.2) and Landsat NDVI (Figure 4.5) values are very consistent in terms of spatial and temporal variations, as well as interannual phenological variations (Figure 4.4 and Figure 4.5).

There are slight discrepancies between maximum and minimum NDVI values from Landsat and MODIS images, which may be attributed to differences in corresponding bandwidths (Table 4.1) (Gupta *et al.* 2000; Teillet *et al.* 2007) or atmospheric correction methods (Vermote *et al.* 1997). Many studies of multi-sensor comparison of NDVI values report that both Landsat and MODIS NDVI values are comparable within a very close range, though it seems that the MODIS NDVI is slightly higher than Landsat NDVI (Huete *et al.* 2002; Gao *et al.* 2003; Morisette *et al.* 2004; Brown *et al.* 2006; Cheng 2006). Another possible explanation of the discrepancy between MODIS and Landsat NDVI values is a scale variant nature of NDVI. We address this issue later in the discussion.

The study area is located in a high-precipitation region (around 2000 mm y⁻¹), so available cloud-free images are quite limited by cloud contamination. Therefore, a post-processing analysis for MODIS NDVI values (filtering and fitting) is necessary, even after removal of unqualified data points with quality assurance flags at each MODIS pixel. In addition, the number of cloud-free Landsat images is limited, although the study site is located in overlapping regions between two paths of Landsat orbits. This is a major reason why composite NDVI images on corresponding DOY (over multiple years), not on corresponding dates, are used in the downscaling process. If enough Landsat NDVI images were available in each year, fluctuations of the α parameters during transition periods would have been reduced (Figure 4.11). In addition, if reasonable spatio-temporal patterns of MODIS NDVI values were available without the post-processing analysis, more stable patterns of the α parameters would have been expected during maturity and dormancy periods (Figure 4.11).

4.5.2 The FPAR-NDVI relationship

This study is based on a simple linear assumption between NDVI and FPAR, represented as proportionality parameters (α ; Eq. 4.5). This linear relationship is known to be a function of biome types and forest structures (Knyazikhin *et al.* 1998; Myneni *et al.* 1997). Eq. 4.5 explicitly assumes that sub-grid variability of FPAR within the MODIS pixel is linearly proportional to sub-grid NDVI values. Therefore, if there are different biome and land cover types within a MODIS pixel, this assumption fails. This is a reason why spatially discrete patterns of α parameters (Figure 4.6c) and downscaled FPAR values (Figure 4.6d, f) are found around the Coweeta basin outlet, where grass and open space for lab facilities are located. There are also two plantation conifer watersheds (WS01, WS17; Figure 4.1) and open fields outside the northern boundaries of the Coweeta basin. Distinct patterns in downscaled FPAR around these regions are more recognizable in summer (Figure 4.7e) and winter (Figure 4.7f), when fully-grown deciduous forests are distinct in Landsat NDVI images (Figure 4.7c, d).

Following Knyazikhin *et al.* (1998), this simple proportional assumption between NDVI and FPAR is valid only if the canopy background is ideally black. Other model studies also found that this linear relationship between NDVI and FPAR is very consistent with respect to various canopy and optical properties (e.g. clumping, canopy cover, leaf angle distribution, spatial heterogeneity, and solar zenith angle etc.), but sensitive to soil background reflectance (e.g. Asrar *et al.* 1992; Myneni and Williams 1994). However, many studies of field-measured FPAR and Landsat NDVI values show that estimated intercept values of the linear NDVI-FPAR relationship are not actually zero, but usually slightly negative under non-ideal soil background color (e.g. Asrar *et al.* 1984, 1992; Goward *et al.* 1994; Friedl *et al.* 1995). This means that sub-grid variability based on Eq. 4.5 might be underestimated and actual proportionality parameters (Eq. 4.6 and 4.7) might be slightly larger than estimated in this study. In similar biome types, the above studies have also reported slightly larger slope values of the linear NDVI-FPAR relationship with negative intercepts across different images (Myneni and Williams 1994; Myneni *et al.* 1997, 2002) than the estimated range of α parameters in this study (Figure 4.11). In addition,

the linear assumption between NDVI and FPAR may not be supported especially when canopy stand structure is gappy (e.g. Song and Band 2004). However, it should not be a big issue in this study site, where upper canopy is dominant with broadleaf closed forest.

Sub-grid FPAR values are a better indicator for sub-grid variability of the MODIS FPAR than sub-grid NDVI values. Note that the α parameter in this study (Eq. 4.5) includes both the linear NDVI-FPAR relationship, as well as proportional phenological discrepancy between near real-time MODIS FPAR and composite Landsat NDVI on corresponding DOY. Separating these two relationships can be a possible solution for the problem in applying α parameter directly to composite Landsat NDVI values. The sub-grid FPAR can be estimated first from the composite Landsat NDVI image, and then a proportionality parameter can be applied to sub-grid FPAR values rather than to NDVI directly. In this approach, α parameter solely represents phenological discrepancy between MODIS and Landsat FPAR values. This approach can also provide more flexibility in the application of these downscaling methods into regions with mixed biome and land cover types by applying different NDVI-FPAR relationships for different land cover and biome types. However, it would be another issue to properly estimate the linear relationship between FPAR and NDVI in different biome and land cover types.

4.5.3 *Scale invariance in sub-grid variability*

The limited effect of the topographically corrected downscaling means that FPAR may not be scale invariant during the winter season in this study area (Eq. 4.3 and 4.4). A simple test of scale invariance of NDVI between Landsat and MODIS scales may give an idea how different NDVI values are affected by different spatial aggregation methods. It also may provide a possible explanation of the discrepancy of maximum and minimum NDVI values between Landsat and MODIS scales. The scale invariance of NDVI between Landsat and MODIS scales can be tested by comparing between the mean NDVI ($NDVI_{avg}$) of sub-grid Landsat NDVI within a single

MODIS pixel and the lumped NDVI ($NDVI_{lump}$) from aggregated radiance at the MODIS scale. In the same way, the scale invariance of FPAR can be checked by comparing Eq. 4.3 and 4.4 values. If α parameters (Eq. 4.5) are assumed to be constant at each sub-grid pixel (homogeneous land cover and biome types), this test results in the comparison between $NDVI_{avg}$ (Eq. 4.3) and the weighted mean of sub-grid NDVI ($NDVI_i$) with respect to sub-grid incoming radiation ($IPAR_i$). It can be rewritten from Eq. 4.4 and 4.5 without the time function (DOY and t) as

$$NDVI_{wgt} = \frac{\sum_{i=1}^n (NDVI_i \cdot IPAR_i)}{\sum_{i=1}^n IPAR_i} \quad (4.8)$$

Figure 4.13a shows a scatter plot between $NDVI_{avg}$ and $NDVI_{lump}$, and the temporal patterns of relative difference between them in the study site ($n = 369$). NDVI is definitely not scale invariant in the middle of winter season, when $NDVI_{avg}$ underestimates $NDVI_{lump}$. This test presents a possibility that the mean Landsat NDVI can be slightly lower than the lumped MODIS NDVI in the middle of winter in the study site. Note that systematic decreases of the mean Landsat NDVI in the middle of winter are observed in this study (Figure 4.5), but not recognized in the filtered MODIS NDVI (Figure 4.2).

Figure 4.13b shows a scatter plot between $NDVI_{avg}$ and $NDVI_{wgt}$, and the temporal patterns of relative difference between them in the study site ($n = 369$). They shows similar pattern to the relation between $NDVI_{avg}$ and $NDVI_{lump}$, so FPAR is not scale invariant during the winter season. Note that larger α_{simple} values (Eq. 4.6) than $\alpha_{topo_corrected}$ values (Eq. 4.7) in the winter (Figure 4.10) already analytically supports the overestimation of $NDVI_{wgt}$ compared to $NDVI_{avg}$.

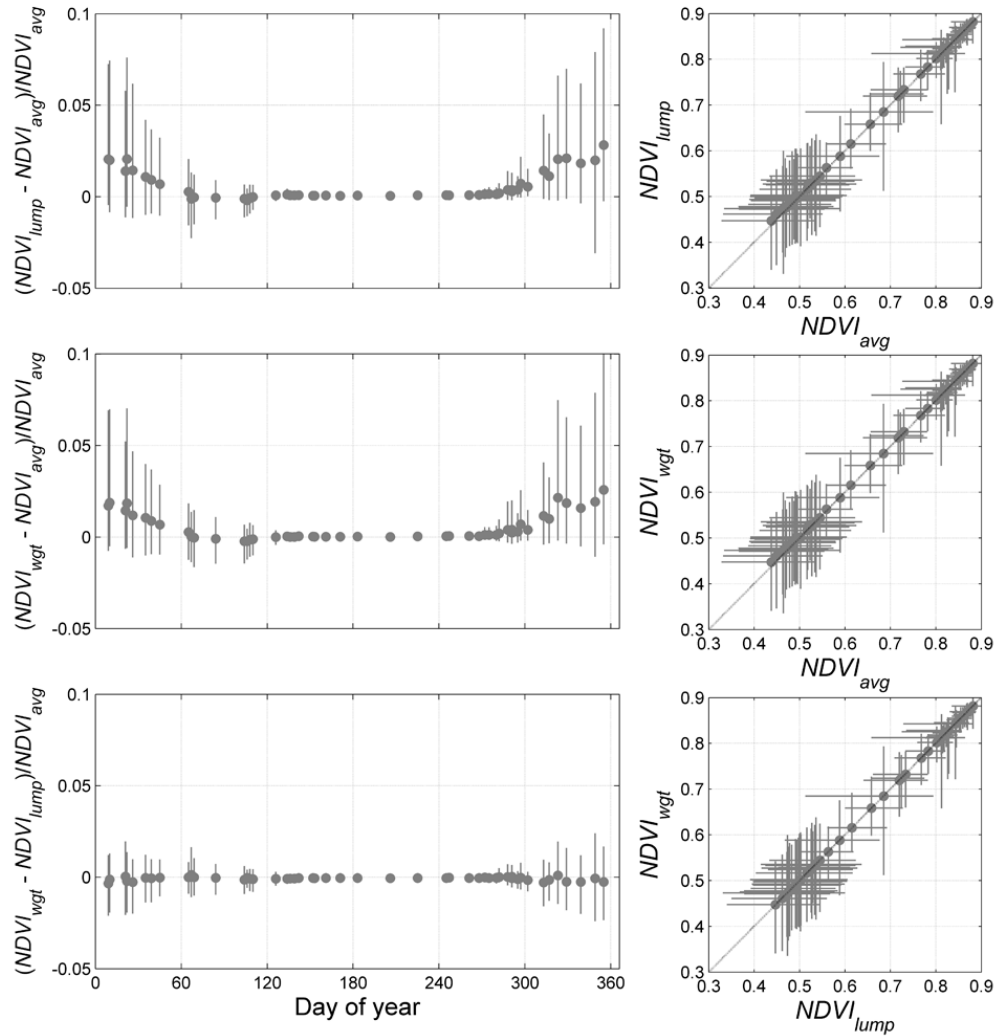


Figure 4.13: Temporal patterns of relative differences (left column) and scatter plots (right column) between (a) $NDVI_{avg}$ and $NDVI_{lump}$, (b) $NDVI_{avg}$ and $NDVI_{wgt}$, and (c) $NDVI_{lump}$ and $NDVI_{wgt}$. $NDVI_{lump}$ is the NDVI calculated from aggregated radiance at the MODIS scale. $NDVI_{avg}$ is the averaged NDVI at MODIS scale from sub-grid Landsat NDVI values. $NDVI_{wgt}$ is the weighted averaged NDVI with respect to sub-grid incoming radiance (Eq. 4.8). Horizontal and vertical lines represent 5th and 95th percentiles of the spatial NDVI values within the WS08 watershed ($n = 8654$; Figure 4.1).

The temporal patterns of relative difference between $NDVI_{avg}$ and $NDVI_{lump}$ (Figure 4.13a), and between $NDVI_{avg}$ and $NDVI_{wgt}$ (Figure 4.13b) show that these relative differences are very similar on corresponding dates. Therefore, there seems little relative difference between $NDVI_{lump}$ and $NDVI_{wgt}$ (Figure 4.13c) even in winter season, when only increased spatial variances are observed. Therefore, we can derive this relationship from Eq. 4.4 and 4.5.

$$FPAR = \alpha \cdot NDVI_{wgt} \approx \alpha \cdot NDVI_{lump} \quad (4.9)$$

where $FPAR$ represents the integrated FPAR at the MODIS scale. Eq. 4.9 indicates that the same α parameter between FPAR and NDVI is applied both at the sub-grid scale (Eq. 4.5) and at the MODIS scale. Therefore, the linear NDVI-FPAR relationship may be scale invariant in the study site, though FPAR and NDVI is not scale invariant.

Previous studies of the scale invariance of NDVI show conflicting results whether the lumped NDVI calculated from aggregated reflectance is larger than the averaged NDVI (Hall *et al.* 1992; Friedl *et al.* 1995). Hu and Islam (1997) proved that the difference between lumped and averaged NDVI was dependent on the variances of the red and near-infrared band radiances and the covariance between two radiances using a Taylor series approximation. Eq. 4.4 shows that the scale invariance of FPAR is only dependent on the covariance between $IPAR_{i,DOY}$ and $NDVI_{i,DOY}$ in Eq. 4.8, but not on each variance term. The similarity between $NDVI_{lump}$ and $NDVI_{wgt}$ (Figure 4.13c) indicates the scale invariance of NDVI is only dependent on the covariance between $IPAR_{i,DOY}$ and $NDVI_{i,DOY}$ within a coarse pixel in the regions with homogeneous land cover and biome types.

In this study, the linear NDVI-FPAR relationship is estimated by matching 1-km MODIS NDVI (MOD13A2) and FPAR (MOD15A2) in the study area. This relationship is used to derive 250-m MODIS FPAR from 250-m MODIS NDVI (MOD13Q1). Tian *et al.* (2002a) examined the scale-dependent property of the MODIS NDVI and LAI algorithms and they found that MODIS

LAI is not scale invariant between 250 m and 1 km while the mean of MODIS NDVI changed little with different spatial resolutions. Tian *et al.* (2002b) also found that LAI retrieval errors at coarse resolutions are proportional to sub-pixel heterogeneity in land cover especially mixed with non-forest biome types. However, Friedl *et al.* (1995) pointed out that the linear NDVI-FPAR relationship was little affected by aggregating NDVI and FPAR unlike the non-linear NDVI-LAI relationship due to its linearity. In this sense, several studies using three-dimensional radiation transfer models pointed out that the linear NDVI-FPAR relationship is scale invariant by comparing estimated relationships from homogeneous and heterogeneous canopy (Myneni and Williams 1994; Myneni *et al.* 1995). Moreover, the study area is represented as relatively homogeneous land cover as deciduous broadleaf forests with closed canopy and well mixed colluvial soils. Therefore, the assumption of scale invariance of the linear NDVI-FPAR relationship may be valid in the study area.

4.5.4 Topographic correction

Some gradual decreases in average Landsat NDVI values are found during the winter season with increased spatial variation (Figure 4.5). These patterns result in increases of average α parameters and their spatial variation in the middle of winter (Figure 4.11). Several studies reported that NDVI is not significantly affected by different topographic correction methods (Ekstrand 1996; Turner *et al.* 1999; Matsushita *et al.* 2007) because the ‘ratioing’ property of NDVI can effectively normalize illumination differences on different slopes. However, most of these studies were done with images with low sun zenith angles. Vincini *et al.* (2002) reported that NDVI calculation from topographically uncorrected Landsat TM led to systematic underestimation of NDVI values especially in areas with high illumination angles.

In this study area, the sun illumination angles (Teillet *et al.* 1982) on north-facing slopes are over 90° in the middle of winter, where diffuse radiation dominates. This fact makes it hard to

apply the cosine-based topographic correction method with Lambertian (Teillet *et al.* 1982; Civco 1989) and non-Lambertian assumptions (Minnaert 1941) for these Landsat data sets. These cosine-based topographic correction methods were known to overly correct in faintly illuminated areas with very low illumination angle (Meyer *et al.* 1993), so modified methods with additive terms were proposed to solve this problem (e.g. the C correction method; Teillet *et al.* 1982, and the Gamma method; Shepherd and Dymond 2003). However, the modified cosine-based methods with additive terms could not produce the proper range of NDVI values in this study even though they can solve systematic decrease of average Landsat NDVI values around the winter solstice.

For this reason, it is hard to find a consistent topographic correction method through the year. The effect of topographic correction for the NDVI calculation is more evident when sun zenith angle is high. Also, it seems that separation of direct and diffuse radiation during the process of topographic correction (Shepherd and Dymond 2003) is quite necessary for winter images because faint diffuse radiation is dominant at slopes with high illumination angles.

4.5.5 Conclusions

NDVI has rarely been used as an indicator of sub-grid variability mainly because NDVI is usually regarded as not scale invariant (Hu and Islam 1997). However, incorporation of FPAR as a downscaling variable can solve the scale invariance problem of NDVI, because FPAR is more physically meaningful and more easily scalable between different spatial resolutions. Moreover, the linear NDVI-FPAR relationship in homogeneous regions is shown to be scale invariant in this study, which facilitates its use as a measure of sub-grid variability. In this study, the fitted MODIS FPAR is downscaled into the Landsat scale with two suggested downscaled methods (the simple and the topographically corrected downscaling) for the 8-year period (2001 ~ 2008). The relationship between the downscaled MODIS FPAR and the composite sub-grid NDVI values is represented with a simple linear proportionality parameter, which includes the linear relationship

between sub-grid NDVI and FPAR, as well as proportional phenological discrepancy between the MODIS FPAR and composite Landsat NDVI on corresponding DOY. The sub-grid variability of vegetation density on each day is estimated from composite NDVI images as a function of DOY. In the topographically corrected downscaling, the sub-grid variability of potential incoming radiation is calculated in conjunction with digital elevation data, and used to weight average sub-grid NDVI values. The effects of the topographically corrected downscaling is quite limited with the exception of winter when there is positive covariance between sub-grid incident PAR and composite NDVI values, as well as increased sub-grid variability of incident PAR with a high sun zenith angle. Suggested downscaling methods are applicable only to relatively homogeneous landscapes due to the simple linear assumption between sub-grid NDVI and incoming FPAR. However, if different NDVI-FPAR relationships can be estimated in different land cover and biome types, these methods are also extendable into heterogeneous landscapes. Combining the spatial resolution of Landsat and the temporal resolution of MODIS can make it possible to compromise between limitations of both image sets in applications of global satellite products into distributed hydrological modeling at local scale. Furthermore, this study provides the potential for ecohydrological nowcasts and forecasts at the catchment scale with integration of near real-time global satellite products by downscaling techniques.

Acknowledgements

The research represented in this paper was supported by the National Science Foundation award to the Coweeta Long Term Ecologic Research project (DEB #0823293). All streamflow and climate data were made available from the Coweeta Hydrological Laboratory and LTER, which is supported by the National Science Foundation and the USDA Forest Service. We specifically thank Dr. Jim Vose for the support in providing climate data in the Coweeta

Hydrologic Lab. This paper is co-authored by Dr Lawrence E. Band and Dr. Conghe Song. Dr. L. E. Band provided overall directions to this research study as a dissertation advisor and gave insights toward data analysis and interpretation. Dr. C. Song was involved in the atmospheric correction of Landsat TM images and discussion of downscaling methods.

References

- Andreadis KM, Lettenmaier DP (2006) Assimilating remotely sensed snow observations into a macroscale hydrology model. *Advances in Water Resources*, **29**, 872-886.
- Asner GP, Scurlock JMO, Hicke JA (2003) Global synthesis of leaf area index observations: implications for ecological and remote sensing studies. *Global Ecology and Biogeography*, **12**, 191-205.
- Asrar G, Fuchs M, Kanemasu ET, Hatfield JL (1984) Estimating Absorbed Photosynthetic Radiation and Leaf-Area Index from Spectral Reflectance in Wheat. *Agronomy Journal*, **76**, 300-306.
- Asrar G, Myneni RB, Choudhury BJ (1992) Spatial Heterogeneity in Vegetation Canopies and Remote-Sensing of Absorbed Photosynthetically Active Radiation - a Modeling Study. *Remote Sensing of Environment*, **41**, 85-103.
- Avisar R (1992) Conceptual Aspects of a Statistical-Dynamic Approach to Represent Landscape Subgrid-Scale Heterogeneities in Atmospheric Models. *Journal of Geophysical Research-Atmospheres*, **97**, 2729-2742.
- Band LE (1993) Effect of Land-Surface Representation on Forest Water and Carbon Budgets. *Journal of Hydrology*, **150**, 749-772.
- Band LE, Moore ID (1995) Scale - Landscape Attributes and Geographical Information-Systems. *Hydrological Processes*, **9**, 401-422.
- Band LE, Patterson P, Nemani R, Running SW (1993) Forest ecosystem processes at the watershed scale: incorporating hillslope hydrology. *Agricultural and Forest Meteorology*, **63**, 93-126.
- Band LE, Peterson DL, Running SW, Coughlan J, Lammers R, Dungan J, Nemani R (1991) Forest Ecosystem Processes at the Watershed Scale - Basis for Distributed Simulation. *Ecological Modelling*, **56**, 171-196.
- Beven K (1997) TOPMODEL: A critique. *Hydrological Processes*, **11**, 1069-1085.
- Bronstert A, Bardossy A (1999) The role of spatial variability of soil moisture for modelling surface runoff generation at the small catchment scale. *Hydrology and Earth System Sciences*, **3**, 505-516.
- Brown ME, Pinzon JE, Didan K, Morisette JT, Tucker CJ (2006) Evaluation of the consistency of long-term NDVI time series derived from AVHRR, SPOT-Vegetation, SeaWiFS, MODIS,

- and Landsat ETM+ sensors. *IEEE Transactions on Geoscience and Remote Sensing*, **44**, 1787-1793.
- Chavez PS (1996) Image-based atmospheric corrections revisited and improved. *Photogrammetric Engineering and Remote Sensing*, **62**, 1025-1036.
- Chen JM (1996) Canopy architecture and remote sensing of the fraction of photosynthetically active radiation absorbed by boreal conifer forests. *IEEE Transactions on Geoscience and Remote Sensing*, **34**, 1353-1368.
- Cheng Q (2006) Multisensor comparisons for validation of MODIS vegetation indices. *Pedosphere*, **16**, 362-370.
- Civco DL (1989) Topographic Normalization of Landsat Thematic Mapper Digital Imagery. *Photogrammetric Engineering and Remote Sensing*, **55**, 1303-1309.
- Cleugh HA, Leuning R, Mu QZ, Running SW (2007) Regional evaporation estimates from flux tower and MODIS satellite data. *Remote Sensing of Environment*, **106**, 285-304.
- Day FP, Philips DL, Monk CD (1988) Forest communities and patterns. In: *Forest Hydrology and Ecology at Coweeta* (eds Swank WT, Crossley JDA), pp. 141-149. Springer-Verlag, New York, NY, USA.
- Day FP, Monk CD (1974) Vegetation Patterns on a Southern Appalachian Watershed. *Ecology*, **55**, 1064-1074.
- Didan K, Huete A (2006) MODIS Vegetation Index Product Series Collection 5 Change Summary.
- Ekstrand S (1996) Landsat TM-based forest damage assessment: Correction for topographic effects. *Photogrammetric Engineering and Remote Sensing*, **62**, 151-161.
- Entekhabi D, Eagleson PS (1989) Land surface hydrology parameterization for atmospheric general circulation models including subgrid scale spatial variability. *Journal of Climate*, **2**, 816-31.
- Famiglietti JS, Devereaux JA, Laymon CA, et al (1999) Ground-based investigation of soil moisture variability within remote sensing footprints during the Southern Great Plains 1997 (SGP97) Hydrology Experiment. *Water Resources Research*, **35**, 1839-1851.
- Famiglietti JS, Wood EF (1994) Multiscale Modeling of Spatially-Variable Water and Energy-Balance Processes. *Water Resources Research*, **30**, 3061-3078.
- Fisher JI, Mustard JF (2007) Cross-scalar satellite phenology from ground, Landsat, and MODIS data. *Remote Sensing of Environment*, **109**, 261-273.
- Fisher JI, Mustard JF, Vadeboncoeur MA (2006) Green leaf phenology at Landsat resolution: Scaling from the field to the satellite. *Remote Sensing of Environment*, **100**, 265-279.

- Friedl MA, Davis FW, Michaelsen J, Moritz MA (1995) Scaling and uncertainty in the relationship between the NDVI and land surface biophysical variables: An analysis using a scene simulation model and data from FIFE. *Remote Sensing of Environment*, **54**, 233-246.
- Gao F, Masek J, Schwaller M, Hall F (2006) On the blending of the Landsat and MODIS surface reflectance: Predicting daily Landsat surface reflectance. *IEEE Transactions on Geoscience and Remote Sensing*, **44**, 2207-2218.
- Gao X, Huete AR, Didan K (2003) Multisensor comparisons and validation of MODIS vegetation indices at the semiarid Jornada experimental range. *IEEE Transactions on Geoscience and Remote Sensing*, **41**, 2368-2381.
- Goward SN, Waring RH, Dye DG, Yang JL (1994) Ecological Remote-Sensing at Otter - Satellite Macroscale Observations. *Ecological Applications*, **4**, 322-343.
- Gower ST, Krankina O, Olson RJ, Apps M, Linder S, Wang C (2001) Net primary production and carbon allocation patterns of boreal forest ecosystems. *Ecological Applications*, **11**, 1395-1411.
- Grayson RB, Western AW, Chiew FHS, Blöschl G (1997) Preferred states in spatial soil moisture patterns: Local and nonlocal controls. *Water Resources Research*, **33**, 2897-2908.
- Gupta RK, Vijayan D, Prasad TS, Tirumaladevi NC (2000) Role of bandwidth in computation of NDVI from Landsat TM and NOAA AVHRR bands. *Remote Sensing for Land Surface Characterisation*, **26**, 1141-1144.
- Gutman G, Ignatov A (1998) The derivation of the green vegetation fraction from NOAA/AVHRR data for use in numerical weather prediction models. *International Journal of Remote Sensing*, **19**, 1533-1543.
- Hall FG, Huemmrich KF, Goetz SJ, Sellers PJ, Nickeson JE (1992) Satellite Remote-Sensing of Surface-Energy Balance - Success, Failures, and Unresolved Issues in Fife. *Journal of Geophysical Research-Atmospheres*, **97**, 19061-19089.
- Hewlett JD (1961) *Soil moisture as a source of base flow from steep mountain watersheds. Station Paper 132*, Southeast Forest Experimental Station, U.S. Department of Agriculture and Forest Service, Asheville, NC, USA.
- Hu Z, Islam S (1997) A framework for analyzing and designing scale invariant remote sensing algorithms. *IEEE Transactions on Geoscience and Remote Sensing*, **35**, 747-755.
- Huete A, Didan K, Miura T, Rodriguez EP, Gao X, Ferreira LG (2002) Overview of the radiometric and biophysical performance of the MODIS vegetation indices. *Remote Sensing of Environment*, **83**, 195-213.

- Hwang T, Band LE, Hales TC (2009) Ecosystem processes at the watershed scale: Extending optimality theory from plot to catchment. *Water Resources Research*, **45**, W11425.
- Hwang T, Kang S, Kim J, Kim Y, Lee D, Band L (2008) Evaluating drought effect on MODIS Gross Primary Production (GPP) with an eco-hydrological model in the mountainous forest, East Asia. *Global Change Biology*, **14**, 1037-1056.
- Johnson L, Meyerink A, Kline K (2009) *Landsat Thematic Mapper (TM) Level 1 (L1) Data Format Control Book (DFCB) Version 3.0. LS-DFCB-20*, Department of the Interior, U.S. Geological Survey, Sioux Falls, SD, USA.
- Kerkhoff AJ, Martens SN, Milne BT (2004) An ecological evaluation of Eagleson's optimality hypotheses. *Functional Ecology*, **18**, 404-413.
- Knyazikhin Y, Martonchik JV, Myneni RB, Diner DJ, Running SW (1998) Synergistic algorithm for estimating vegetation canopy leaf area index and fraction of absorbed photosynthetically active radiation from MODIS and MISR data. *Journal of Geophysical Research-Atmospheres*, **103**, 32257-32275.
- Lee DS, Storey JC, Choate MJ, Hayes RW (2004) Four years of Landsat-7 on-orbit geometric calibration and performance. *IEEE Transactions on Geoscience and Remote Sensing*, **42**, 2786-2795.
- Leuning R, Zhang YQ, Rajaud A, Cleugh H, Tu K (2008) A simple surface conductance model to estimate regional evaporation using MODIS leaf area index and the Penman-Monteith equation. *Water Resources Research*, **44**, W10419.
- Liang X, Lettenmaier DP, Wood EF (1996) One-dimensional statistical dynamic representation of subgrid spatial variability of precipitation in the two-layer variable infiltration capacity model. *Journal of Geophysical Research-Atmospheres*, **101**, 21403-21422.
- Liang X, Xie ZH (2001) A new surface runoff parameterization with subgrid-scale soil heterogeneity for land surface models. *Advances in Water Resources*, **24**, 1173-1193.
- Luce CH, Tarboton DG (2004) The application of depletion curves for parameterization of subgrid variability of snow. *Hydrological Processes*, **18**, 1409-1422.
- Luce CH, Tarboton DG, Cooley KR (1999) Sub-grid parameterization of snow distribution for an energy and mass balance snow cover model. *Hydrological Processes*, **13**, 1921-1933.
- Mackay DS (2001) Evaluation of hydrologic equilibrium in a mountainous watershed: incorporating forest canopy spatial adjustment to soil biogeochemical processes. *Advances in Water Resources*, **24**, 1211-1227.

- Matsushita B, Yang W, Chen J, Onda Y, Qiu GY (2007) Sensitivity of the Enhanced Vegetation Index (EVI) and Normalized Difference Vegetation Index (NDVI) to topographic effects: A case study in high-density cypress forest. *Sensors*, **7**, 2636-2651.
- Meyer P, Itten KI, Kellenberger T, Sandmeier S, Sandmeier R (1993) Radiometric Corrections of Topographically Induced Effects on Landsat Tm Data in an Alpine Environment. *Isprs Journal of Photogrammetry and Remote Sensing*, **48**, 17-28.
- Minnaert M (1941) The reciprocity principle in lunar photometry. *Astrophysical Journal*, **93**, 403-410.
- Morisette JT, Pinzon JE, Brown CJ, Tucker CJ, Justice CO, (2004) *Initial validation of NDVI time series from AVHRR, vegetation and MODIS*, http://gimms.gsfc.nasa.gov/Molly/pdf_files/Morisette_SPOT_AVHRR_MODIS_timeseries.pdf.
- Mu Q, Heinsch FA, Zhao M, Running SW (2007) Development of a global evapotranspiration algorithm based on MODIS and global meteorology data. *Remote Sensing of Environment*, **111**, 519-536.
- Myneni RB, Hoffman S, Knyazikhin Y, et al (2002) Global products of vegetation leaf area and fraction absorbed PAR from year one of MODIS data. *Remote Sensing of Environment*, **83**, 214-231.
- Myneni RB, Maggion S, Iaquinto J, et al (1995) Optical Remote-Sensing of Vegetation - Modeling, Caveats, and Algorithms. *Remote Sensing of Environment*, **51**, 169-188.
- Myneni RB, Nemani RR, Running SW (1997) Estimation of global leaf area index and absorbed par using radiative transfer models. *IEEE Transactions on Geoscience and Remote Sensing*, **35**, 1380-1393.
- Myneni RB, Williams DL (1994) On the Relationship between FAPAR and NDVI. *Remote Sensing of Environment*, **49**, 200-211.
- Nash JE, Sutcliffe JV (1970) River flow forecasting through conceptual models part I — A discussion of principles. *Journal of Hydrology*, **10**, 282-290.
- Nishida K, Nemani RR, Running SW, Glassy JM (2003) An operational remote sensing algorithm of land surface evaporation. *Journal of Geophysical Research-Atmospheres*, **108**, 4270.
- Pan M, Wood EF, Wojcik R, McCabe MF (2008) Estimation of regional terrestrial water cycle using multi-sensor remote sensing observations and data assimilation. *Remote Sensing of Environment*, **112**, 1282-1294.
- Pohl C, van Genderen JL (1998) Multisensor image fusion in remote sensing: concepts, methods and applications. *International Journal of Remote Sensing*, **19**, 823-854.

- Rodrigueziturbe I, Entekhabi D, Bras RL (1991) Nonlinear Dynamics of Soil-Moisture at Climate Scales .1. Stochastic-Analysis. *Water Resources Research*, **27**, 1899-1906.
- Roy DP, Ju J, Lewis P, Schaaf C, Gao F, Hansen M, Lindquist E (2008) Multi-temporal MODIS-Landsat data fusion for relative radiometric normalization, gap filling, and prediction of Landsat data. *Remote Sensing of Environment*, **112**, 3112-3130.
- Running SW, Nemani RR, Hungerford RD (1987) Extrapolation of synoptic meteorological data in mountainous terrain and its use for simulating forest evapotranspiration and photosynthesis. *Canadian Journal of Forest Research-Revue Canadienne De Recherche Forestiere*, **17**, 472-483.
- Ryu D, Famiglietti JS (2005) Characterization of footprint-scale surface soil moisture variability using Gaussian and beta distribution functions during the Southern Great Plains 1997 (SGP97) hydrology experiment. *Water Resources Research*, **41**, W12433.
- Sellers PJ (1985) Canopy Reflectance, Photosynthesis and Transpiration. *International Journal of Remote Sensing*, **6**, 1335-1372.
- Shepherd JD, Dymond JR (2003) Correcting satellite imagery for the variance of reflectance and illumination with topography. *International Journal of Remote Sensing*, **24**, 3503-3514.
- Song C, Woodcock CE, Seto KC, Lenney MP, Macomber SA (2001) Classification and change detection using Landsat TM data: When and how to correct atmospheric effects? *Remote Sensing of Environment*, **75**, 230-244.
- Song C, Band LE (2004) MVP: a model to simulate the spatial patterns of photosynthetically active radiation under discrete forest canopies. *Canadian Journal of Forest Research*, **34**, 1192-1203.
- Sullivan NH, Bolstad PV, Vose JM (1996) Estimates of net photosynthetic parameters for twelve tree species in mature forests of the southern Appalachians. *Tree physiology*, **16**, 397-406.
- Swift LW, Cunningham J, G.B., Douglass JE (1988) Climatology and hydrology. In: *Forest Hydrology and Ecology at Coweeta* (eds Swank WT, Crossley JDA), pp. 35-55. Springer-Verlag, New York, NY, USA.
- Tague CL, Band LE (2004) RHESSys: Regional Hydro-Ecologic Simulation System--an object-oriented approach to spatially distributed modeling of carbon, water, and nutrient cycling. *Earth Interactions*, **8**, 1-42.
- Teillet PM, Fedosejevs G, Thome KJ, Barker JL (2007) Impacts of spectral band difference effects on radiometric cross-calibration between satellite sensors in the solar-reflective spectral domain. *Remote Sensing of Environment*, **110**, 393-409.

- Teillet PM, Guindon B, Goodenough DG (1982) On the slope-aspect correction of multispectral scanner data. *Canadian Journal of Remote Sensing*, **8**, 84-106.
- Tian YH, Woodcock CE, Wang YJ, et al (2002a) Multiscale analysis and validation of the MODIS LAI product - I. Uncertainty assessment. *Remote Sensing of Environment*, **83**, 414-430.
- Tian YH, Wang YJ, Zhang Y, Knyazikhin Y, Bogaert J, Myneni RB (2002b) Radiative transfer based scaling of LAI retrievals from reflectance data of different resolutions. *Remote Sensing of Environment*, **84**, 143-159.
- Tucker CJ (1979) Red and Photographic Infrared Linear Combinations for Monitoring Vegetation. *Remote Sensing of Environment*, **8**, 127-150.
- Turner DP, Cohen WB, Kennedy RE, Fassnacht KS, Briggs JM (1999) Relationships between leaf area index and Landsat TM spectral vegetation indices across three temperate zone sites. *Remote Sensing of Environment*, **70**, 52-68.
- Uchida T, Meerveld IT, McDonnell JJ (2005) The role of lateral pipe flow in hillslope runoff response: an intercomparison of non-linear hillslope response. *Journal of Hydrology*, **311**, 117-133.
- Vermote EF, ElSaleous N, Justice CO, Kaufman YJ, Privette JL, Remer L, Roger JC, Tanre D (1997) Atmospheric correction of visible to middle-infrared EOS-MODIS data over land surfaces: Background, operational algorithm and validation. *Journal of Geophysical Research-Atmospheres*, **102**, 17131-17141.
- Vincini M, Reeder D, Frazzi E (2002) Seasonal Landsat TM data topographic dependence in rugged deciduous forest Areas. In: *Analysis of Multi-temporal Remote Sensing Images - Proceedings of the First International Workshop* World Scientific Publishing Co. Pte. Ltd., River Edge, NJ.
- Walko RL, Band LE, Baron J, et al (2000) Coupled atmosphere-biophysics-hydrology models for environmental modeling. *Journal of Applied Meteorology*, **39**, 931-944.
- Whittaker RH (1956) Vegetation of the Great Smoky Mountains. *Ecological Monographs*, **26**, 1-69.
- Wolfe RE, Nishihama M, Fleig AJ, Kuyper JA, Roy DP, Storey JC, Patt FS (2002) Achieving sub-pixel geolocation accuracy in support of MODIS land science. *Remote Sensing of Environment*, **83**, 31-49.
- Zhang YQ, Chiew FHS, Zhang L, Leuning R, Cleugh HA (2008) Estimating catchment evaporation and runoff using MODIS leaf area index and the Penman-Monteith equation. *Water Resources Research*, **44**, W10420.

Chapter 5 Summary and conclusions

In this dissertation, three research studies are presented concerning integration of spatio-temporal vegetation dynamics into a distributed ecohydrological model with application to optimality theory and real-time simulation. Spatial pattern of vegetation density is estimated at different scales with a combination of simulation and multi-temporal remote sensing data sets, further evaluated with field measurements. Hydrologic gradients of vegetation density within a small catchment are related to the optimal state for carbon uptake as a function of lateral hydrologic connectivity. Phenological features are extracted from global satellite products to find the topography-mediated controls on vegetation phenology at a local scale. Finally, near real-time dynamics of vegetation density are updated for distributed ecohydrological simulation by fusing multi-temporal Landsat and MODIS data.

In Chapter 2, we test whether the simulated spatial pattern of vegetation corresponds to measured canopy patterns and an optimal state relative to a set of ecosystem processes, defined as maximizing ecosystem productivity and water use efficiency at the small catchment scale. Vegetation density along the hillslope gradient may effectively represent the degree of dependency of multiple interacting resources (water and nutrients) as a function of lateral hydrologic connectivity, moderated by feedbacks with canopy light absorption.

In this study, we found the following:

- Model results suggest that more efficient photosynthesis can take place downslope due to more efficient water use for carbon uptake and increased nitrogen availability,

producing a feedback with more light absorption through the development of greater leaf area and lower belowground proportional allocation.

- The spatial distribution of rooting depth and allocation dynamics estimated from pit excavations show very similar patterns to those estimated from the optimal hydrologic gradients of vegetation density.
- Simulated canopy growth shows effective compromises between multiple stresses (water, light, and nutrients) for optimal carbon uptake through the control of aboveground vegetation density by limited photosynthate allocation.
- The existing hydrologic gradients of vegetation density within the catchment effectively represent the degree of dependency on productivity and resource use with other patches along flowpaths and the long-term optimal state for carbon uptake, which is closely modulated by rooting and allocation strategies.

In Chapter 3, multi-year trajectories of the MODIS NDVI data are filtered and fitted to find the topography-mediated controls on vegetation phenology within the study site. We find well expressed spatial patterns of phenological signals as a function of topography, closely related to micro-climate variations, vegetation community types, and hillslope positions.

- Elevation is a primary factor characterizing topography-mediated phenological features for both greenup and senescence, related to environmental temperature lapse rate and combined orographic precipitation.

- Radiation proxies have significant explanatory powers for all phenological variables, which are affiliated with photoperiod controls or combined effect with temperature.
- Hillslope position only show positive relationships with greenup phenological variables which may be explained by cold air drainage. However, strong precipitation-related controls on phenology are found in terms of both orographic and interannual variations.
- Phenological signals at MODIS scale lead to important scale issues in their relationships with topographic factors, especially due to the scale variance nature of radiation proxies and reduced variances produced by aggregating phenological and topographic information.

In Chapter 4, daily spatial patterns of vegetation density (FPAR, LAI) over complex terrain are estimated at a high resolution by fusing multi-temporal MODIS and Landsat TM data in conjunction with topographic information. Two downscaling methods are developed to overcome spatial and temporal limitations of MODIS and Landsat image sets in applications of spatially and interannually variable vegetation phenology into catchment-scale distributed hydrological modeling.

- FPAR is more physically meaningful and more easily scalable between different spatial resolutions, therefore the incorporation of FPAR as a downscaling variable helps to solve the scale invariance problem of NDVI in the application of multi-resolution methodology.

- Sub-grid variability of the fitted MODIS FPAR is represented by the composite Landsat NDVI images with a simple linear proportionality parameter. This includes a linear relationship between sub-grid NDVI and FPAR, as well as proportional phenological discrepancy between MODIS FPAR and composite Landsat NDVI on corresponding day of year.
- A simple linear assumption between sub-grid NDVI and FPAR is not met when there is significant heterogeneity in biome and land cover type within a MODIS pixel as the relationship strongly depends on biome types and forest structures.
- Considering sub-grid variability of incoming radiation during a downscaling process has limited effects with the exception of winter season when there is significant positive covariance between sub-grid incident PAR and composite NDVI values, as well as increased sub-grid variability of incident PAR with a high sun zenith angle.

In this dissertation, two different complementary approaches (top-down and bottom-up) are incorporated into a distributed ecohydrological model for spatio-temporal vegetation dynamics. A major question is how ecological mechanisms underlie spatio-temporal hydrologic patterns and processes, essentially examining the coupled evolution and interactions within ecohydrological systems. With a bottom-up approach, emergent optimality within the small catchment expands our knowledge of the degree of dependency on productivity and resource use with other patches along flowpaths as a function of lateral hydrological connectivity. With a top-down approach, spatio-temporal patterns of vegetation phenology are related to spatial and interannual variations of hydrological patterns as well as topographic variables. Major biophysical variables (FPAR, LAI) are assimilated into a distributed ecohydrological model by fusing multi-temporal remote sensing products. Spatial pattern of vegetation is a good indicator of surface soil moisture dynamics and lateral hydrologic redistribution. These approaches help to simulate and understand

complicated ecohydrological feedbacks between water and carbon cycles within distributed ecohydrological modeling frameworks. Furthermore, this study also improves our understanding of spatio-temporal ecohydrologic responses (e.g. streamflow, evapotranspiration, vegetation phenology, vegetation growth) to near-future global climate changes especially in mountainous terrains. It also provides the potential for ecohydrological nowcasts and forecasts at the local catchment scale. These studies also suggest forthcoming works as following:

- Real-time ecohydrological nowcasts and forecasts in terms of severe drought and near-future climate changes at the local catchment scale.
- Downscaling vegetation phenology as a function of topographic factors and its application for vegetation response to future climate changes.
- Cross verification of interannual vegetation dynamics with various field measurements such as continuous FPAR measurements, phenological observations, and tree ring data.
- Validation of suggested allocation dynamics along the hillslope gradients with detailed aboveground and belowground biomass estimation.
- Further studies about the relationship between hydrologic gradients of vegetation density and lateral hydrologic connectivity at different sub-watersheds in the study site.